Pós-Graduação em Ciência da Computação

Luis Filipe Alves Pereira

Development of a fast and cost-effective Computed Tomography system for industrial environments by incorporating priors into the imaging workflow

Universidade Federal de Pernambuco
posgraduacao@cin.ufpe.br
http://cin.ufpe.br/~posgraduacao

RECIFE

2018

Luis Filipe Alves Pereira

Development of a fast and cost-effective Computed Tomography system for industrial environments by incorporating priors into the imaging workflow

Ph.D. Thesis presented to the Center for Informatics of Federal University of Pernambuco in partial fulfillment of the requirements for the degree of Philosophy Doctor in Computer Science.

Advisor: George Darmiton da Cunha Cavalcanti
Co-Advisor: Jan Sijbers and Tsang Ing Ren

RECIFE
2018

Catalogação na fonte
Bibliotecária Monick Raquel Silvestre da S. Portes, CRB4-1217

P436d Pereira, Luis Filipe Alves
Development of a fast and cost-effective computed tomography system for industrial environments by incorporating priors into the imaging workflow / Luis Filipe Alves Pereira. – 2018.
106 f.: il., fig., tab.

Orientador: George Darmiton da Cunha Cavalcanti.
Tese (Doutorado) – Universidade Federal de Pernambuco. CIn, Ciência da Computação, Recife, 2018.
Inclui referências, glossário e apêndices.

1. Ciência da computação. 2. Tomografia computadorizada. I. Cavalcanti, George Darmiton da Cunha (orientador). II. Título.

004 CDD (23. ed.) UFPE- MEI 2018-062

Luis Filipe Alves Pereira

Development of a Fast and Cost-Effective Computed Tomography System for Industrial Environments by Incorporating Priors into the Imaging Workflow

Tese de Doutorado apresentada ao Programa de Pós-Graduação em Ciência da Computação da Universidade Federal de Pernambuco, como requisito parcial para a obtenção do título de Doutora em Ciência da Computação

Aprovado em: 20/03/2018.

_____

Orientador: Prof. Dr. George Darmiton da Cunha Cavalcanti

BANCA EXAMINADORA

_____

Prof. Dr. Silvio de Barros Melo
Centro de Informática /UFPE

_____

Prof. Dr. Carlos Costa Dantas
Departamento de Energia Nuclear / UFPE

_____

Prof. Dr. Abraão David Costa do Nascimento
Departamento de Estatística / UFPE

_____

Prof. Dr. Wellington Pinheiro dos Santos
Departamento de Engenharia Biomédica / UFPE

_____

Profa. Dra. Margarida Mizue Hamada
Instituto de Pesquisas Energéticas e Nucleares / USP

This work is dedicated to my parents and my future wife who brought lights when very dark nights suddenly came.

ACKNOWLEDGMENTS

I am deeply grateful to Professor George and Professor Tsang for teaching me about how to do science during the last 8 years. I am also immeasurably grateful to Professor Sijbers for had patiently guided me into the world of tomography. I am sure that all three of them can find a friend in me from now on. I also would like to thank some colleagues who helped me, at least once, when I asked for them in this PhD trajectory, they are: Hector Pinheiro, Thyago Porpino, Dimas Cassimiro, Tom Roelandts, Geert Van Eyndhoven, Willem Jan Palenstijn, Wim van Aarle, Eline Janssens, and Andrei Dabravolski. I also grateful to our colleagues from BIOSYST-MeBios in KU Leuven who kindly allowed us to use their dataset of CT images: Mattias Van Dael, Pieter Verboven, and Bart Nicolai.

"You cannot teach a man anything, you can only help him to find it within himself."
(Galileo Galilei)

ABSTRACT

Conventional X-ray radiography has been extensively used for inspection and quality assurance of industrial products. However, 2-D X-ray radiography cannot provide quantitative information within three dimensions about the scanned object. To obtain such depth information, X-ray Computed Tomography (CT) should be applied. Nevertheless, conventional CT systems (at which the X-ray source and detector rotates around the target object) are cost ineffective, inflexible, and suffer from long acquisition times. Therefore, the deployment of such technology is unfeasible for many industrial environments where high throughput is required as much as the best cost-benefit rate. The main goal of this research is to design a simple and cost-effective X-ray CT imaging system of high throughput for industrial environments. This system should comprises a single and static pair of X-ray source and detector for imaging objects passing on a conveyor belt. Such setup has been widely used with traditional radiographs for quality assurance in industrial environments; however, the large number of unknown projection views made such setup unfeasible for CT. Computer vision- and machine learning-based improvements are applied to incorporate prior knowledge about the scanned object into the CT imaging workflow as a way of compensating the lack of multiple X-ray sources or moving parts in both source and detector. More precisely, it is evaluated the use of priors related to the materials composition and also the outer object shape, as well as the use of Machine Learning techniques to apply priors automatically extracted from a training set of previous reconstructions. The trade-off between reconstruction quality and system's throughput is exposed by linking the following measures: processing time, conveyor belt acceleration/deceleration, number of X-ray projections, reconstruction accuracy, and image resolution. It is also shown that one of the proposed methods can improve the system's throughput in 21% while keeping the reconstruction accuracy over 90%. This research represents an advance in the state-of-the-art since it demonstrates that is possible to generate good quality reconstructions from projections acquired in an usual scanning setup where both X-ray source and detector are statically positioned.

Key-words: Computed Tomography. Discrete Tomography. High throughput CT.

RESUMO

A radiografia tradicional, que utiliza raios-X, tem sido bastante utilizada para inspeção e controle de qualidade de produtos na indústria. No entanto, através de uma radiografia 2-D não é possível obter informações qualitativas em três dimensões sobre o objeto analisado. Para obter tal informação de profundidade, a Tomografia Computadorizada (TC) pode ser aplicada. Todavia, sistemas convencionais de TC (nos quais a fonte de raios-X e o detector giram em torno do objeto analisado) são de alto custo, inflexíveis, e necessitam de um longo tempo para aquisição de dados. Dessa forma, o uso dessa tecnologia é desaconselhável em ambientes industriais que demandam uma alta velocidade de processamento, além de baixo custo de implantação e manutenção. O principal objetivo dessa pesquisa é projetar um sistema de TC simples, de relativo baixo custo e de alta velocidade para ambientes industriais. Esse sistema deve ser composto por um único par de fonte e detector de raios-X posicionado estaticamente para escanear objetos que passam sobre uma esteira elétrica. Tal configuração tem sido extensamente utilizada para inspeção de qualidade utilizando radiografia 2-D em indústrias; no entanto, o baixo número de ângulos de visões disponíveis têm feito essa configuração inapropriada para tomografia. Técnicas implementadas usando visão computacional e aprendizagem de máquina são aplicadas para introduzir conhecimento *a priori* sobre o objeto em estudo no fluxo de dados da reconstrução de imagens em um sistema de TC, com isso espera-se compensar a falta de múltiplas fontes de raios-X ou movimentos entre a fonte e o detector de radiação. Mais precisamente, é avaliado o uso de conhecimento *a priori* sobre a composição do objeto e seu formato externo, bem como o uso de técnicas de Aprendizagem de Máquina para aplicar informações que foram extraídas automaticamente de um conjunto de treinamento formado por reconstruções anteriormente realizadas. O balanceamento entre a qualidade das reconstruções e a velocidade do sistema é apresentado nesse trabalho relacionando as seguintes medidas: tempo de processamento, aceleração/desaceleração da esteira, número de projeções de raios-X capturadas, acurácia da reconstrução e resolução da imagem reconstruída. Também é apresentado um método que é capaz de aumentar a velocidade do sistema em 21% enquanto a acurácia da reconstrução é mantida em ao menos 90%. A presente pesquisa contribuiu para o estado-da-arte da área ao demonstrar que é possível gerar reconstruções de boa qualidade a partir da aquisição de projeções em um sistema tomográfico não convencional no qual o emissor e o receptor de radiação estão posicionados estaticamente.

Palavras-chaves: Tomografia Computadorizada. Tomografia Discreta. Tomografia de alta velocidade.

LIST OF FIGURES

LIST OF TABLES

ACRONYMS

ANN Artificial Neural Network. 16, 17, 52, 53, 55, 58, 59, 61, 62, 84, 86

ART Algebraic Reconstruction Techniques. 35–39, 58, 65, 66, 86

ASD-POCS adaptative-steepest-descend-POCS. 57

ASIR Adaptative Statistical Iterative Reconstruction. 56

BoF Bag-of-Features. 11, 70, 71

BP Belief Propagation. 58

CNN Convolutional Neural Network. 53, 86

CT Computed Tomography. 8–12, 16, 17, 19, 21–32, 39, 40, 50, 52, 54, 56, 58, 59, 61, 62, 64–66, 69, 70, 72, 74, 75, 81, 83–86, 102, 103

DART Discrete Algebraic Reconstruction Technique. 9, 11, 37–39, 58, 64–66, 72–74, 84, 85

DSCT Dual Source Computed Tomography. 26

DSR Dynamic Spatial Reconstructor. 25, 26

EBT Electron Beam Tomography. 25

EM Expectation Maximization. 55

EOD Expected Object Domain. 12, 65, 66, 73, 75, 84

FBP Filtered Back Projection. 34, 35, 59, 64, 72, 78, 83, 84

GGMRF Generalized Gaussian Markov Random Fields. 56

IRIS Image Reconstruction in Image Space. 56

IT Information Technology. 19

LDCT Low-Dose Computed Tomography. 50, 51

MAP Maximum A Posteriory. 51, 56, 57

ML Maximum Likelihood. 51, 55

ML Machine Learning. 66

MLP Multilayer Perceptron. 67, 71

MRF Markov Random Fields. 56–58

NDT Non-destructive Testing. 19–21, 23, 24, 29, 84, 85

NLM Non-Local Means. 56, 57, 61, 62

NN-FBP Neural Network Filtered Back Projection. 59

POCS Projections Onto Convex Sets. 17, 55, 57

PSRR Previous Scan Regularized Reconstruction. 61

PWLS Penalized Weighted Least-Square. 51

RF Random Forest. 67, 71

RTT Real Time Tomography. 26

S-FBP Segmented FBP. 11, 72–74

S-SIRT Segmented SIRT. 11, 72–74

SIFT Scale-Invariant Feature Transform. 70, 71

SIRT Simultaneous Iterative Reconstruction Technique. 36, 37, 64, 72, 73, 78, 83, 84, 86

TV Total Variation. 56, 57

WLS Weighted-Least Squares. 51

CONTENTS

1 INTRODUCTION

This initial chapter introduces the context of this research and states its main goal and its specific objectives. A quick overview of the reduction of processing time in Computed Tomography (CT) over time is also presented. Finally, the structure of this document is exposed.

1.1 Context

The most successful companies around the world are committed to deliver the best experience to the consumer at competitive prices. In fact, consumers consider the product's quality, functionality, price, and the reputation of the brand name when buying an item. Simultaneously, in an era of globalization, manufacturing firms have been finding economical advantages on outsourcing their production lines. In Information Technology (IT) industry, Quanta Computer Incorporated (a Taiwan-based manufacturer) provides computer devices to larger companies such as Apple, Compaq, Dell, Gateway, Lenovo and Hewlett-Packard (NAGURNEY; LI, 2015). In the automotive industry, non-US based companies such as Minda HUF, Visteon, Arvin Meritor and Rico Auto supply components to the US head office of Volvo (NAGURNEY; LI, 2015). This trend creates a very competitive market between the outsourcing companies. As a result, issues related to product quality have been raised to another level because the reputation associated with the outsourced product remains with the original firm.

The production quality is also an important issue in agriculture market. For instance, Brazil is currently the third fruit producer in the world (GUEDES; SENA; TOLEDO, 2013). However, Brazil has exported too few: it is only the fifteenth in the ranking of largest fruit exporter countries (CARVALHO; MIRANDA, 2009). Brazil exports fewer fruits than Chile, for example. In part, this is due to the difficulty of Brazilian rural producers in attending the quality requirements of international markets.

Companies must invest in Non-destructive Testing (NDT) to assess the quality of products just before they leave the industry. According to Shull (SHULL, 2002), the basic principle of NDT is to *"determine the quality or integrity of an item non-destructively"*. For instance, to ensure the production quality at fruit industry, it is desirable to detect browning and holes in apples without cutting them.

NDT may apply distinct technologies such as *ultrasound*, *thermography*, *microwave*, *visible radiation*, *radiology*, and others. The decision about which method is the most suited for each particular case is usually based on two aspects: *(i)* the properties that should be evaluated (*i.e.* mechanical or electromagnetic); and *(ii)* the costs associated

to the deployment and the maintenance of such inspection technology in relation to the costs of manufacturing the product.

Ultrasonic NDT is based on the use of high-frequency sound waves (from 50 kHz to several GHz). Since the propagation velocity of those waves varies according to environment properties, the echo detected during an ultrasonic inspection can be used to characterize the object's composition, structure, density, and geometry. Ultrasonic NDT has been applied in aeronautical engineering (KATUNIN; DRAGAN; DZIENDZIKOWSKI, 2015), food industry (MORRISON; ABEYRATNE, 2014), electrical engineering (YE et al., 2014), civil engineering (PLANÈS; LAROSE, 2013), and other fields.

Thermographical NDT is classified as *active* or *passive*. In *active thermography*, an external heating source is used to irradiate the object while a thermal camera measures the resulting temperature distribution on the object's surface. Active thermography has been used in aeronautical engineering (BATES et al., 2000), in food industry (GINESU et al., 2004), in civil engineering (MEOLA, 2007), and other fields. On the other hand, in *passive thermography*, no external heating source is used. Then, the temperature distribution along the object's surface is measured within normal conditions. Passive thermography has been used in inspection of electrical equipments (JADIN; TAIB, 2012), in food industry (VERAVERBEKE et al., 2006; MANICKAVASAGAN et al., 2005), in civil engineering (CLARK; MCCANN; FORDE, 2003), and other fields.

In *microwave*-based NDT, a high-frequency electromagnetic energy (from few hundred MHz to few hundred GHz) irradiates the object. Those electromagnetic waves interact with the dielectric[1] regions of the object. As a result, by measuring the scattered and transmitted electromagnetic waves through the object, it is possible to determine its electrical properties. Microwave-based NDT has been used in electronics engineering (JU; SAKA; ABE, 2001), in civil engineering (SAKAI et al., 2012), in pharmaceutical industry (ANUAR et al., 2007), and other fields.

In NDT based on *visible radiation*, the object is irradiated using visible light, and a standard video camera is used to record multiple image frames of the object. Then, pattern recognition algorithms running on digital computers analyze such image frames. Such algorithms can estimate the dimension, surface, and assembly characteristics of a manufactured items. *Visible radiation*-based NDT has been used in textile industry (BAHLMANN; HEIDEMANN; RITTER, 1999), in food industry (BROSNAN; SUN, 2004), and other fields.

Radiology is one of the most commonly used NDT methods. In fact, it is one of the few methods that can examine the interior of the objects. It is the only NDT method that works on all materials according to Shull (SHULL, 2002). The required equipment for X-ray testing includes at least a radiation source and a detector. Electrically powered source tubes create radiation through the collision between accelerated electrons and a

[1] refers to electrical insulator materials that can be polarized by an electric field.

target material to release photons. By adjusting the voltage that accelerates the electron, the system operator can control the energy of the photons. By adjusting the current in the electrical circuit, the system operator can control the number of photons. The X-ray detector is composed of an array of transducers that convert the intensity of the incident radiation into electrical current. Since distinct materials absorb different levels of X-ray energy according to its densities, the amount of energy that reaches the detector transducers can be used for imaging distinct structures that may comprise the interior of the irradiated object. Those images are often referred to as radiography. Radiography-based NDT has been used in food industry (HAFF; TOYOFUKU, 2008; KWON; LEE; KIM, 2008; OGAWA; KONDO; SHIBUSAWA, 2003; AYALEW et al., 2004; JIANG et al., 2008; CHUANG et al., 2011; MERY et al., 2011; NIELSEN; CHRISTENSEN; FEIDENHANS, 2014; KELKAR; BOUSHEY; OKOS, 2015; MATHANKER et al., 2011), in electronics engineering (ETIEMBLE et al., 2015; MAHMOOD et al., 2015; UEHARA; YASHIRO; MOMOSE, 2013; WANG; WANG; ZHANG, 2014), in inspection of gas and oil transmission in pipelines (YAZDANI et al., 2014; YANG et al., 2014), in automotive industry (CARRASCO; MERY, 2011; MERY, 2006; LI et al., 2006; MERY; FILBERT, 2002; MERY, 2003), in electrical engineering (JASINIEN et al., 2009; FANTIDIS; POTOLIAS; BANDEKAS, 2011), in welding inspection at nuclear, naval, chemical and aeronautical industries (WANG; LIAO, 2002; VILAR; ZAPATA; RUIZ, 2009; ZAPATA; VILAR; RUIZ, 2011; SHAO et al., 2012; ZAHRAN et al., 2013), in security inspection systems at airports and railway stations (ZHANG; ZHANG; CHEN, 2005; WELLS; BRADLEY, 2012; MICHEL et al., 2007; ABIDI et al., 2006; SINGH; SINGH, 2005; OERTEL; BOCK, 2006; NERCESSIAN; PANETTA; AGAIAN, 2008), and other applications.

Despite widely used in industry, conventional X-ray radiography has an inherent drawback: it cannot provide depth information. Radiography superimposes information along the radiation path onto the detector. As a result, it is impossible to identify features of interest occluded by others or to quantify the volume occupied by a specific material within the object. On the other hand, X-ray CT captures multiple X-ray radiography projections from few hundred of different angles. Those projections are mathematically combined by a computer algorithm to generate multiple 2-D cross-section images (which are equivalent to create a 3-D model) of the irradiated object as illustrated in Figure 1. In this thesis, Chapter 2 presents the mathematical tools that allow mapping the X-ray data from the projection domain into the reconstruction domain[2]. For instance, Figure 2 (a) shows a conventional 2-D X-ray radiography of an apple; and Figure 2 (b) shows nine cross-section images of the same apple generated by using CT. It is clear that CT provides much more information than conventional radiography for quality inspection.

A typical workflow in CT imaging (illustrated in Figure 3) is composed of the following stages (AARLE, 2012): *acquisition*, *data preprocessing*, *reconstruction*, *segmentation*, and *analysis*. During the *acquisition* phase, an X-ray source and detector usually rotates

[2] for detailed description about the domains involved in a CT processing, see Appendix A.

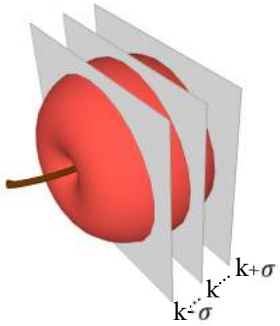

Figure 1 – Representation of $2\sigma + 1$ cross sections of an apple that are generated in a CT reconstruction.

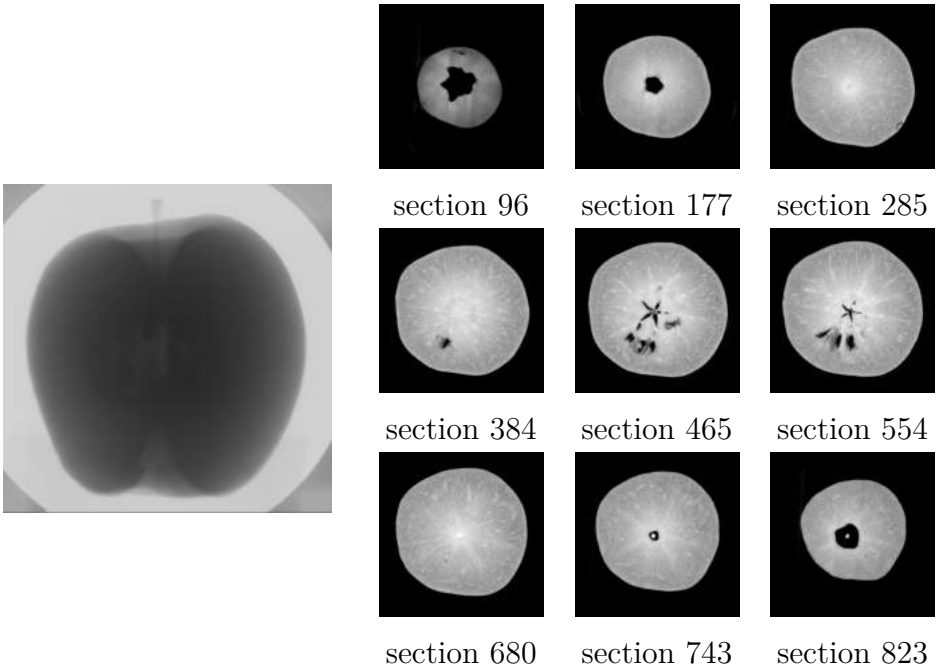

Figure 2 – Conventional 2D X-ray radiography of an apple (a); and nine cross section images of the same apple generated by using CT. (**Source:** radiography and image reconstructions acquired at BIOSYST-MeBios, KU Leuven, Belgium).

around a target object to generate X-ray projection data from multiple points of view (*i.e.*, projection angles). The visual representations of such raw data are referred to as sinograms. Then, in the *data preprocessing* stage, a logarithmic transform is calculated to map the intensity values of radiation in the projection data into log-corrected attenuation values. Next, the *reconstruction* phase aims at generating multiple 2-D images representing the internal content of the target object in many cross sections. Thereby, the intensity value in each pixel is related to the density of the material in that region of the object. Afterwards, the *segmentation* step classifies the pixels into meaningful groups to promote an easier analysis of the results. Finally, in the *analysis* stage, the output is

evaluated according to specific metrics. This phase can be automated using a Computer Vision algorithm.

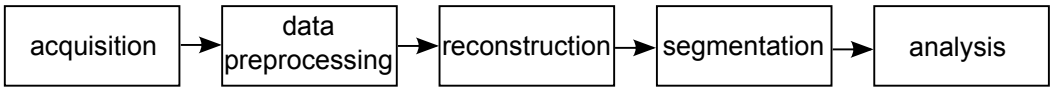

Figure 3 – Typical workflow in CT imaging. In the *acquisition* phase, multiple X-ray projection data are generated from a target object. Then, in the *data preprocessing* stage, the projection data is transformed into log-corrected attenuation values. Next, the *reconstruction* phase aims on generating images representing internal structures of a target object. Next, the *segmentation* step classifies the pixels into meaningful groups. Finally, in the *analysis* stage, the output is evaluated according to specific metrics given by the application. (**Source:** adapted from (AARLE, 2012)).

The acquisition stage of conventional CT workflow is typically very time consuming since the scanned object, the radiation source, and the X-ray detector must be rigorously static about each other at every X-ray projection acquisition. Moreover, multiples projections are acquired from different angular views to compose the necessary raw data for a CT reconstruction. Also, the hardware devices used to synchronize the X-ray pulses and the rotation engine, the X-ray detector cells, and the radiation source are very expensive. Therefore, the use of such technology is unfeasible for many industrial environments which require a high throughput inspection and a deployment cost as low as possible. The design of a simple, cost-effective, and fast X-ray CT system will allow the employment of such 3-D imaging technology in many industries that are currently employing conventional 2-D radiography (*e.g*, inspection of food products, electronic components, automotive engines).

1.2 Motivation

To the best of our knowledge, the high throughput X-ray CT systems that were developed up to the present date for NDT in industrial environments are expensive due to the use of cutting-edge hardware-based technologies. For instance, to allow a full angular sampling of few hundreds of radiography projections around the scanned object within a short period, it is possible to increase the number of X-ray sources used in the system or even to reduce the duration of one projection acquisition. As a result, the ratio between the costs associated with the deployment of such technology and the value of the manufactured product itself is prohibitive to the most of the industries.

To popularize this 3-D imaging technology for NDT among as many industries as possible, the design of a simple, flexible, and cost-effective CT technology is required. A solution which covers those properties would allow the employment of this cutting-edge

NDT technology to the inspection of lower cost (but not less important) products, such as fruits and foods in general.

In this thesis, we propose the use of a simpler hardware design that will lead to a cost-effective technology. Thus, software-based improvements are studied and discussed in this thesis to incorporate prior knowledge into the reconstruction process as a way of compensating the lack of expensive hardware devices into the X-ray CT system. In the future, the technology developed in this work can be also incorporated into CT systems that apply other types of radiation, such as gamma-ray.

1.3 Objectives

In this thesis, our main goal is to *develop a fast and cost-effective CT system for industrial environments by incorporating priors related to the scanned objects into the image reconstruction workflow*. To achieve this research goal, we defined the following specific objectives:

- To evaluate the performance of conventional reconstruction techniques in a simple setup for fast CT scanning comprising a single pair of X-ray source and detector statically positioned for imaging objects passing on a conveyor belt.
- To incorporate prior knowledge related to the materials composition and also the outer object shape into the imaging process.
- To incorporate prior knowledge extracted from a training set of similar objects previously scanned into the imaging process.
- To evaluate both the processing time and reconstruction quality of the solutions proposed in this thesis in relation to conventional techniques.
- To investigate if a solution for Non-destructive Testing (NDT) based on CT X-ray imaging that bypasses the reconstruction stage would be plausible. Thus, the acquisition stage would be directly connected to the analysis stage of the imaging workflow.

1.4 Improvements in temporal resolution of CT systems over time

In CT imaging, *temporal resolution* refers to the duration of time required for the full processing of one object cross-section. Toward the development of a high throughput X-ray CT system, we are interested in the progress of temporal CT resolution along the history.

A fundamental principle of X-ray tomography is that the irradiated object should remain unchanged during the acquisition of the projections (MAIRE; WITHERS, 2014). Thus, researchers have been focused on the development of faster CT systems to allow the imaging of moving organs (*e.g.*, heart, and lungs) and the evaluation of events that take place on small time scales (*e.g.*, solidification process of a specific material).

In 1969, the first CT prototype had a temporal resolution of 9 days (BUZUG, 2008). Since then, a lot of effort has been applied to make CT faster. By the end of 1979, the acquisition time was reduced to less than 20 seconds (BUZUG, 2008) per image slice. With the introduction of slip-ring scanners in 1987, researchers replaced the power source cables which limited the rotation of the X-ray tube to single 360° turns about the object. As a result, the scan time of 1 second became available to reconstruct isolated cross-section images (KALENDER, 1994). In the 1990s, spiral CT allowed continuous scanning of multiple cross-sections in the object. The spiral scanning geometry is exhibited in Figure 4, the illustration shows that the X-ray source (1) and the detector rotate around the patient (2) which is shifted at a speed of one slice thickness d per rotation cycle. As a result, a total scan of 20 to 60 seconds was enough to most medical applications (KALENDER, 1994). In 1998, the multi-slice systems were introduced to scan from 2 to 4 cross-section images simultaneously (TAGUCHI; ARADATE, 1998). By the end of 2004, 256-slice CT systems were commercialized (MORI et al., 2004). In 2016, one of the most advanced clinical CT systems produced by General Electric applies the spiral scanning geometry with $d = 160$ mm and a rotation speed of the X-ray tube about 0.28 seconds per cycle.

The resolution time of medical CT scanners that apply the spiral geometry are limited by the maximum centripetal acceleration that can be experienced by the X-ray tube. By 2006, this acceleration was about 30 times the gravitational force (KALENDER, 2006). Higher speeds of rotation can only be achieved with investments on more robust hardware devices.

In the early of the 1980s, an alternative approach to achieve a high-speed CT was proposed for cardiac imaging (BOYD; LIPTON, 1983), the Electron Beam Tomography (EBT). This technology is based on the magnetic deflection of an electron beam to replace the mechanical motion of the X-ray tube was initially proposed. Due to the use of an electrostatic field configuration within a gun of electron beams, EBT systems are costly and less used nowadays.

Also in early of the 1980s, Berniger *et al.* patented the first CT system with multiple X-ray sources to provide a high-speed scanning (BERNINGER; REDINGTON, 1980). That configuration also included rotating parts around the object. About the same time, the Dynamic Spatial Reconstructor (DSR) was developed at Biodynamics Research Unit at the Mayo Clinic for a fast scanning (ROBB et al., 1983). The DSR simultaneously acquired projections from 28 X-ray sources placed around a 160° within a circular structure which

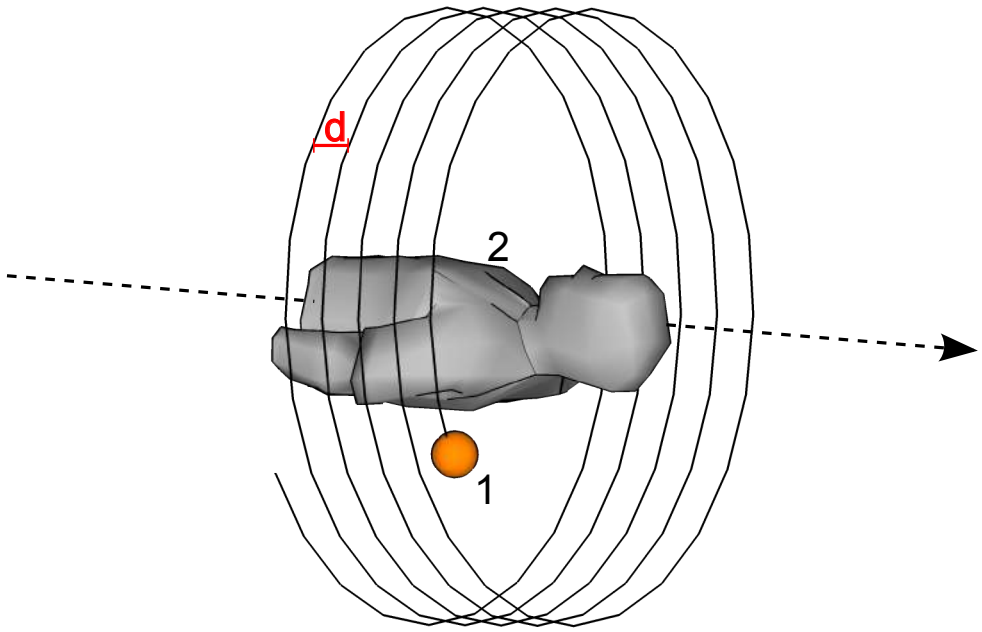

Figure 4 – Scanning geometry of spiral CT: the X-ray source (1) and the detector rotate around the patient (2) which is shifted at a speed of one slice thickness d per rotation cycle.

rotates around the patient. Moreover, 2-D projections were acquired for each X-ray source. As a result, the DSR could scan up to 240 adjacent cross-sections at rates up to 60 images per second.

In 1998, Hori *et al.* (HORI; FUJIMOTO; KAWANISHI, 1998) proposed a high-speed CT system based on 60 stationary X-ray sources. Such setup provided a throughput of 2000 slices per second. Also in 1998, Morton *et al.* (MORTON et al., 1998) designed a high-speed system based on 7 X-ray sources arranged in an annular geometry for the analysis of multiphase flow. Morton's system was able to generate 50 image cross-section per second. By 2005, the first commercialized Dual Source Computed Tomography (DSCT) comprised two X-ray sources and two corresponding detectors offset by 90° rotating about the patient. This DSCT could provide a spatial resolution of 60 milliseconds (or a throughput of 16 cross-section images per second).

In 2009, Morton *et al.* (MORTON et al., 2009) designed a Real Time Tomography (RTT) system able to produce 480 cross-section images of objects travelling in a conveyor belt at speed up to 0.5 m/s. To avoid any physical moving parts, Morton *et al.* proposed the use of a multi-focus X-ray source circumference composed of 384 to 768 focal spots. By pulsing those individual X-ray sources in a suitable scanning sequence, the impression of motion was achieved without any moving parts. The first prototype of this machine, the RTT80 (illustrated in Figure 5), was built for luggage inspection. Similar static setup with X-ray sources pulsing in a sequence was also exploited in (NIEMI; LASSAS; SILTANEN,

2013; THOMPSON et al., 2015).

Figure 5 – Prototype of RTT80 machine for luggage inspection. (**Source:** theengineer.co.uk, accessed on July 2016, <https://www.theengineer.co.uk/issues/awards-2010/rtt80-baggage-scanner/>).

All the methods mentioned above for improving the throughput of CT systems are oriented to the development of new hardware-based technologies. More precisely, the idea behind all those methods is: *to acquire the highest number of projections within the shortest period of time*. Once many projection data is available, the projections are reconstructed using standard Fourier-based methods (SHEPP; LOGAN, 1974) in the vast majority of those cases. In this scenario, the ultimate limit of reachable time resolution is defined by the hardware applied in the acquisition phase (RACK et al., 2010). As a result, all those methods are costly due to the use of modern hardware-based technologies. Then, the deployment of those systems may be prohibitive to many production lines due to its cost-benefit ratio.

On the other hand, software-based improvements to the CT workflow have been proposed to the scenarios in which too few projections are acquired because *(i)* the time to collect the ideal number is prohibitively long or *(ii)* the X-ray dose[3] must be limited to safe levels (MAIRE; WITHERS, 2014). To deal with such under-sampled scenarios, the basic strategy shared in the state-of-the-art is *to incorporate prior knowledge about the scanned objects into the (i) pre-processing, (ii) reconstruction, and/or (iii) post-processing stages.*

This thesis is focused on the development of a fast and cost-effective CT system for industrial environments based on incorporating prior knowledge about the scanned object into the imaging process. The trade-off between reconstruction quality and system throughput will be a guideline to evaluate the proposed solutions.

[3] refer to the intensity of energy that is used in the scanning process.

1.5 Document Structure

The next chapters of this document are organized as follows:

In **Chapter 2**, we summarize basic concepts and techniques related to the acquisition and reconstruction stages of the CT workflow. This theory is fundamental to a complete comprehension of this work.

In **Chapter 3**, we introduce and discuss technical issues that emerge in the design of a fast inline X-ray CT system. This chapter also highlights the challenges that should be overcome in this research.

In **Chapter 4**, we present an organized overview of the most relevant works previously published in the literature about how to incorporate priors into the CT workflow.

In **Chapter 5**, we describe and justify the methods proposed in this thesis toward to the development of a fast inline X-ray CT system.

In **Chapter 6**, we present experimental results and discussions about the methods proposed in this thesis.

In **Chapter 7**, we summarize the contributions achieved in this work and also suggests guidelines for future researches.

2 BACKGROUND ON COMPUTED TOMOGRAPHY

This chapter presents some basic theory, methods, and techniques related to the data acquisition and image reconstruction stages of Computed Tomography (CT) workflow. In the following sections, the reader will find: a brief introduction to the history of X-ray radiography and tomography in Section 2.1; an overview of the evolution of CT scanning systems along the 1970s in Section 2.2; a description of the image reconstruction techniques used in this work in Section 2.3; and a discussion about reconstruction problems related to limited projection data in Section 2.4.

2.1 Introduction

This very brief introduction was written based on the book (BUZUG, 2008). For a detailed study on the history of X-ray CT, the reader may check this bibliography.

Wilhelm Conrad Röntgen, in 1901, won the first Nobel Prize in Physics for his discovery of a new radiation type able to easily penetrate into physical bodies. Such radiation was named as "X-ray", referring to an unknown kind of ray. Continuous improvements in techniques to handle X-rays led to the first medical imaging technology: the radiography, which first enabled physicians to "look inside" the human body without surgeries. In fact, radiography can be used to "see inside" an opaque object. A conventional radiography imaging setup comprises a target object between an X-ray source and a detector, as illustrated in Figure 6. When a short-duration pulse of X-rays is emitted toward the object, the intensity of each X-ray is attenuated while it passes through the matter because the photons of the radiation are absorbed by the atoms which compose the object. Once distinct particles absorb distinct levels of energy, each material has its attenuation coefficient μ. Finally, by measuring the intensity of the X-ray beams (*i.e.*, the number of photons) that reaches the detector cells, it is possible to infer the attenuation coefficients inside the target object.

Apart from medical applications, X-ray radiography is widely used today for Non-destructive Testing (NDT) in the industry, in airports and border crossings to ensure people's safety, in archaeology laboratories to identify the composition of fossil and archaeological discoveries, and in forensic centers to corpses identification. X-ray radiography, however, can not display three-dimensional information about the target object. For this purpose, multiple X-ray projections should be taken from different perspectives (see Figure 7) and then combined to create a 3-D model.

In 1917, Johann Karl August Radon proposed a couple of mathematical operators (the

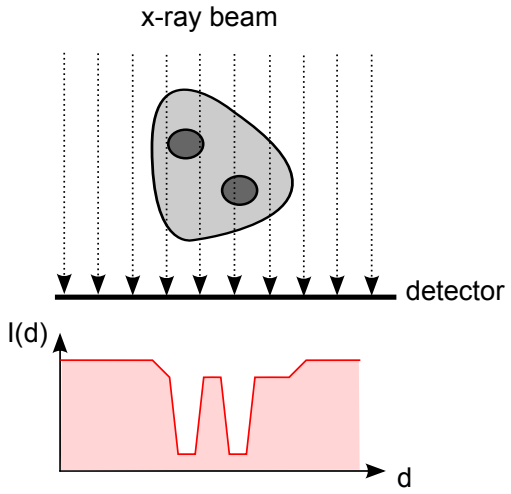

Figure 6 – Setup used in conventional radiography: a target object is positioned in between an X-ray source and a detector. When an X-ray beam passes through the object, each X-ray is attenuated according to the material composition along its path inside the object. Finally, by measuring the intensity of the X-ray beams that reach the detector cells, one can infer the matter composition and distribution inside the target object.

Radon Transform[1] and *Inverse Radon Transform*), which defines the projection values of a two-dimensional object function, and vice versa. Based on Radon's contribution, Allan MacLeod Cormack and Godfrey Hounsfield worked to develop the first prototype of a transmission[2] CT scanner in the second half of $20th$ century. In 1979, both Cormack and Hounsfield were awarded the Nobel Prize in medicine in recognition to their contributions.

[1] for a complete description on Radon Transform, see Appendix B.

[2] refers to the imaging technology at which an external radiation source radiates through the object in the study.

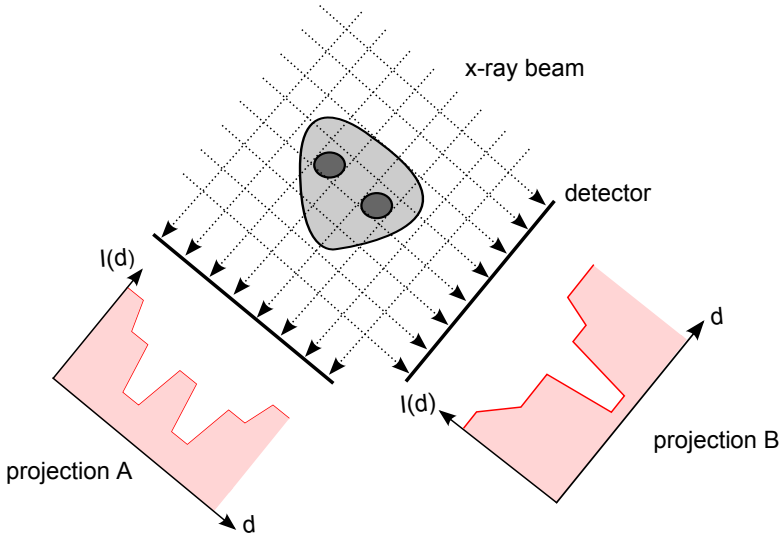

Figure 7 – Basic idea of a transmission tomography: multiple X-ray images are taken from different perspectives and then mathematically combined to create a 3D model of the scanned object.

2.2 The early days of CT

This short overview of the evolution of CT devices was written based on the works of Buzug in (BUZUG, 2008) and Bushberg *et al.* in (BUSHBERG et al., 2011). For a detailed description of the X-ray CT system generations, the reader may check these bibliographies.

From the very first prototypes, at the end of the 1960s, to the latest CT systems, the literature organizes the evolution of such devices in four main generations which were developed along the 1970s. By 1990s, the third and fourth generation of scanners were adapted to yield the spiral scanning geometry[3] that are applied up to the present day in modern medical CT machines.

The first generation of CT scanners comprised an X-ray source, which emitted a single needle-like X-ray beam, and a detector to compose the called *pencil beam* geometry, as shown in Figure 8 (a): the source and a single detector were linearly translated and, at each position increment, the detector was measured to generate a complete projection (like in Figure 6). After a full linear translation, the pair source/detector was rotated and the process was repeated to capture a new projection angle.

The CT scanners of the second generation were quite similar to the previous ones, except for a narrow fan beam which replaced the single needle-like X-ray beam and introduced a more extensive detector composed of approximately 30 elements, as shown in Figure 8 (b). Since the detector array could measure several intensities simultaneously, the acquisition time was reduced.

The development of a more extensive X-ray fan beam angle and correspondingly longer detector array led to the third generation of CT scanners, which allowed the simultaneous

[3] such spiral scanning geometry was previously discussed in Section 1.4.

imaging of an entire measure field, as shown in Figure 8 (c). The acquisition time was highly reduced since the continuous rotation of the source and detector was implemented without interruptions for linear displacement.

The systems developed according to the fourth CT generation comprised a stationary detector ring with up to 5000 elements and an X-ray continuous rotated outside (or inside) such ring, as shown in Figure 8 (d).

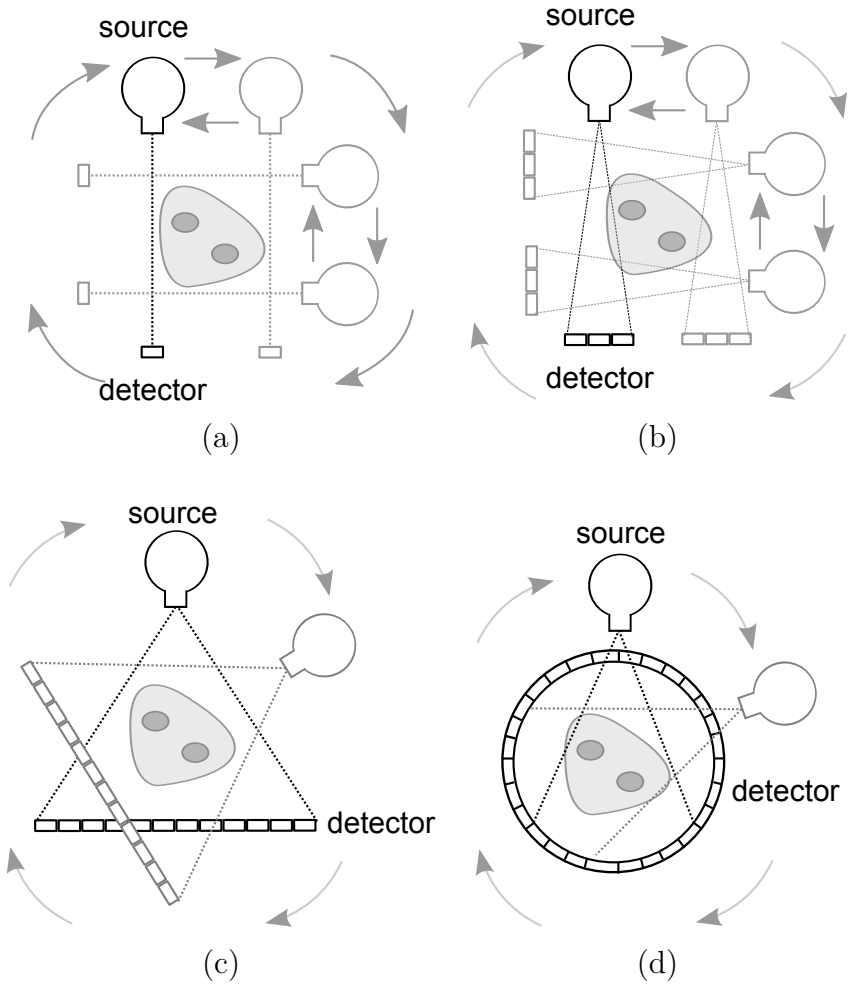

Figure 8 – Diagram of the evolution of CT systems, developed along the 1970s, divided into four generations: (a) in the first generation, CT scanners comprised an X-ray source, which emitted a single needle-like X-ray beam, and a detector to compose the called *pencil beam* geometry: for a complete scanning, rotation of source/detector was interleaved with linear displacements; (b) in the second generation, a narrow fan beam was developed to allow measuring several intensities simultaneously; (c) in the third generation, a larger X-ray fan beam angle and a correspondingly longer detector array allowed the simultaneous imaging of an entire measure field, no more linear displacements were required; (d) in the fourth generation, a stationary detector ring was introduced and the X-ray source continuously rotated (or inside) such ring.

2.3 Image reconstruction techniques

Image reconstruction algorithms are implemented in digital computers to map data from the projection domain into the reconstruction domain[4]. In fact, such methods are feasible alternatives to the Inverse Radon Transform[5] initially proposed by Johann Radon in (RADON, 1986).

Those techniques are divided into Continuous Tomography and Discrete Tomography. Continuous Tomography comprises the more conventional and widely used methods at which almost any value of attenuation coefficients that may occur within an object is represented. On the other hand, Discrete Tomography comprises the techniques focused on reconstructing images that consist of only a few attenuation coefficients. In the following subsections, methods for Continuous and Discrete Tomography are exposed.

2.3.1 Continuous tomography

Such reconstruction methods are typically divided into two classes: the Analytical Reconstruction Methods and the Iterative Techniques. The first one, based on the Fourier Slice Theorem, is the most used in present-day CT systems due its simplicity and efficiency. The second one finds approximate reconstructions within successive iterations of an algorithm. Despite computationally expensive, the Iterative Techniques has been attracting the attention of researchers due to its flexible operation with many distinct scanning geometries, the possibility of incorporating prior knowledge into the process, and the fast increase of computational power available nowadays.

Short overviews of the Analytical and Iterative reconstruction methods are presented in the following subsections. The reader may find a complete description of those methods in (KAK et al., 1988) and (BUZUG, 2008). The following subsections were also written based on the concise and clear explanations presented in (AARLE, 2012). For the sake of simplicity, in subsections 2.3.1.1 and 2.3.1.2, it is considered the parallel beam projection setup, *i.e.*, a scanning geometry in which all the projection rays are parallel to each other for every projection direction. Nevertheless, the theory presented in this section is extensible to every scanning geometry.

2.3.1.1 *Analytical reconstruction methods*

The *Fourier Slice Theorem* states that the one-dimensional Fourier transform of the projection function $g(\rho, \theta)$ [6] is equal to the to the slice through the origin at rotation θ of the two-dimensional Fourier space $F(\omega_1, \omega_2)$ of the o object function $f(x, y)$.

[4] for a detailed description of the domains involved in a CT processing, see Appendix A.
[5] for a detailed description of Inverse Radon Transform, see Appendix B
[6] the notation $g(\rho, \theta_k)$ is introduced in Appendix B.

Therefore, by sampling projections at angles $\theta_1, \theta_2, \cdots, \theta_K$, and Fourier transforming each $g(\rho, \theta_k)$, we can determine the values of $F(\omega_1, \omega_2)$ on radial lines, as shown in Figure 9. If an infinite number of projections were available, the object function $f(x, y)$ would be restored by using the Inverse Fourier Transform according to the Equation 2.1.

$$\hat{f}(x, y) = \int_{-\infty}^{\infty} \int_{-\infty}^{\infty} F(\omega_1, \omega_2) e^{j2\pi(\omega_1 x + \omega_2 y)} d\omega_1 d\omega_2 \tag{2.1}$$

such that $\hat{f}(x, y)$ is the reconstructed image.

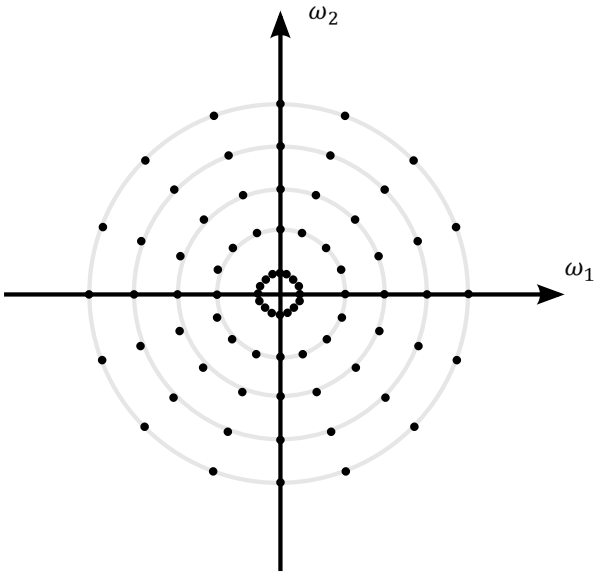

Figure 9 – According to the *Fourier Slice Theorem*, it is possible to find out the representation of the object function $f(x, y)$ in the frequency domain by sampling many projection functions, related to different angles θ_k, in the frequency domain.

In practice, only a finite number of projections can be acquired. Moreover, the interpolation error in $\omega_1\omega_2$-plane (see Figure 9) becomes larger as the points get further from the center. It implies that there is a great error on the high-frequency components interpolated, which would result in some image degradations.

The most popular Analytical Reconstruction Method is the Filtered Back Projection (FBP). To derive the FBP algorithm based on Equation 2.1, let us first exchange the rectangular coordinate system in the frequency domain, (ω_1, ω_2), for a polar coordinate system, (ρ, θ), by applying the following

$$\begin{aligned} \omega_1 &= \rho \cos\theta, \\ \omega_2 &= \rho \sin\theta, \\ d\omega_1 d\omega_2 &= \rho d\rho d\theta \end{aligned}$$

the Equation 2.1 then becomes:

$$\hat{f}(x,y) = \int_0^{2\pi} \int_0^{\infty} F(\rho,\theta) e^{j2\pi\rho(x\cos\theta + y\sin\theta)} \rho d\rho d\theta \tag{2.2}$$

Since $F(\rho, \theta + \pi) = F(-\rho, \theta)$, the integration limits are changed and Equation 2.2 becomes:

$$\hat{f}(x,y) = \int_0^{\pi} \left[\int_{-\infty}^{\infty} F(\rho,\theta)|\rho| e^{j2\pi\rho(x\cos\theta + y\sin\theta)} d\rho \right] d\theta \tag{2.3}$$

According to the *Fourier Slice Theorem*, $F(\rho, \theta)$ is equal to the Fourier transform of the projection $g(\theta, \rho)$ at a fixed angle θ, *i.e.* $G_\theta(\rho)$. Therefore, the process on finding out the reconstructed image $\hat{f}(x, y)$ can be described by:

$$\hat{f}(x,y) = \int_0^{\pi} \left[\int_{-\infty}^{\infty} G_\theta(\rho)|\rho| e^{j2\pi\rho(x\cos\theta + y\sin\theta)} d\rho \right] d\theta \tag{2.4}$$

By defining the signal $q_\theta(t)$ as the inverse Fourier transform of $G_\theta(\rho)$ weighted by $|\rho|$, as follows

$$q_\theta(t) = \mathcal{F}^{-1}\{G_\theta(\rho)|\rho|\} = \int_{-\infty}^{\infty} G_\theta(\rho)|\rho| e^{j2\pi\rho t} d\rho \tag{2.5}$$

the Equation 2.4 than becomes:

$$\hat{f}(x,y) = \int_0^{\pi} q_\theta(x\cos\theta + y\sin\theta) d\theta \tag{2.6}$$

Equation 2.5 describes the first step of FBP algorithm: each projection function $g_\theta(\rho)$ is **filtered** by multiplying its Fourier transform with $|\rho|$; this operation compensates the lower sampling density in high frequencies of the Fourier domain (see Figure 9). The second step of FBP algorithm is described in Equation 2.6: the filtered projection data is then **backprojected** (or "smeared out") onto the reconstruction grid along the lines $t = x\cos\theta + y\sin\theta$.

2.3.1.2 *Iterative Techniques*

The Algebraic Reconstruction Techniques (ART) are the subset of the Iterative Techniques most used in the literature. ART states the reconstruction problem as the solving of a system of linear equations. In such methods the image reconstruction resolution, *i.e.*, the number of pixels used to represent the field of view, is determined before the reconstruction takes place. Therefore, the tomographic image consists of a discrete array of unknown variables f_j, for $j = \{1, 2, \cdots, N\}$. Figure 10 illustrates such array for $N = 9$. Let p_i be the ray level intensity measured with the $i-th$ detector, as shown in Figure 10. The relation between f_j and p_i is given by:

$$p_i = \sum_{j=1}^{N} a_{ij} f_j, i = \{1, 2, 3, \cdots, M\} \tag{2.7}$$

such that M is the total number of rays and a_{ij} is a weighting factor which measures the contribution of the $j-th$ image cell to the $i-th$ ray path. For instance, the value a_{ij} may be equal to the length of intersection between the $i-th$ ray path and the $j-th$ image cell, as shown in Figure 10.

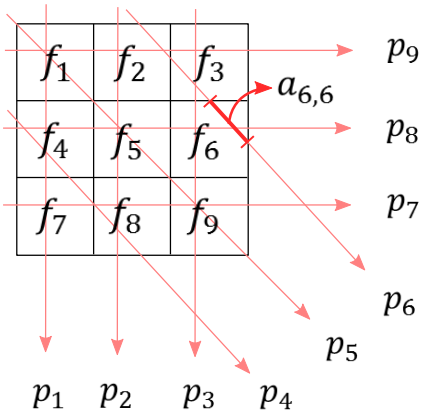

Figure 10 – In algebraic methods, the field of view is partitioned into a grid of N cells before the reconstruction takes place. Then, a projection intensity p_i is measured by summing proportionally all the image cells which interact to the $i-th$ ray path.

By expanding Equation 2.7, the following linear system of equations raises:

$$\begin{aligned} a_{1,1}f_1 + a_{1,2}f_2 + a_{1,3}f_3 + \cdots + a_{1,N}f_N &= p_1 \\ a_{2,1}f_1 + a_{2,2}f_2 + a_{2,3}f_3 + \cdots + a_{2,N}f_N &= p_2 \\ &\vdots \\ a_{M,1}f_1 + a_{M,2}f_2 + a_{M,3}f_3 + \cdots + a_{M,N}f_N &= p_M \end{aligned} \tag{2.8}$$

which is simple $\mathbf{Af} = \mathbf{p}$. If M and N are equal and also small, there are conventional matrix theorem methods to invert A and find $\mathbf{f} = \mathbf{A^{-1}p}$. In practice N is larger than $65,000$ (for 256×256 reconstruction images), and M should have the same magnitude (to achieve an equal number of unknowns and equations in the linear system presented in 2.8). Then, the matrix $\mathbf{A}$ is larger than $65,000 \times 65,000$ which makes the direct matrix inversion approach impracticable. Moreover, when noise is present in the measured data or when $M < N$, that trivial solution becomes undetermined.

One of the ART methods able to find good approximations to the solution of the linear system of equations presented in 2.8, considering realistic values for M and N, is the Simultaneous Iterative Reconstruction Technique (SIRT) (GORDON; BENDER; HERMAN, 1970): starting with an initial solution $\mathbf{f}^{(0)}$ (typically $\mathbf{f}^{(0)} = 0$, *i.e.* a black image), and an iteration counter $k = 0$, SIRT runs successive iterations. Each of those is composed by the following steps:

1. Computation of the forward projection related to the current reconstruction image:

$$\mathbf{p}^{(k)} = \mathbf{A}\mathbf{f}^{(k)} \tag{2.9}$$

2. Computation of the current projection difference in relation to the measured projection. It is also called as *residual sinogram*:

$$\mathbf{r}^{(k)} = \mathbf{p} - \mathbf{p}^{(k)} \tag{2.10}$$

3. Update the reconstruction image $f^{(k)}$ by adding a weighted backprojection of the residual sinogram:

$$\mathbf{f}^{(k+1)} = \mathbf{f}^{(k)} + \mathbf{C}\mathbf{A}^T\mathbf{R}\mathbf{r}^{(k)} \tag{2.11}$$

in which $\mathbf{R}$ is a diagonal matrix of the inverse row sums of $\mathbf{A}$ and $\mathbf{C}$ is a diagonal matrix of the inverse column sums of $\mathbf{A}$.

2.3.2 Discrete tomography

These methods assume that the scanned object is composed of only a few homogeneity materials. In Discrete Tomography, the number and the value of gray levels of the reconstructed image (*i.e.*, attenuation coefficients in the object) are usually known in advance (BATENBURG; SIJBERS, 2009).

A recent proposed method is the Discrete Algebraic Reconstruction Technique (DART) (BATENBURG; SIJBERS, 2011a). DART is based on the interleaving of continuous update steps and discretization steps. The flow chart of Figure 11 shows the sequence of stages which compose the DART algorithm. Then, each DART stage is explained in the following list:

- **To compute an initial ART reconstruction:** DART starts with an initial reconstruction of the acquired data p obtained with a continuous iterative reconstruction algorithm, such as SIRT.
- **To segment the reconstruction:** the reconstruction is segmented according to the set of gray values $(\rho_1, \rho_2, \ldots, \rho_\iota)$ that is expected for the image. In fact, since the gray values of the reconstructed image are associated with the attenuation coefficients of the target object in each region, this incorporated prior knowledge is related to the expected density of the materials of which the object is composed. In this stage, $\iota - 1$ thresholds (τ_i) are applied to the image, defined as:

$$\tau_i = \frac{\rho_i + \rho_{i+1}}{2} \tag{2.12}$$

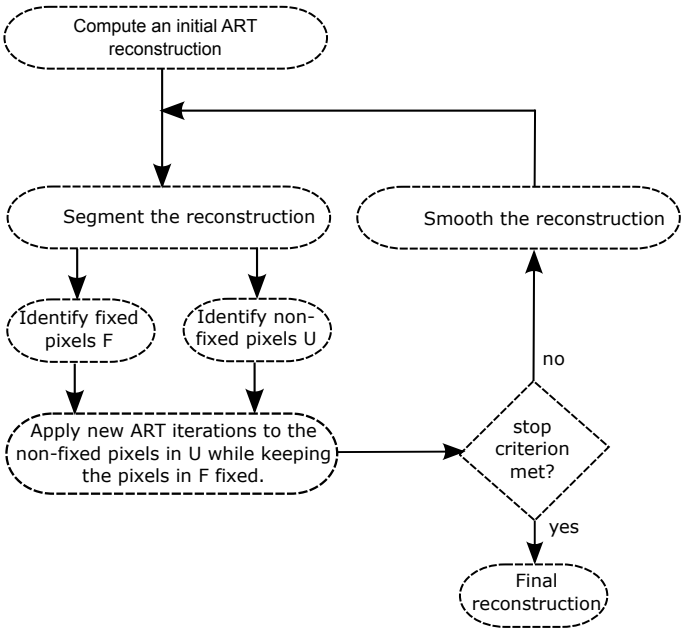

Figure 11 – Flow chart of DART algorithm.

- **To identify non-fixed pixels U:** Let $U^{(k)} \in \{1, 2, \ldots, n\}$ be the set of pixels to be updated in the $k-th$ iteration of DART. Since experimental results showed that ART leads to errors near the edges of the reconstructed image, all boundary pixels of the current segmented image are thus added to $U^{(k)}$. For this purpose, every pixel which value is different from at least one of its neighboring pixels is considered a boundary pixel. Moreover, each non-boundary pixel is added to $U^{(k)}$ with a certain probability $0 \leq r \leq 1$. In this way, the accuracy of DART reconstruction is increased in the case of small holes or features which were missed during the initial reconstruction.

- **To identify fixed pixels F:** After defining a set of non-fixed pixels $U^{(k)}$, the complementary set of pixels that must not be updated in the $k-th$ iteration of DART is defined as $F^{(k)} = \{1, 2, \ldots, n\} \setminus U^{(k)}$. In other words, $F^{(k)}$ contains all pixels that will be removed from the reconstruction problem in the next stage of DART flowchart.

- **To apply new ART iterations to the pixels in U while keeping the pixels in F fixed:** Since the linear system of equations presented in Equation 2.8 can be written as:

$$p = \begin{pmatrix} \vdots & \vdots & \vdots \\ a_1 & \cdots & a_n \\ \vdots & \vdots & \vdots \end{pmatrix} \cdot \begin{pmatrix} f_1 \\ \vdots \\ f_n \end{pmatrix} \tag{2.13}$$

where a_j denotes the $j-th$ column of the matrix A, the f_j pixel can be made fixed and removed to the reconstruction problem if the Equation 2.13 is converted in the Equation 2.14.

Then, an ART iteration can be applied for this new linear system which has the same number of equations of 2.13 and a lower number of variables.

$$p - a_j f_j = \begin{pmatrix} \vdots & \vdots & \vdots & \vdots & \vdots & \vdots \\ a_1 & \cdots & a_{j-1} & a_{j+1} & \cdots & a_n \\ \vdots & \vdots & \vdots & \vdots & \vdots & \vdots \end{pmatrix} \cdot \begin{pmatrix} f_1 \\ \vdots \\ f_{j-1} \\ f_{j+1} \\ \vdots \\ f_n \end{pmatrix} \tag{2.14}$$

- **Stop criterion met:** The consecutive iterations of DART are usually stopped based on a fixed number of iterations.
- **Smooth the reconstruction:** Reducing the number of variables by selecting a subset of non-fixed pixels $U^{(k)}$ may lead to more noise sensitive ART reconstructions. Then, a Gaussian smoothing filter is applied to the boundary pixels after applying the ART.

2.4 The limited data problem

Image errors that may emerge in CT reconstructions due to a variety of reasons are called artifacts. Two of those reasons are (i) the acquisition of only a few number of X-ray projections (*i.e.*, low-sampling), and (ii) the acquisition within a non-complete angular around the object (*i.e.*, partial angular sampling) as illustrated in Figure 12. In the second case, the non-sampled image views are referred to as missing wedges.

By limiting the acquired X-ray data, the radiation exposure time is reduced. This is desired for two main reasons: *(i)* in medical imaging, it can reduce the risk of fatal cancer in patients (SMITH-BINDMAN et al., 2009); and *(ii)* in industrial imaging, the scanning time resolution[7] can be highly improved.

[7] for a detailed description on time resolution, see Section 1.4.

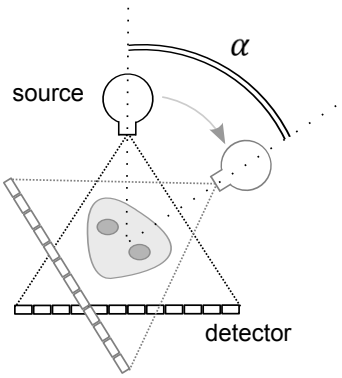

Figure 12 – Example of an X-ray CT scanning using a limited view angle of α. The non-sampled image views are referred as missing wedges.

3 PROBLEM STATEMENT

This chapter presents the performance of conventional reconstruction techniques in a simple setup for fast CT scanning comprising a statically positioned pair of X-ray source and detector for imaging objects passing on a conveyor belt. The analysis of the results is guided based on both reconstruction quality and time and should be used as a baseline for comparison purposes with the methods further proposed in this thesis. In Section 3.1, the inline scanning geometry is described; in Section 3.2, experiments show the performance of standard techniques operating in that system.

3.1 The inline scanning geometry

The inline setup used in this work is exposed in Figure 13. It comprises a static wide cone X-ray source (a) and a large detector (b) for imaging objects (c) passing by on a conveyor belt (d). Since such setup comprises no moving parts, the data acquisition is cheaper and faster than in conventional CT systems at which the X-ray source and the detector rotate around the object. That setup has been widely used with traditional radiographs for quality assurance in industrial environments (PIERCE et al., 1993; EILBERT; SHI, 2005) and for luggage inspection in airports (DENNHOVEN; KUNZE; KUEHN, 1977; DENNHOVEN; KUNZE; KUEHN, 1979). However, due to the expressive missing wedge inherent in such setup, it is not used for X-ray CT. Recently, Janssens *et al.* (JANSSENS et al., 2016a) used a similar scanning setup in their work. However, the system proposed by them was composed of a non-fixed X-ray detector which follows the scanned object trajectory to avoid the acquisition of truncated projections near detector borders. In this thesis, we suggest that the use of a static positioned detector is simpler and cheaper. Then, reconstruction issues related to the existence of truncated projections should be solved via software.

A more precise diagram of the relation between the scanned object and the X-ray projections in the proposed inline scanning setup is presented in Figure 14. The parameters of such geometry are described as follows:

- **D**: the vertical distance between the object and the X-ray source.
- **B**: the vertical distance between the conveyor belt and the detector.
- **2a**: the dimension of the rectangular region to be reconstructed.
- **2L**: the detector length.
- **2**α: the X-ray fan-beam opening angle.

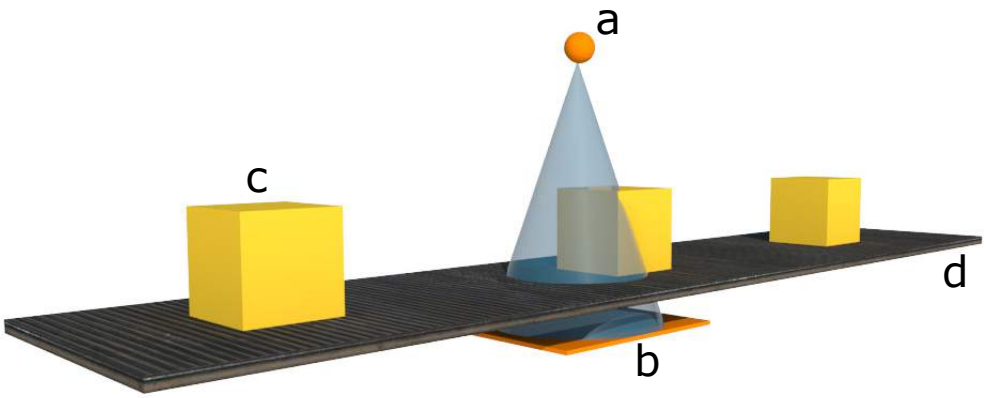

Figure 13 – Overview of the inline scanning geometry for X-ray CT: a static setup consisting of a wide cone X-ray source and a large detector for imaging object passing on a conveyor belt.

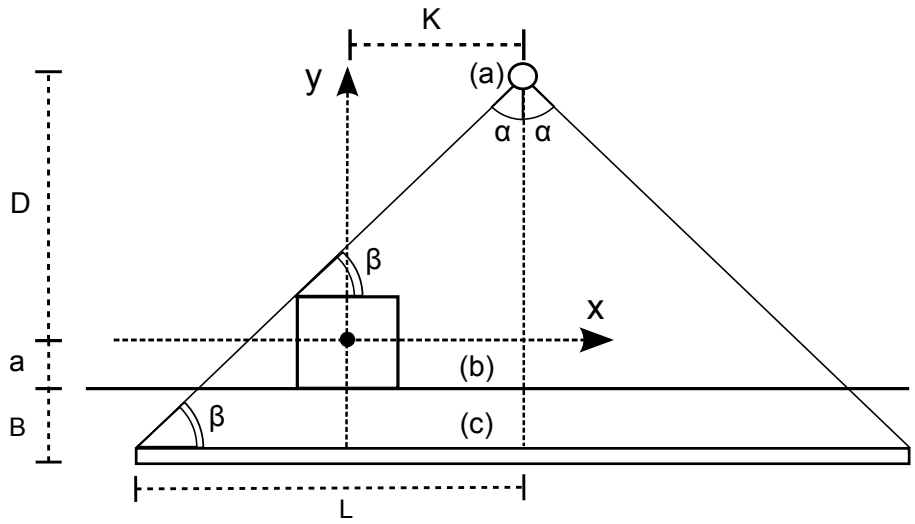

Figure 14 – Reference frame of the inline scanning geometry evaluated in this work. The system is composed by a wide cone X-ray source (a), a conveyor belt (b), and a large detector (c).

Three main constraints are imposed on the data acquisition in the proposed inline scanning geometry. This constraints bring a huge challenge to the image reconstruction process. They are exposed as follows:

- **Limited fan-beam angular range:** due to physical limitations, the X-ray cone angle (2α) is limited to 60°. Therefore, the object is scanned from very limited angular views.
- **Limited number of projections:** since the conveyor belt must be totally stopped for each X-ray projection acquisition, only a few number of projections should be acquired to allow a great translation velocity in the conveyor belt.
- **Truncated projections:** some projection information is lost near the detector

borders. In fact, the object is only complete entailed by the X-ray fan-beam when the horizontal distance K between the object and the X-ray source is no longer than K_{max}. From Figure 14, the value of K_{max} is calculated as follows:

$$\tan\beta = \frac{D-a}{K_{max}+a} = \frac{D+B+A}{L} \tag{3.1}$$
$$K_{max} = \frac{(D-a)\cdot L}{(D+B+a)} - a$$

Figure 15 highlights the differences of the projection configurations among (a) the full-sampled symmetrical case at circular scanning geometry, (b) the low-sampled asymmetrical case at circular scanning geometry, and (c) the low-sampled inline scanning geometry used in this thesis.

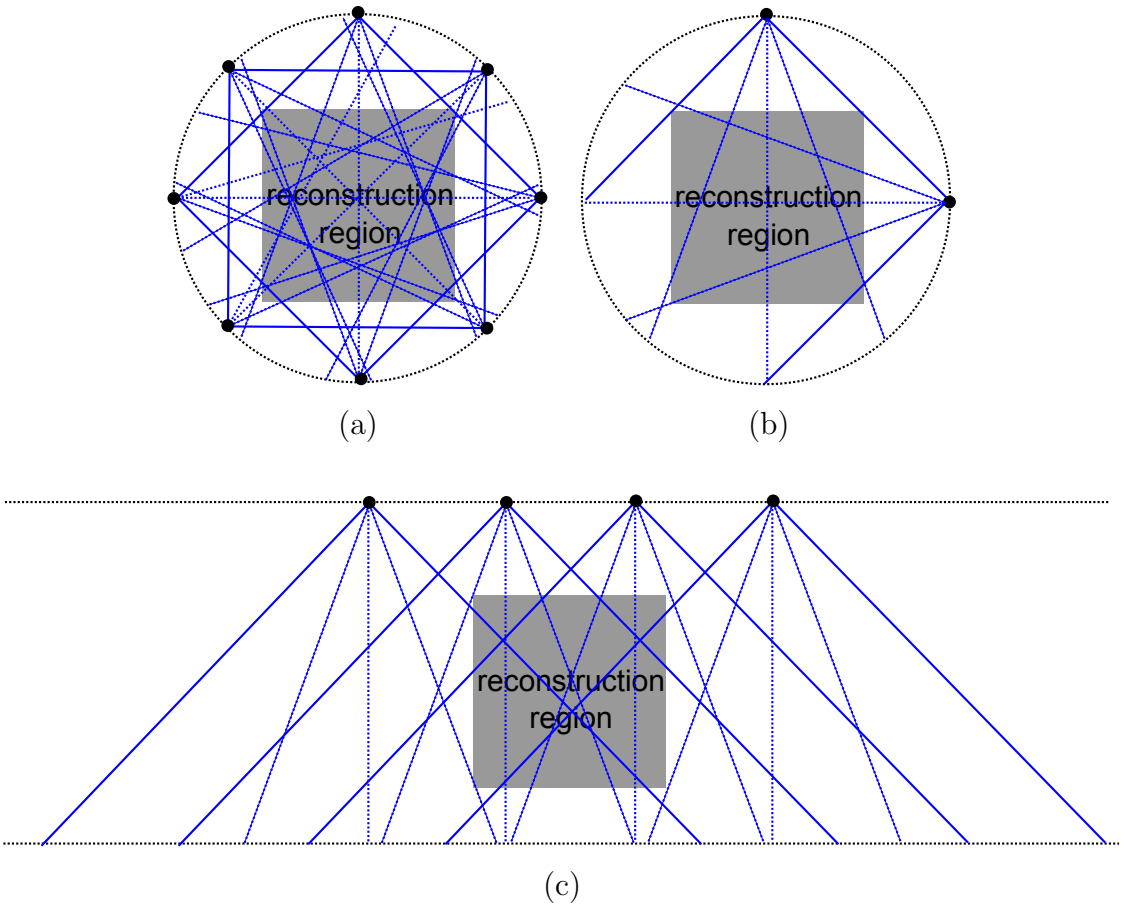

Figure 15 – Differences within the projection configurations among (a) the full-sampled symmetrical case at circular scanning geometry, (b) the low-sampled asymmetrical case at circular scanning geometry, and (c) the low-sampled inline scanning geometry used in this thesis.

An alternative approach that should also be evaluated to deal with the low number of object's view in the inline scanning setup consists of allowing some object rotation while it is linearly translated on the conveyor belt. Figure 16 (a) illustrates such rotation

along the time, and Figure 16 (b) shows a design of gears that can be used to allow the proposed movement of objects in the conveyor belt. In this thesis, we describe object's angular speed by the arch θ covered by a fixed point in the object during the scanning process.

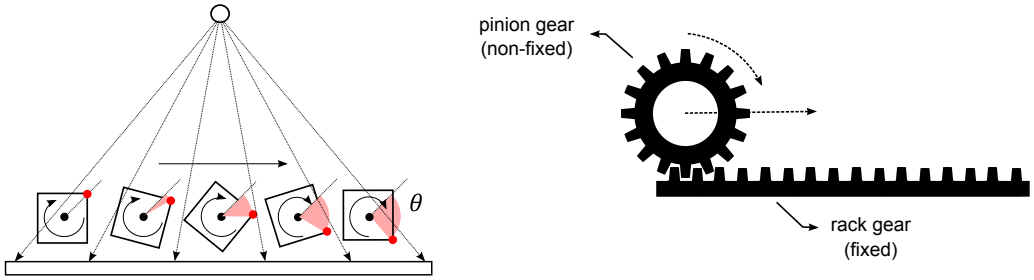

(a) (b)

Figure 16 – Object rotation of θ in the conveyor belt during a linear translation (a); and the devices suggested to promote both rotation and translation of the object in the conveyor belt (b): a non-fixed pinion gear is attached to a fixed rack gear, the desired movement is produced as the pinion gear rolls over the rack gear.

3.2 Simulations

Every simulation in this thesis was made using the ASTRA-Toolbox (AARLE et al., 2016) that provides a convenient framework for the development of advanced tomographic reconstruction techniques. Furthermore, real X-ray CT image reconstructions of Jonagold apples and Bell peppers acquired at BIOSYST-MeBios, KU Leuven, Belgium were used as phantoms. A phantom models object's material response to a specific type of radiation. As a result, phantoms are used in simulations and evaluations of many imaging systems.

3.2.1 Data set

The real CT images were acquired in a conventional circular scanning geometry using around 500 projections. Conventional FBP was used to reconstruct more than 1600 cross-section images of apples and peppers. Figure 17 shows four of those images of Jonagold apples (a-d) and Bell peppers (e-h).

3.2.2 Results and discussion

The phantoms described in Section 3.2.1 were used to simulate acquisition of projections in the inline scanning geometry introduced in Section 3.1. Thus, such projections were reconstructed using conventional techniques. Figures 18 and 19 show reconstructed samples of Jonagold apples using FBP and SIRT, respectively. Image results are shown for

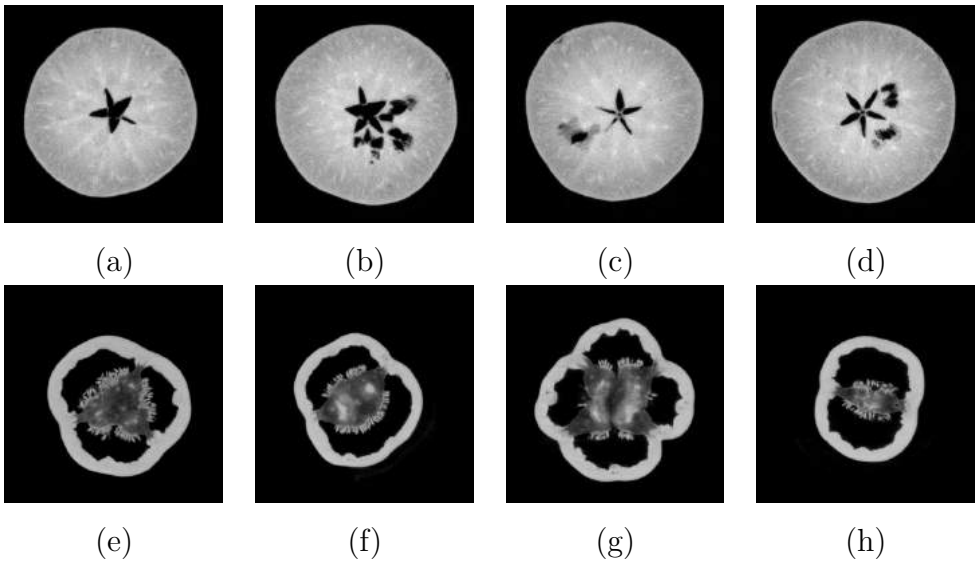

Figure 17 – Examples of real X-ray CT reconstruction of Jonagold apples (a-d) and Bell peppers (f-h) used in this work as phantoms. (**Source:** image reconstructions acquired at BIOSYST-MeBios, KU Leuven, Belgium).

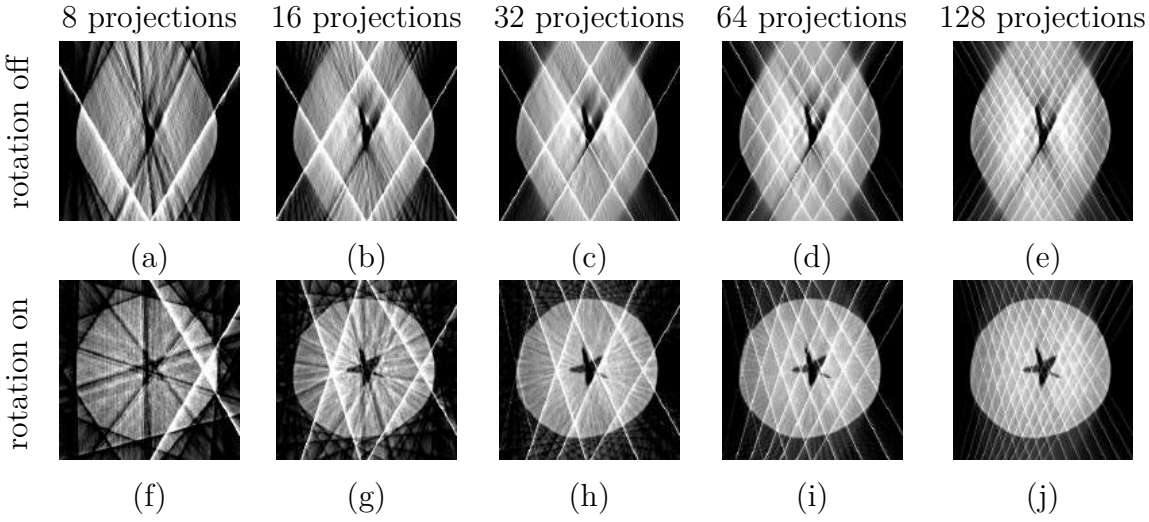

Figure 18 – Reconstructed samples of Jonagold apples reconstructed using FBP and distinct numbers of X-ray projections: 8 in (a) and (f), 16 in (b) and (g), 32 in (c) and (h), 64 in (d) and (i), and 128 in (e) and (j). Moreover, the first line (a-e) shows results obtained with object rotation disable ($\theta = 0°$) and second line (f-j) shows results obtained with object rotation enable ($\theta = 180°$).

experiments using distinct numbers of X-ray projections and turning on and off the mechanism responsible for rotating the object in the conveyor belt (described in Figure 16). Figures 20 and 21 show similar results using the Bell pepper dataset.

The reconstruction images observed in Figures 18 to 21 shows that SIRT is more suited than FBP to reconstruct CT images from projections acquired in the inline scanning geometry. The choice of using SIRT goes in opposite direction of most of CT systems that use FBP due its fast processing time. However, it is clear the low-quality level of

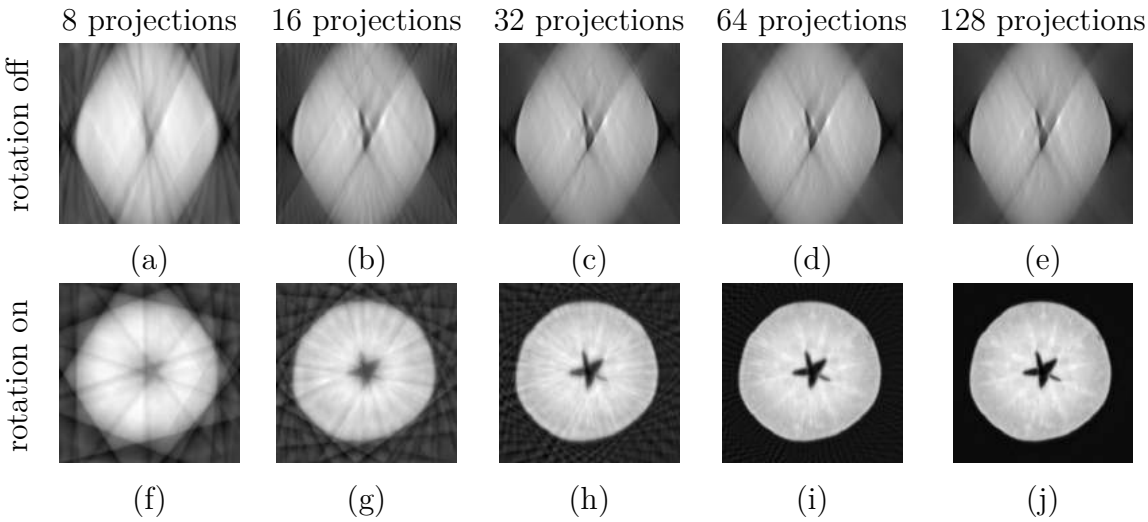

Figure 19 – Reconstructed samples of Jonagold apples reconstructed using SIRT and distinct numbers of X-ray projections: 8 in (a) and (f), 16 in (b) and (g), 32 in (c) and (h), 64 in (d) and (i), and 128 in (e) and (j). Moreover, the first line (a-e) shows results obtained with object rotation disable ($\theta = 0°$) and second line (f-j) shows results obtained with object rotation enable ($\theta = 180°$).

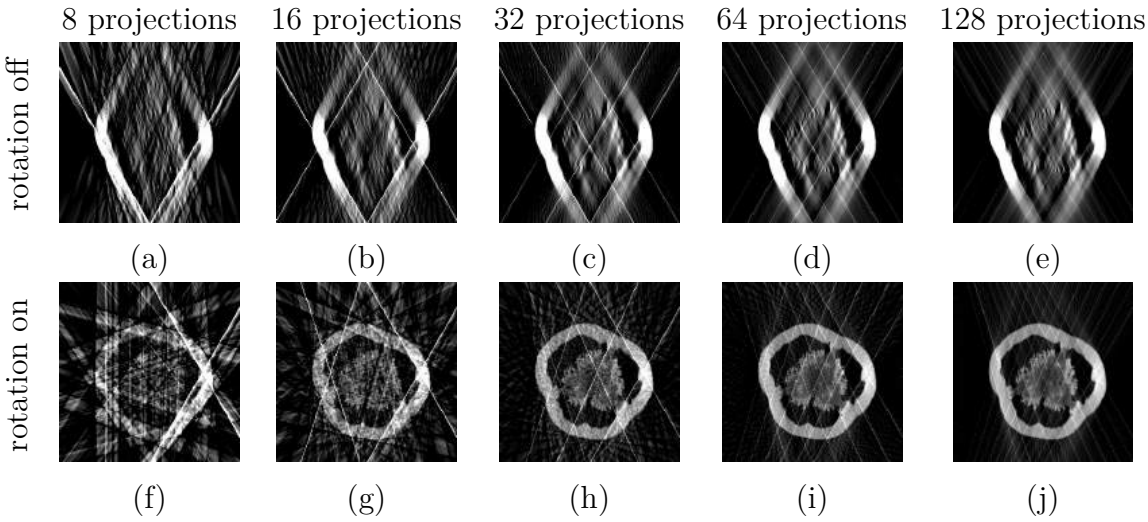

Figure 20 – Reconstructed samples of Bell peppers reconstructed using FBP and distinct numbers of X-ray projections: 8 in (a) and (f), 16 in (b) and (g), 32 in (c) and (h), 64 in (d) and (i), and 128 in (e) and (j). Moreover, the first line (a-e) shows results obtained with object rotation disable ($\theta = 0°$) and second line (f-j) shows results obtained with object rotation enable ($\theta = 180°$).

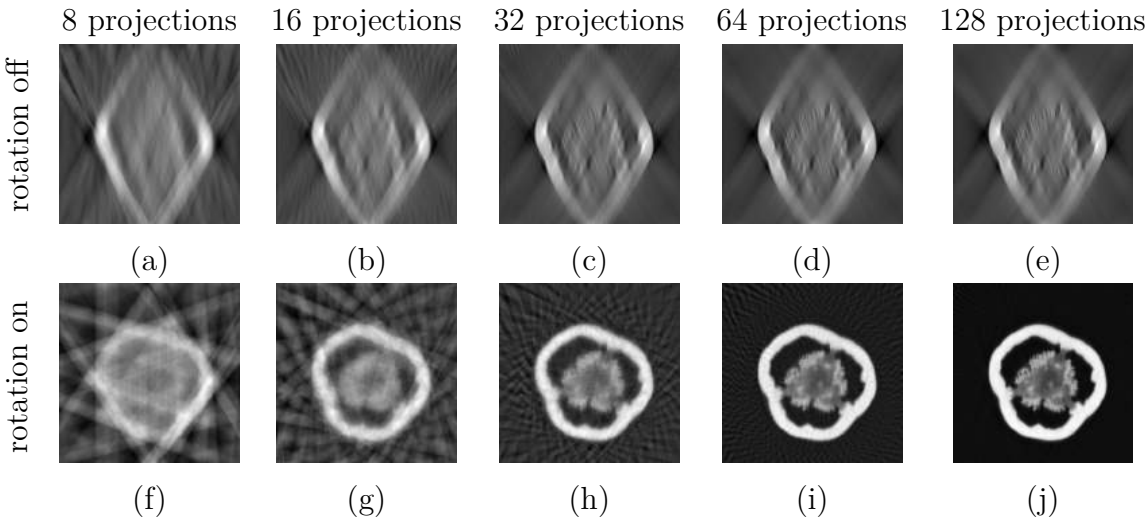

Figure 21 – Reconstructed samples of Bell peppers reconstructed using SIRT and distinct numbers of X-ray projections: 8 in (a) and (f), 16 in (b) and (g), 32 in (c) and (h), 64 in (d) and (i), and 128 in (e) and (j). Moreover, the first line (a-e) shows results obtained with object rotation disable ($\theta = 0°$) and second line (f-j) shows results obtained with object rotation enable ($\theta = 180°$).

FBP reconstructions in the inline scanning geometry. The experimental tests conducted to elaborate this work showed that the crossed white lines observed in every FBP reconstruction are due to the existence of truncated projections. However, such limitation is inherent to the inline scanning geometry presented in this thesis.

Furthermore, although the scanning setup without object rotation is preferable due to the final system's cost, the reconstruction results showed that the rotation feature is crucial to obtain accurate reconstruction results. In fact, the association of SIRT, and at least 32 X-ray projections, and a conveyor belt with object rotation produces reconstructions of enough quality for object inspection purposes. However, no evaluation of the system's throughput has been conducted until this point.

The throughput of the CT imaging setup is determined by both the scanning and reconstruction time. The scanning time is a function of the number of projections acquired because, in a step-and-shoot mode, the conveyor belt must stop totally for each X-ray projection acquisition. Simulations to estimate the scanning time were performed assuming acceleration/deceleration values compatible with the study published by (HE; PANG; LODEWIJKS, 2016). Moreover, it was considered an X-ray detector composed of 350 cells of 1 mm each and an acquisition time of 50 ms per projection. The scanning times obtained are shown in Figure 22 for conveyor belt's acceleration/deceleration of 0.1 m/s^2, 0.05 m/s^2, and 0.025 m/s^2. On the other hand, the reconstruction time is a function of the desired final image resolution and the number of X-ray projections used. Figures 23 and 24 show the reconstruction time measured for creating images of resolution of 128×128, 256×256, and 512×512 using FBP and SIRT, respectively.

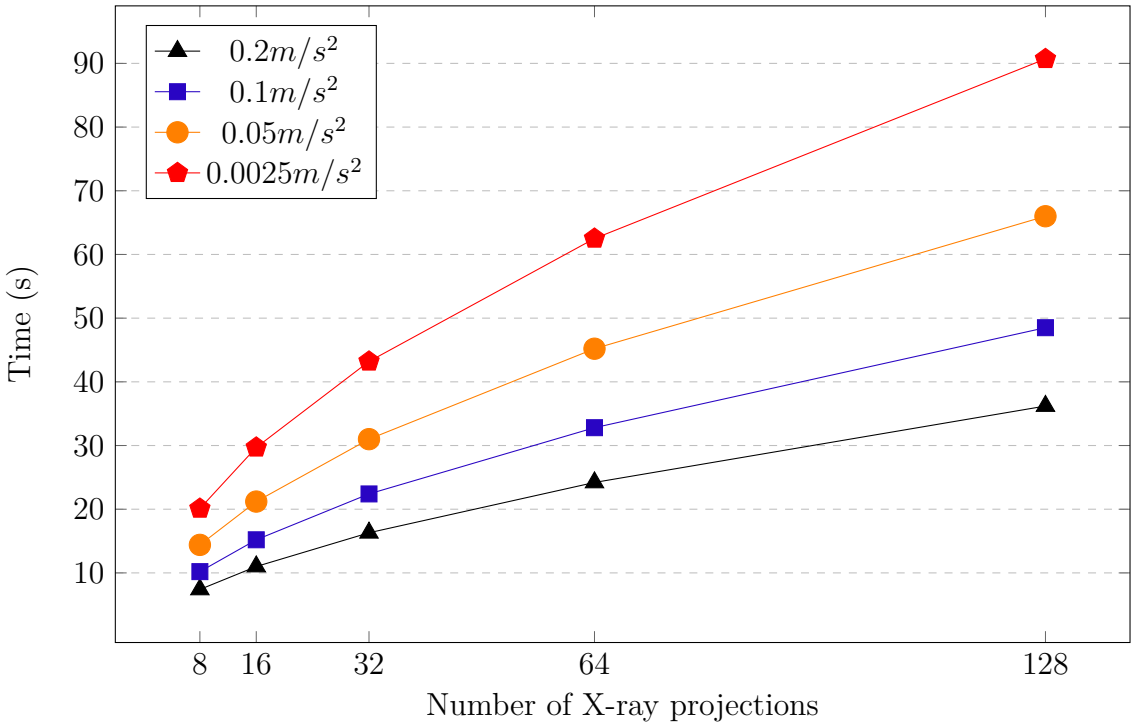

Figure 22 – Scanning time using different numbers of X-ray projections.

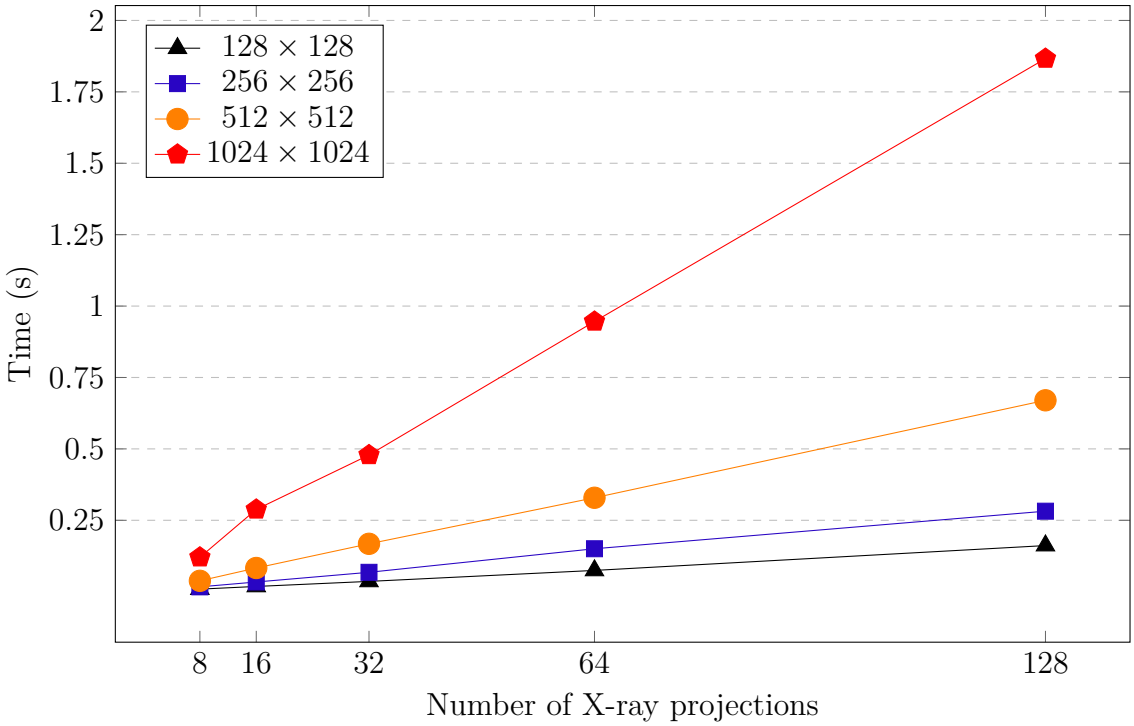

Figure 23 – Reconstruction time using FBP using different numbers of X-ray projections.

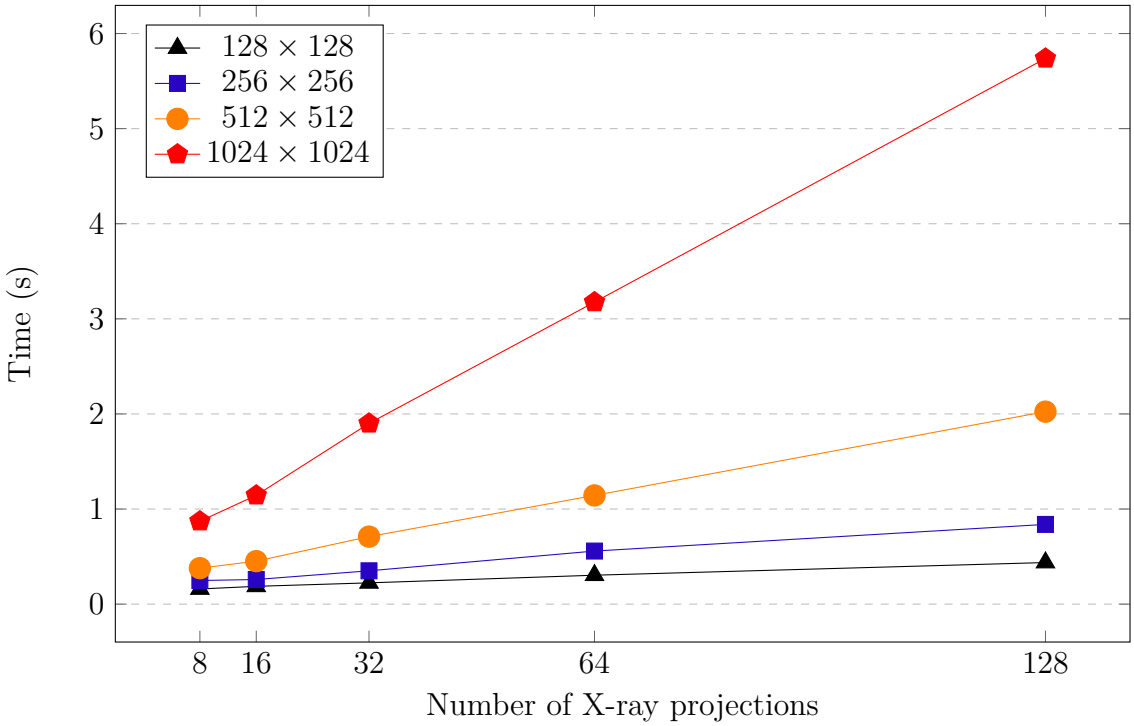

Figure 24 – Reconstruction time using SIRT using different numbers of X-ray projections.

The analysis of Figures 22 to 24 shows that the elapsed time during the reconstruction phase, using either FBP or SIRT, is less relevant than the time elapsed during the scanning phase to compose the final system's processing time. This way, a direct approach that should guide the development towards a higher throughput inline CT system is *to reduce the number of X-ray projections while keeping the quality of the reconstruction image.*

4 RELATED WORKS

Software-based improvements to the Computed Tomography workflow have been proposed in the state-of-the-art to handle with scenarios at which Low-Dose Computed Tomography (LDCT) is required due to *(i)* the X-ray dose must be limited to safe levels[1] or *(ii)* the elapsed time to collect the ideal number of X-ray projections is prohibitively long. The basic idea behind most of the works which deal with low-dose scenarios is to incorporate priors into the reconstruction process; they may be incorporated into three distinct stages of the workflow (see Figure 3): pre-reconstruction, reconstruction, or post-reconstruction. The next three sections presents distinct approaches proposed along the latest years to introduce priors at distinct stages of the CT imaging workflow.

4.1 Pre-reconstruction

The techniques which process sinograms using priors before the reconstruction stage are focusing on solving two distinct problems: *(i)* sinogram denoising and *(ii)* sinogram interpolation or inpainting. Each of these is described as follows:

(i) sinogram denoising aims at suppressing noise that arises in sinogram data due to the use of some strategies for LDCT, such as: decrease the current and/or the voltage at the electrical circuit of the X-ray source;

(ii) sinogram interpolation or inpainting aims at generating non-measured projection samples based on the available projections. In both cases, those methods are usually succeeded by conventional reconstruction techniques.

In the following subsections, it is shown the evolution of the techniques for sinogram denoising and sinogram interpolation or inpainting along the latest years. In the end, considerations about the most suitable pre-reconstruction techniques for the inline scanning system described in this work are summarized.

4.1.1 Sinogram denoising

The methods for sinogram denoising can be categorized into *(i)* statistical- or *(ii)* weighted filtering-based methods. Each of those is described as follows:

[1] some of the technical guidelines to develop machines which operate with less radiation are (LEE; CHHEM, 2010): *(i)* modulate the electrical current in the X-ray tube, *i.e.*, the current is increased (decreased) at angles where there are more (less) attenuation because the patient/object thickness is large (small); and *(ii)* reduce the number of X-ray projections used.

(i) the statistical-based methods use measures (*e.g.*, mean and variance) about the noise observed in the similar sinograms to enhance the data using statistical tools such as Weighted-Least Squares (WLS), Maximum A Posteriory (MAP), and Maximum Likelihood (ML);

(ii) the weighted filtering-based methods apply weighted sums to similar sinograms or distinct parts of the same sinogram to suppress noise and emphasize non-corrupted areas. In fact, such filtering has strong origins in MAP estimation (MANDUCA et al., 2009).

In the following subsections, the most significant statistical- and weighted filtering-based methods developed up to the present date for sinogram denoising are presented.

4.1.1.1 *Statistical-based methods*

In (LU et al., 2002), it is shown that the noise in the evaluated LDCT projection data can be regarded as normally distributed with a nonlinear signal-dependent variance. Thus, it is proposed a Penalized Weighted Least-Square (PWLS) smoothing framework which incorporates statistical noise properties. In fact, PWLS estimates the ideal projection by minimizing a specific cost function. A similar approach was discussed later by (LI et al., 2004) and (WANG et al., 2006).

In (RIVIERE, 2005) and (KARIMI; WARD, 2016), the authors propose the estimation of noise-free sinograms by maximizing likelihood objective functions. Those works differ on the algorithm used in the optimization problem, and (KARIMI; WARD, 2016) also uses the sparsity in the gradient domain as a regularization term.

In (WANG et al., 2008), it is proposed a multiscale approach where a PWLS smoothing strategy enhances a sinogram data in the wavelet domain. Experimental analysis showed that the proposed multiscale approach leads to better reconstruction results than the previous single-scale approaches.

4.1.1.2 *Weighted filtering-based methods*

In (BORSDORF et al., 2008), the weights used for sinogram filtering are generated according to the similarity of the Wavelet coefficients in the images generated by the even and odd numbered projections. More precisely, the closer is the correlation between the Wavelet coefficients, the higher is the probability that is a true structure in the object and such composition should remain; the lower is the similarity value between the Wavelet coefficients, the higher is the probability that the corresponding detail coefficient includes only noise and should be suppressed. To maintain a Wavelet coefficient, the filter weights are set as high; to suppress it, the filter weights are set as low.

In (MANDUCA et al., 2009), it is proposed a method for sinogram smoothing based on bilateral filtering which was initially proposed for additive noise removal (ELAD, 2002).

The authors claim that such approach can perform noise reduction while preserving structural details. A similar approach was also proposed by (BALDA; HORNEGGER; HEISMANN, 2012).

4.1.2 Sinogram interpolation or inpainting

The methods for sinogram interpolation or inpainting can be categorized into *(i)* gradient-, *(ii)* image registration-, *(iii)* dictionary learning-, or *(iv)* Artificial Neural Network (ANN)-based methods. Each of those is described as follows:

(i) the gradient-based methods aim to estimate variation rules of gray values among neighbor pixels in under-sampled sinogram images to fill in unmeasured views;

(ii) the image registration-based methods looks up to a set of correct sampled sinograms acquired at CT scans of similar objects. Therefore, the most similar sinogram is used to restore the unmeasured views from the under-sampled sinogram;

(iii) the Dictionary Learning-based methods generate a new representation of the sinogram data based on atomic signals free of artifacts which were previously learned from a training set;

(iv) the Artificial Neural Network (ANN)-based methods use a set of under-sampled and full-sampled sinograms to train mathematical models able to generate a mapping function from under- to full-sampled sinograms.

In the following subsections, the most significant gradient-, image registration-, dictionary learning- and neural network-based methods developed up to the present date for sinogram interpolation or inpainting are presented.

4.1.2.1 *Gradient-based methods*

In (BERTRAM et al., 2004) and (BERTRAM et al., 2009), structure tensors are used to estimate the orientation of gray value changes in local neighborhoods. That information is then used to perform a directional interpolation at missing regions of sinogram data.

In (KOSTLER et al., 2006), it is proposed a variational interpolation approach that consists on minimizing an energy function which involves the under-sampled sinogram g, the desired sinogram f, and a regularization term. Such regularization term often involves derivative operators to restrict the gray values behavior at neighbor pixels of the sinogram image. The authors demonstrated that the results obtained using distinct linear regularizers are superior to the obtained previously in (BERTRAM et al., 2004).

In (LI et al., 2012), each missing measure in the sinogram is considered as a composition of a group of sinusoid-like curves. The proposed method consists of using a fitting method

to find the S-curves that go through each unmeasured point in the sinogram. Thus, each S-curve is responsible for the intensity variation in a different direction at each point. On the other hand, using the tensor theory, it is possible to measure the largest intensity variation of the sinogram in the same point. Finally, to fill in each missing pixel, the least-squares method is used to figure out the interpolated S-curve whose direction is closest to the largest intensity variation calculated using the tensor theory.

In (KALKE; SILTANEN, 2014), the sinogram is interpolated by solving characteristics of sine waves in a limited region, the so-called warps. The strategy consists of calculating the essential features of the warps. From those values, weight factors are defined and the sinogram unknowns can be estimated by numerical computations.

4.1.2.2 *Image registration-based methods*

In (HEUSSER et al., 2012) and (HEUSSER et al., 2014), a degraded reconstruction f from a sinogram with missing data is registered[2] to a prior artifact-free image g from a data set. Then, g is forwarded projected[3] to inpaint the missing data at the initial sinogram in a smooth way.

4.1.2.3 *Dictionary Learning-based methods*

In (LI et al., 2014), the missing sinogram data is inpainted using the Dictionary Learning method. The basic idea of such method is to build an over-complete dictionary of prototype signal-atoms. Thus, any image signal may be represented as a sparse linear combination of those atoms (AHARON; ELAD; BRUCKSTEIN, 2006). Li *et al.* used overlapping sinogram patches from a simulated phantom image to train a dictionary. Therefore, the sparse vector which best matches the corrupted sinogram in the space of signal-atoms is calculated. Finally, the reverse transformation to the original domain leads to an inpainted sinogram data.

4.1.2.4 *Artificial Neural Network (ANN)-based methods*

In (LEEA; LEEA; CHOA, 2017), it is proposed an interpolation method using Convolutional Neural Network (CNN) which is one of the architectures of Artificial Neural Network (ANN) used in deep-learning strategies. The CNN is built using 20 pairs of convolution and activation layers successively. At the proposed architecture, the output and the input data have the same size. Thus, the CNN is trained to enhance the sinogram up-sampled obtained by a simple linear interpolation method.

[2] image registration refers to the alignment of multiple images according to the similarity of their features. To overlap images is common to apply rotation, scale and skew to find the best match between the data.

[3] for a detailed description about conversions between in CT domains, see Appendix A.

4.1.3 Considerations

Since all the previously mentioned methods introduce priors into the sinogram processing to compensate the use of low levels of X-ray radiation, they are all related to this thesis. However, owing to the physical constraints imposed by the inline scanning geometry[4], there is a subset of such methods that are more suited to be applied in industrial CT machines. Those methods must *(i)* generate new sinogram views to allow the acquisition of the fewest number of X-ray projections possible; and *(ii)* avoid iterative algorithms to accelerate the computation time. Table 1 shows whether (or not) such characteristics are present at each method discussed in this section.

Table 1 – List of representative methods proposed in the literature since 2002 which incorporates priors into a sinogram processing to compensate the use of low levels of X-ray radiation at the acquisition stage. For each method, a ticker shows whether the method generates new sinogram views and/or it includes iterative algorithms. The most suited methods for industrial CT machines are highlighted in gray.

Method	Does it generates new sinogram views?	Does it includes iterative algorithms?
(LU et al., 2002)	✗	✓
(BERTRAM et al., 2004)	✓	✓
(LI et al., 2004)	✗	✓
(RIVIERE, 2005)	✗	✓
(WANG et al., 2006)	✗	✓
(KOSTLER et al., 2006)	✓	✓
(BORSDORF et al., 2008)	✗	✗
(MANDUCA et al., 2009)	✗	✗
(BERTRAM et al., 2009)	✓	✓
(BALDA; HORNEGGER; HEISMANN, 2012)	✗	✗
(LI et al., 2012)	✓	✓
(HEUSSER et al., 2012)	✓	✗
(LI et al., 2014)	✓	✓
(HEUSSER et al., 2014)	✓	✗
(KALKE; SILTANEN, 2014)	✓	✓
(KARIMI; WARD, 2016)	✗	✓
(LEEA; LEEA; CHOA, 2017)	✓	✗

[4] for a detailed description of the scanning constraints related to the inline geometry, see Figure 14.

4.2 Reconstruction

The methods which compute image reconstructions from sinogram data using priors can be categorized into *(i)* statistical-, *(ii)* Projections Onto Convex Sets (POCS)-, *(iii)* Discrete Tomography-, *(iv)* Dictionary Learning- or *(v)* Artificial Neural Network (ANN)-based methods. Each of those is described below:

(i) the statistical-based methods are those that incorporate into the reconstruction process the expected behavior of X-ray measures and/or attenuation coefficients observed in the reconstruction algorithm;

(ii) the POCS-based methods compute the final image reconstruction by iteratively projecting solution vectors onto few convex sets that holds different properties derived from distinct priors. Thus, the desired reconstruction is placed in the intersection among all convex sets;

(iii) the Discrete Tomography-based methods assume, as a prior, that only a few possible attenuation coefficients may occur in the scanned object;

(iv) the Dictionary Learning-based methods limit the possible solutions to those that are possible to be represented by atomic signals from a dictionary previously trained using a set of images;

(v) the ANN-based methods intend to create a mathematical model of a function which directly maps the data in the projection domain into the reconstruction domain.

In the following subsections, some of the most relevant techniques developed along the latest years to incorporate priors into the CT image reconstruction are described. In the end, considerations about the most suitable reconstruction techniques for the inline scanning system described in this work are summarized in a final subsection.

4.2.1 Statistical-based methods

Starting in the 1970's, some works, *e.g.* (ROCKMORE; MACOVSKI, 1976; SHEPP; VARDI, 1982; LANGE; CARSON et al., 1984), assumed the observed X-ray measurements as sets of Poisson random variables and - unlike previously proposed reconstruction methods that ignored the stochastic nature of the data - applied joint probability density functions to model the X-ray measurements. Thus, the images were reconstructed according to the Maximum Likelihood (ML) estimation theory using the Expectation Maximization (EM) algorithm. In (GREEN, 1990), the same technique based on ML was modified to incorporate priors about smoothness concentration of isotopes in the radiation. Later, (ERDOGAN; FESSLER, 1999) used Ordered Subsets EM (OSEM) to achieve a faster convergence of the EM algorithm when computing image reconstructions using the ML estimation theory.

In (GEMAN; GEMAN, 1984; SAUER; BOUMAN, 1993), prior information about spatially correlation of adjacent attenuation coefficients at similar objects, *i.e.* the probability distribution of the pixel values in the reconstructed image, was modeled using Markov Random Fields (MRF). Therefore, such prior distribution is used to regularize the data-fidelity term of an objective function defined according to a Maximum A Posteriory (MAP) estimation. Later, Thibault *et al.* used Generalized Gaussian Markov Random Fields (GGMRF) (THIBAULT et al., 2007), and Chen *et al.* used non-local weights (CHEN et al., 2008; CHEN et al., 2009) to model priors.

In (CANDÈS; ROMBERG; TAO, 2006), the Total Variation (TV), *i.e.* the sum of all gradient magnitudes at specific neighbors, is used to regularize the data-fidelity term of an objective function defined according to a MAP estimation. The authors claim that the image artifacts tend to have a large TV norm. Thus, a regularization which avoids solutions associated with large TV norms tends to benefits solutions that maintain fidelity to the observed data.

In (ZHANG et al., 2014; QI et al., 2016; CHEN et al., 2016), it is proposed Non-Local Means (NLM)-based approaches to regularize the data-fidelity term of a MAP estimation. NLM (BUADES; COLL; MOREL, 2005a; BUADES; COLL; MOREL, 2005b) is a non-linear filter which replaces each pixel value by a weighted average of its neighbors according to the similarity between them. The regularization terms proposed in those works tend to benefit solutions where similar regions of the image are associated with the same intensity value.

Distinct statistical-based methods were developed and patented by the largest manufactures of tomographic devices: *(i)* Siemens developed the Image Reconstruction in Image Space (IRIS) (GHETTI; ORTENZIA; SERRELI, 2012), *(ii)* Philips developed the iDose^4 (ARAPAKIS et al., 2014), *(iii)* GE Healthcare developed the Adaptative Statistical Iterative Reconstruction (ASIR) (SINGH et al., 2011). Thus, modern CT scanners can operate with lower radiation doses.

In the 2010's, the term "model-based" emerged to designate a group of techniques strongly connected to the statistical-based methods designed by Siemens, Philips, and GE Healthcare to take place IRIS, iDose^4, and ASIR. Such model-based methods go beyond statistical-based methods in the sense that they also model the system optics, *i.e.* the scanning geometry, the path traversed by each X-ray, the size of each detector cell, and others (KATSURA et al., 2012). The model-based algorithms that integrates the top CT scanners are (LIU, 2014): *(i)* SAFIRE (Siemens), *(ii)* IMR (Philips), and *(iii)* Veo (GE Healthcare). Studies show a higher performance of model-based algorithms rather than previous statistical-based algorithms when operating with setups of lower radiation exposure (NEROLADAKI et al., 2013; SCHEFFEL et al., 2012).

4.2.2 Projections Onto Convex Sets (POCS)-based methods

In (OSKOUI; STARK, 1989), the priors applied at each of the four convex sets used were: *(i)* the ray sum at each radiation path must be the same previously measured in the scanned object; *(ii)* the divergence between the solution and a given reference image must not exceed a given threshold; *(iii)* limitation of maximum and minimum attenuation coefficients in the solution; *(iv)* delimitation of the effective reconstruction area in the image plane.

In (SIDKY; KAO; PAN, 2006; SIDKY; PAN, 2008), the Total Variation (TV) of partial solutions is minimized, using the gradient descend approach, between two sequential executions of POCS steps. The algorithm is referred as adaptative-steepest-descend-POCS (ASD-POCS). ASD-POCS iterates continously until converge, *i.e.* significant changes are not found in the output of two successive POCS steps. Later, Huang *et al.* in (HUANG et al., 2011) proposed a variation in ASD-POCS where the TV minimization stage is replaced by a Non-Local Means (NLM)-based filtering.

4.2.3 Discrete tomography-based methods

Such methods play a key role in this work due to the fact they have been shown promising reconstruction results from very few projection directions. In fact, the very limited number of available attenuation coefficients in the reconstructed images - especially fewer than three or four - strongly reduces the space of valid solutions and, as a consequence, reduces the need for projections.

In (FRESE; BOUMAN; SAUER, 1999), the proposed technique follows the Bayesian approach by deriving an objective function according to a Maximum A Posteriory (MAP) estimation [5]. However, in contrast to other works, a discrete Markov Random Fields (MRF) is used to model the prior distribution of discrete attenuation coefficients in reconstructed images. Furthermore, they introduced multi-scale algorithms to both reduce computation and improve convergence to the global minimum.

In (SCHÜLE et al., 2005), a relaxation and convex-concave regularization is proposed to optimize the objective functions derived from the application of the Bayesian approach. The innovation of the work of Schüle *et al.* relies on the application of binary constraints, into the relaxation and regularization, to the values of the attenuation coefficients in the image. Another type of relaxation for obtaining discrete solutions, this time based on linear programming, is proposed in (WEBER; SCHNORR; HORNEGGER, 2003).

In (BATENBURG, 2007), a novel algorithm is proposed for reconstructing binary images. Several reconstruction steps for solving two-projection problems are applied in sequence for each pair of projections individually. Those reconstruction steps use a network flow approach at which the ray-sum of each projection is seen as one node in a network,

[5] for a complete review on Statistical-based methods for CT reconstruction, see Section 4.2.1.

and the connection weights between each pair of nodes represents a pixel value in the final image solution.

In (BATENBURG; SIJBERS, 2011b), a novel iterative algorithm for discrete tomography is proposed: the Discrete Algebraic Reconstruction Technique (DART). DART performs sucessive executions of conventional ART update steps and discretization steps at which the prior related to the set of attenuation coefficients presented in the object is incorporated.

In (GOUILLART et al., 2013), a prior which assumes that neighboring pixels have a larger probability to take the same value is exploited to generate discrete reconstructions using Belief Propagation (BP) which can be seen as an extension of Markov Random Fields (MRF) or Bayesian networks (YEDIDIA; FREEMAN; WEISS, 2003).

4.2.4 Dictionary Learning-based methods

In (ETTER; JOVANOVIC; VETTERLI, 2011), the idea of incorporating dictionaries of signals into the reconstruction process emerged. Instead of minimizing the cost function $||\mathbf{p} - \mathbf{Af}||^2$ (for more details on Algebraic Reconstruction Techniques (ART), see Section 2.3.1.2), Etter, Jovanovic, and Vettereli proposed the minimization of $||\mathbf{p} - \mathbf{AD}\alpha||^2$; where $\mathbf{D}$ is a dictionary of atomic signals learned from a training set of images, and α is a vector of coefficients which weighs the atomic signals of $\mathbf{D}$ to represent $\mathbf{f}$. Such approach limits the structs that may occur in $\mathbf{f}$ to those which are possible to be represented by the atomic signals in $\mathbf{D}$. A similar approach was also discussed in (XU et al., 2012; XU et al., 2015; SOLTANI; ANDERSEN; HANSEN, 2015; SOLTANI; ANDERSEN; HANSEN, 2017).

In (LU; ZHAO; WANG, 2011), it was proposed the use of a pair of dictionaries: a first one, $\mathbf{D}_1$ is learned from low quality CT images; and a second one, $\mathbf{D}_2$ is learned from high quality CT images. A correspondence between the atoms in $\mathbf{D}_1$ and $\mathbf{D}_2$ is built in such way that $\mathbf{D}_1$ is initially used to find the best reconstruction representation α in a lower sample scenario; then, $\mathbf{D}_2$ is used to represent α using the atoms related to high-quality images.

4.2.5 Artificial Neural Network (ANN)-based methods

In (MA; FUKUHARA; TAKEDA, 2000), it is proposed a direct application of a conventional feed-forward Artificial Neural Network (ANN) whose input neurons are associated to pixels in the sinogram data, and the output neurons are related to the pixels of the image in reconstruction domain. Later, Cierniak applied in (CIERNIAK, 2009) a similar approach using a Hopfield-type neural network. Such approaches results lead to very large network sizes. Thus, real-world applications of methods like those had not be found (PELT; BATENBURG, 2013).

In (PELT; BATENBURG, 2013), the Neural Network Filtered Back Projection (NN-FBP) method is presented. NN-FBP creates a model which reconstructs each pixel in the reconstruction individually to avoid large network sizes. Furthermore, it is shown that NN-FBP is equivalent to a weighted sum of multiples FBP algorithms, each one with a different filter.

In (WÜRFL et al., 2016), the key idea is similar to the previously presented in (MA; FUKUHARA; TAKEDA, 2000), *i.e.* mapping the FBP algorithm into an ANN model. However, Würfel *et al.* make use of modern neural architectures which involves deep nets. Then, they obtained similar results using FBP and deep nets.

4.2.6 Considerations

Since all the above-mentioned methods incorporate priors into the reconstruction process, they are - at first sight - closely related to the research presented in this thesis. Although, the most required aspects of a reconstruction stage that composes a fast inline CT system are: *(i)* the ability of producing high quality reconstructions from a very limited number of projections to reduce the acquisition time which has mechanical limitations[6]; and *(ii)* do not include iterative algorithms to avoid excessive time consuming. Table 2 shows whether (or not) such characteristics are present at each method discussed in this section. As highlighted in Table 2, the method presented by Pelt and Batenburg in (PELT; BATENBURG, 2013) is the unique that meets both of the desired requirements. Thus, Janssens *et al.* applied such method in an inline CT inspection system published in (JANSSENS et al., 2016b). However, as shown in Figures 18 and 20, the FBP-based reconstructions present crossed white artifacts which are inherent to the truncated projections generated in the inline scanning geometry. To overcome this issue, Janssens *et al.* proposed the use of an X-ray detector which moves along a linear trajectory to follow the scanned object and therefore avoid truncated projections near the detector borders. In this thesis, we opted for employing a fixed scanning setup to make the overall system cheaper. Then, in our approach, any type of artifacts that may occur must be solved via software. This explains why we will avoid the use of the method proposed in (PELT; BATENBURG, 2013) along this research.

[6] to more details on the limitations of the acquisition times in the inline scanning geometry, see Figure 22.

Table 2 – List of the representative methods proposed in the literature since the 1970's which incorporates priors into the reconstruction stage to compensate the use of low radiation levels at the acquisition stage. For each method, a ticker shows whether the paper shows experimental results using less than 32 X-ray projections and/or it includes iterative algorithms. The most suited methods for industrial CT machines are highlighted in gray.

Method	Dos it exposes nice results using less than 32 X-ray projections?	Does it includes iterative algorithms?
(ROCKMORE; MACOVSKI, 1976)	✗	✓
(SHEPP; VARDI, 1982)	✗	✓
(LANGE; CARSON et al., 1984)	✗	✓
(GEMAN; GEMAN, 1984)	✗	✓
(OSKOUI; STARK, 1989)	✗	✓
(GREEN, 1990)	✗	✓
(SAUER; BOUMAN, 1993)	✗	✓
(ERDOGAN; FESSLER, 1999)	✗	✓
(FRESE; BOUMAN; SAUER, 1999)	✓	✓
(MA; FUKUHARA; TAKEDA, 2000)	✗	✓
(WEBER; SCHNORR; HORNEGGER, 2003)	✓	✓
(SCHÜLE et al., 2005)	✓	✓
(CANDÈS; ROMBERG; TAO, 2006)	✓	✓
(SIDKY; KAO; PAN, 2006)	✓	✓
(THIBAULT et al., 2007)	✗	✓
(BATENBURG, 2007)	✓	✓
(CHEN et al., 2008)	✗	✓
(CIERNIAK, 2009)	✗	✓
(CHEN et al., 2009)	✗	✓
(HUANG et al., 2011)	✓	✓
(LU; ZHAO; WANG, 2011)	✗	✓
(ETTER; JOVANOVIC; VETTERLI, 2011)	✗	✓
(XU et al., 2012)	✗	✓
(BATENBURG; SIJBERS, 2011b)	✓	✓
(GOUILLART et al., 2013)	✓	✓
(PELT; BATENBURG, 2013)	✓	✗
(ZHANG et al., 2014)	✗	✓
(SOLTANI; ANDERSEN; HANSEN, 2015)	✗	✓
(QI et al., 2016)	✓	✓
(CHEN et al., 2016)	✓	✓
(WÜRFL et al., 2016)	✗	✗
(SOLTANI; ANDERSEN; HANSEN, 2017)	✗	✓

4.3 Post-reconstruction

The techniques that incorporate priors into the processing of the reconstruction outputs can be categorized into *(i)* Weighted filtering-, *(ii)* Image registration-, *(iii)* Dictionary Learning-, or *(iv)* ANN-based methods. Each of those is presented below:

(i) the Weighted filtering-based methods apply weighted sums to similar parts of the same or distinct CT images to suppress artifacts and emphasize non-corrupted areas;

(ii) the image registration-based methods looks up to a set of normal-dose CT images acquired at conventional scans of similar objects to use those images for suppressing artifacts that occur in low-dose CT images;

(iii) the Dictionary Learning-based methods enhance the low-dose CT reconstructions by trying to represent the final reconstructions as a weighted sum of noise-free signals;

(iv) the ANN-based methods intend to create a mathematical model able to learn how to rearrange the pixel values in an artifact-full CT reconstruction to generate the pixel values distribution coherent to the expected structures in the scanned object.

In the following subsections, it is described some of the most relevant techniques developed along the latest years to incorporate priors into the post-reconstruction stage of the CT imaging workflow. In the end, considerations about the most suitable reconstruction techniques for the scanning system described in this work are summarized in a final subsection.

4.3.1 Weighted filtering-based methods

In (MA et al., 2011), the conventional Non-Local Means (NLM) technique is adapted to utilize redundancy information of previous of normal-dose scans to restore artifacts that occur in low-dose scans. In this proposed technique, the pixel values of the normal-dose CT image are weighted summed according to their similarity to the correspondent pixel values in the low-dose CT image to suppress the artifacts that emerged due the reduced used of radiation in the acquisition stage. Similar approaches were also proposed in (XU; MUELLER, 2011; HA; MUELLER, 2013).

4.3.2 Image registration-base methods

In (YU et al., 2009), the Previous Scan Regularized Reconstruction (PSRR) method is proposed to improve the quality of ultra-low-dose CT image by utilizing previously normal dose CT scan of the same patient. PSRR aims at recognizing substantially changed parts in ultra-low-dose scans, and replace them with other parts from the normal dose scan which share the same corresponding features.

In (XU; HA; MUELLER, 2013), the input low-dose image is used to query global features in a database built using normal dose CT. Then, a method based on Non-Local Means (NLM) is used to enhance the low-dose image from the data acquired from the normal dose CT images. A similar approach was also discussed in (HA; MUELLER, 2015).

4.3.3 Dictionary Learning-based methods

In (CHEN et al., 2013), it is presented an approach where the small image patches of a low-dose CT reconstruction is represented using a dictionary of atomic signals learned from a training set of normal dose CT reconstruction. Similar approach was also discussed later in (CHEN et al., 2014b).

In (CHEN et al., 2014a), different dictionaries were used to enhance different sub-bands of the image frequency spectrum. Such band decomposition is obtained using the Wavelet Transform. After the enhancement of each sub-band, the Inverse Wavelet Transform is used to map the data into the spatial domain.

4.3.4 Neural Network-based methods

In (CHEN et al., 2017a), it is proposed the training of a deep architecture of an Artificial Neural Network (ANN) - the auto-encoders - to learn the end-to-end mapping from a low-dose CT image to its respective normal dose CT image. Similar approach that employs Convolutional Neural Networks was also discussed in In (CHEN et al., 2017b).

4.3.5 Considerations

Since all the above-mentioned methods incorporate priors into the post-reconstruction CT imaging process, they are related to the research presented in this thesis. However, the methods must present two basic characteristics to fit in the inline CT imaging machine which is the focus of this thesis. Such characteristics are: *(i)* be able to enhance reconstructions obtained from a low number of X-ray projections to accelerate the acquisition stage; and *(ii)* does not include iterative algorithms to avoid excessive computing time. Table 3 shows whether (or not) such characteristics are present at each method discussed in this section.

Table 3 – List of the representative methods proposed in the literature which incorporates priors into the post-reconstruction stage to compensate the use of low radiation levels at the acquisition stage. For each method, a ticker shows whether the paper shows experimental results using less than 32 X-ray projections and/or it includes iterative algorithms. The most suited method for industrial CT machines is highlighted in gray.

Method	Does it report enhancement results of CT images acquired using less than 32 X-ray projections?	Does it includes iterative algorithms?
(YU et al., 2009)	✓	✗
(MA et al., 2011)	✗	✗
(HA; MUELLER, 2013)	✗	✗
(CHEN et al., 2013)	✗	✓
(CHEN et al., 2014a)	✗	✓
(XU; HA; MUELLER, 2013)	✗	✗
(HA; MUELLER, 2015)	✗	✗
(CHEN et al., 2017a)	✗	✗
(CHEN et al., 2017b)	✗	✗

5 PROPOSED METHODS

This chapter presents software-based solutions able to improve the overall CT system throughput based on the idea presented in the Chapter 3: to reduce the number of X-ray projections acquired to the smallest possible, to reduce the scanning time, by exploiting distinct types of prior knowledge about the scanned object. Thus, two approaches are discussed. The first one is placed in the standard CT workflow. In fact, two distinct techniques are proposed for the *reconstruction*, and *post-processing/segmentation* stages. The second approach suggests that, for quality assessment purposes, the *reconstruction* stage may be bypassed.

5.1 Conventional CT workflow

The techniques presented in this section are anchored in the conventional CT workflow. In Section 5.1.1, prior knowledge about material's composition and object shape are injected into the *reconstruction* stage. In Section 5.1.2, prior knowledge automatically acquired from a trained set of images is included into the *post-processing/segmentation* stage. Figure 25 highlights the stages of the CT workflow at which the methods proposed are situated.

Figure 25 – Conventional CT workflow with the *reconstruction* and segmentation stages highlighted to indicate where the methods proposed in this section are positioned into the complete flow.

5.1.1 Using prior knowledge about material's composition and object shape

Unlike continuous reconstruction techniques such as FBP and SIRT, Discrete Tomography can operate with a reduced number of projections because only a few possible attenuation coefficients may occur within the object. If such coefficients are previously known, DART[1] may be used.

In fact, DART incorporates specific prior knowledge related to the density of the scanned materials, and it has shown that it can reconstruct high-quality images, reducing the occurrence of smearing artifacts, even from a limited amount of data. DART has successfully been applied in conventional CT (DABRAVOLSKI; BATENBURG; SIJBERS, 2014)

[1] See Section 2.3.2 for a detailed description of DART.

and in electron and X-ray diffraction tomography (BATENBURG; SIJBERS, 2009). However, as illustrated in the scheme presented in Figure 11, there are several ART iterations within a single DART iteration. As a result, DART is a computationally expensive method and the elapsed time in the reconstruction process may impact the throughput of the proposed inline X-ray CT system. Thus, an improvement on DART which can reduce the number of reconstruction iterations until the convergence of the algorithm is also proposed in this work.

In ART, reducing the number of pixels to be reconstructed (as described in Equation 2.14) is an interesting approach to reduce the number of unknown pixels while keeping the number of equations fixed in the linear system presented in Equation 2.13. As a result, the final reconstruction is improved as a large number of unknowns are replaced by *a priori* known values. Thus, if the outer object shape is known in advance, it is possible to remove the pixels related to the background from the reconstruction domain. This way, the limited number of projections available in the proposed setup is used to compute only a subset of the whole set of unknown pixels. To determine an object contour, optical sensor systems can be incorporated into the proposed inline scanning geometry.

Figure 26 shows an overview of the proposed method at which the reconstruction domain is limited to the object's contour by incorporating an Expected Object Domain (EOD) in the reconstruction process. To create an EOD representation which distinguishes the object pixels from the background, a simple technique as thresholding is usually enough.

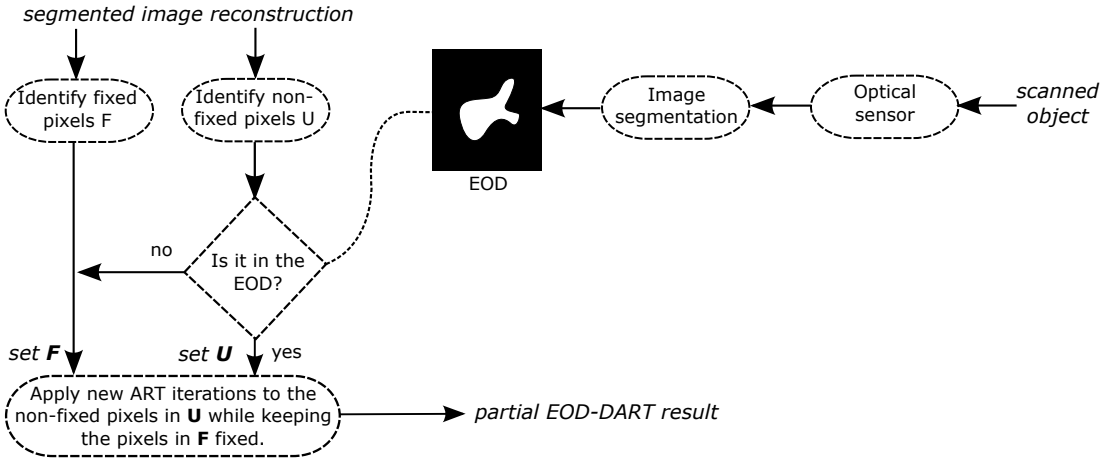

Figure 26 – Flow chart proposed for EOD-DART in relation to DART flow chart: the pixels outer the object's domain are removed from the set of non-fixed pixels U at each DART iteration.

The proposed EOD can be incorporated into the process of DART just after identifying the **set of fixed pixels F** and the **set of non-fixed pixels U** from the segmented reconstruction. The pixels selected to be updated (i.e., which composes the set **of non-fixed pixels U**) are evaluated in respect to their position in the EOD matrix: the pixels

which lie outside the EOD borders can be transposed to the set of **fixed pixels F**. As a result, only pixels which lie inside the EOD would be candidates for an update. After applying new ART iterations to the pixels within the **set of non-fixed pixels U**, a partial EOD-DART result would be obtained. If the stop criterion is met, the execution ends. Otherwise, a new iteration is computed as illustrated in Figure 11.

Finally, it is expected that DART provide high-quality reconstructions by using fewer X-ray projections, *i.e.*, reducing the system's scanning time. Furthermore, it is also expected that the number of DART iterations necessary to the solution convergence would be reduced by the use of the EOD, *i.e.* reducing the system's reconstruction time.

5.1.2 Extracting prior knowledge from a training set of images

An idea to speed up the throughput in the proposed inline X-ray CT system may consist of improvements on segmentation/post-processing stage of CT workflow instead of making an effort to improve the reconstruction stage. Such segmentation may be specifically designed for each type of object, and it would recover its natural aspects that were lost due to the availability of only a limited number of projection data in the inline scanning setup. Thus, a novel segmentation module based on Machine Learning (ML) techniques is proposed in this thesis.

If Machine Learning (ML) techniques are used, prior knowledge about the scanned object can be acquired automatically from a training set at which the data present similar characteristics to that one that is being scanned. Recently, (SOLTANI; ANDERSEN; HANSEN, 2017) proposed the use of a set of images to train a visual dictionary which is then used as a regularization term in an algebraic reconstruction method. Once based on the solution of an optimization problem, such method is computationally expensive and should be avoided in applications where the processing time is critical. Alternatively, (JANSSENS et al., 2016a) proposed a successful Neural Network-based Hilbert transform Filtered Backprojection (NN-hFBP) trained with samples of the scanned object to perform fast tomography in an inline setup design where the detector moves with the object to avoid the acquisition of truncated projections. In contrast, the method proposed in this section operates with a fixed X-ray detector to reduce system's costs (*i.e.*, acquiring truncated projections[2]).

The proposed method consists of two steps: a training stage and an evaluation stage. Each of those is described in the next two subsections.

5.1.2.1 *Training stage*

The proposed architecture for the training stage is shown in Figure 27. This setup was designed to incorporate knowledge from the relationship between the segmented high-

[2] Section 3.1 describes the existence of truncated projections in the inline CT setup.

quality X-ray CT images and the low-quality X-ray CT images produced in a fast inline setup. For this purpose, a training set is created by scanning objects $O = \{o_1, o_2, \cdots, o_n\}$ to form two groups: *(i)* high quality CT images $H = \{h_1, h_2, \cdots, h_n\}$ generated using, for example, a conventional cone beam acquisition; and *(ii)* low quality CT images $L = \{l_1, l_2, \cdots, l_n\}$ generated from projection data acquired in a fast inline setup. Then, the operation of each module in Figure 27 is described as following:

- **feature extraction:** each pixel of every image k in the set L, *i.e.*, $l_k(u, v)$, $1 \leq k \leq n$ is linearly transformed into a feature vector $x^{(i)} \in \mathbb{R}^m$, where (i) denotes an instance in the training set.
- **conventional segmentation:** a label $y^{(i)}$ is assigned to the feature vector $x^{(i)}$ according to $S(h_k(u, v))$, where $S(\cdot)$ is a segmentation technique, such as Otsu, to compose the training instance $(x^{(i)}, y^{(i)})$.
- **classifier training:** a Machine Learning technique is used to train a decision model λ able to estimate a label $y^{(i)}$ for a feature vector $x^{(i)}$ relative to an image pixel of a new input. Classification techniques such as Multilayer Perceptron (MLP) (RUMELHART; HINTON; WILLIAMS, 1985) or Random Forest (RF) (HO, 1998) would be used to implement this module.

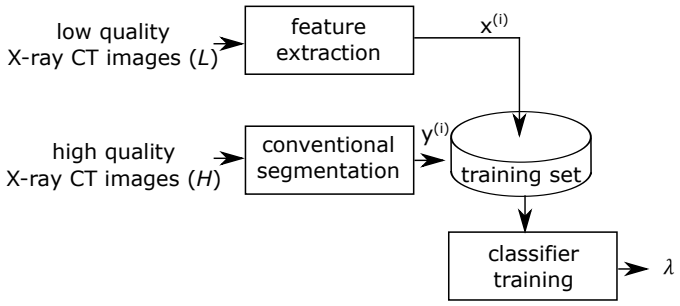

Figure 27 – The proposed architecture for the system's training stage: a training set stores the relationship between the segmented high-quality X-ray CT images and the low-quality X-ray CT images produced in the inline setup. Then, a classifier is trained to generate the decision model λ able to segment pixels of new input.

The flowchart of the *feature extraction* module, which generates $x^{(i)}$, is shown in Figure 28. The operation of the sub-modules for each image pixel is described as follows:

- **positions evaluation:** computation of the distance ρ to the object's center of mass $\bar{l_k}$, as illustrated in Figure 29.
- **patches extraction:** the gray values within a $\omega \times \omega$ neighborhood are extracted to compose the image patch γ.

- **vectors composition:** the gray values of the patch γ and the distance ρ are disposed in a single feature vector $x^{(i)}$. Thus, the length of the feature vector is $\omega \cdot \omega + 1$ and the number of vectors created is $p \cdot q \cdot n$, at which $p \times q$ is the image dimension and n is the amount of images in L.

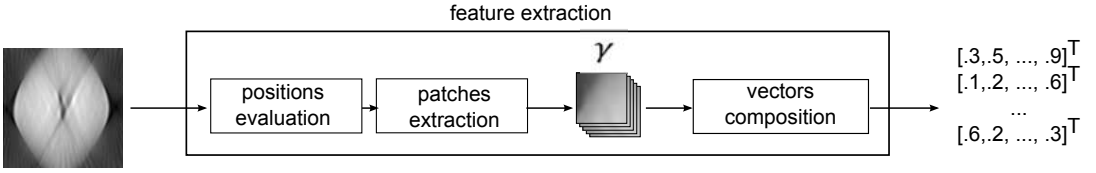

Figure 28 – The proposed architecture for composing the feature vector for each pixel of the input image: first, the distance between each pixel position and the object's center of mass is computed at the *positions evaluation* module. Then, every image patch γ presented in the image is captured at the *patches extraction* module. Finally, the gray values of each image patch and its relative position to the object's center of mass are distributed in a single feature vector at the *vectors composition* module.

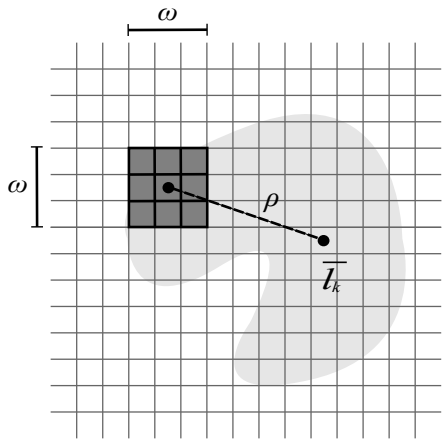

Figure 29 – Schema of the *feature extraction* module which computes the distance ρ from an actual pixel position to the center of mass $\bar{l}_k$ of the image and the gray values in a $\omega \times \omega$ image grid.

5.1.2.2 *Evaluation stage*

The proposed architecture for the evaluation stage is shown in Figure 30. First, each pixel from a low-quality X-ray CT image is transformed into feature vector $x^{(i)}$ at the *feature extraction* module, as described in Figure 28. Then, at the *pixel classification* module, the decision model λ is used to classify each vector $x^{(i)}$ into one of the possible labels $\{y_1, y_2, \cdots, y_z\}$ which are previously defined in the segmentation of the images in H. Finally, the output associated to the classification of distinct pixels are arranged into an image grid at the *image composition* module to generate the final segmented image.

To accelerate the evaluation stage, the independence of the *feature extraction* and *pixels classification* modules concerning the pixels position in the image may be exploited, *i.e.*, multiple instances of both modules can be used simultaneously to process distinct pixels of the image.

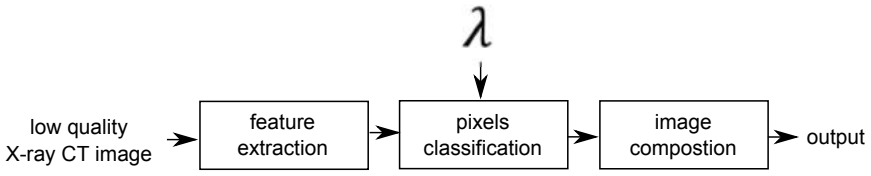

Figure 30 – The proposed architecture for the evaluation stage: first, each pixel in the input image is transformed into a feature vector $x^{(i)}$ at the *feature extraction* module. Then, the decision module λ is used to assign a label y to the input vectors at the *pixels classification* module. Finally, the output of each classification is arranged into a final image grid at the *image composition* module.

As a result, it is expected that such segmentation may recover the natural aspects of the objects that were lost due to the limited projection data available in the inline scanning setup.

5.2 Altered CT workflow

The approaches discussed so far in this work, *i.e.* focused on the standard workflow, may not be the most suited for an industrial environment. This is because the high-throughput desired will not allow a human to perform a real-time analysis of the reconstructed images. Therefore, an algorithm would be developed to automate such stage of analysis.

If the pre-processing, reconstruction, and segmentation stages of the conventional CT workflow are bypassed, as illustrated in Figure 31, the reconstruction time is saved. Thus, the analysis stage may be adapted to receive the input directly from the acquisition stage and provide a decision based on the object's quality.

This proposed method is based on the fact that all the information of the reconstructed image is already present in the sinogram[3]. For instance, Figure 32 illustrates how the

[3] for a detailed description of sinograms, see Appendix B.

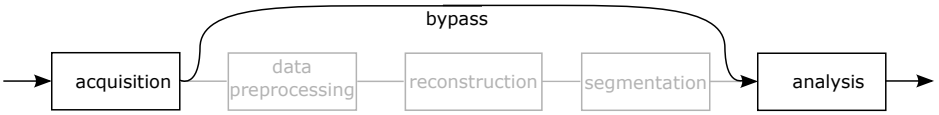

Figure 31 – Workflow of the proposed method in which the pre-processing, reconstruction, and segmentation stages are bypassed.

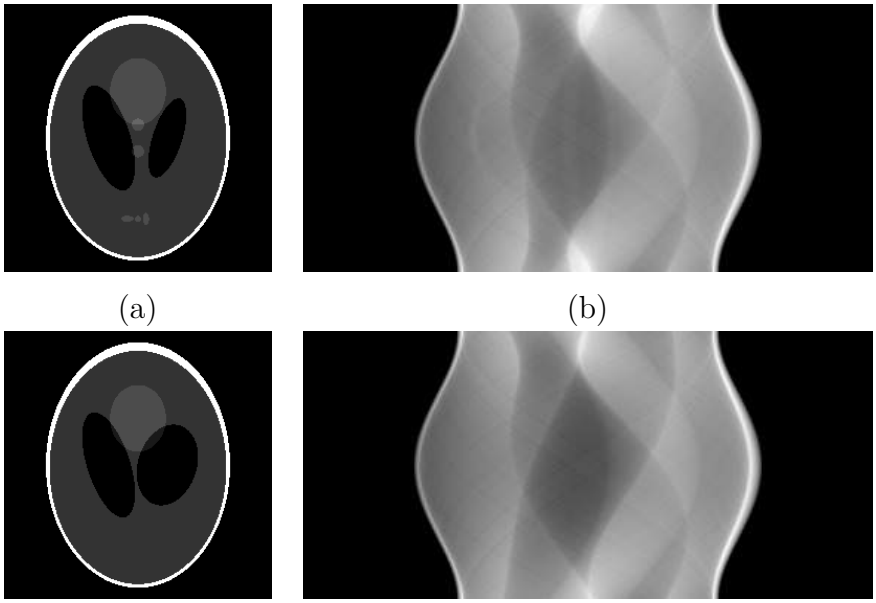

Figure 32 – Two similar objects with distinct internal structures leads to soft differences in the sinograms.

internal structures of two distinct objects reflects on soft differences in the sinograms.

In the sinogram, the data is organized in a way that does not help human understanding, although a computer vision algorithm can learn such organization. Furthermore, if only a small amount of data would be enough for the algorithm classify the object, the number of X-ray projections acquired in the object scanning should be reduced which will also lead to an inferior scanning time.

To design a novel analysis module able to process the CT raw data as input and understand it, we apply the Bag-of-Features (BoF) technique which was successfully used in image classification, categorization, and retrieval tasks (BOSCH; MUñOZ; MARTí, 2007; CSURKA et al., 2004). In BoF, low-level features are extracted from a training set of images to compose a vocabulary of visual words. Thus a novel image can be represented by a vector that represents the number of occurrences of each visual feature in the image. More specifically, a system based on the BoF technique contains three main stages: vocabulary construction, attribution of terms, and vector generation. In the present thesis, the design of each of those stages is proposed as follows:

- **vocabulary construction:** Scale-Invariant Feature Transform (SIFT) is used to extract low-level features from sinograms in a training set, as shown in Figure 33 (a); then, all the features are combined in a single vector space, as illustrated in Figure 33 (b); finally, the K-means algorithm is used to find K clusters in the feature space and visual words $\{c_1, c_2, \cdots, c_k\}$ is assigned to the centroid of each cluster, as presented in Figure 33 (c);

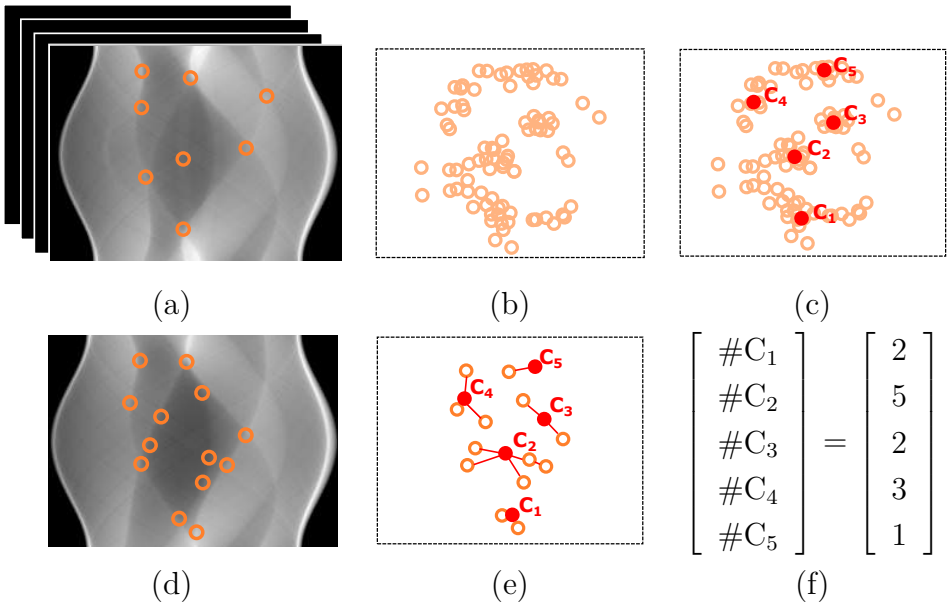

Figure 33 – Intermediate steps of the BoF solution proposed in this thesis: **vocabulary construction** in (a), (b), and (c), **attribution of terms** in (d) and (e), and **vector generation** in (f).

- **attribution of terms:** for a new sinogram, SIFT features are extracted, as illustrated in Figure 33 (d); then, each feature is assigned to the nearest cluster (or visual world), as shown in Figure 33 (e);
- **vector generation:** each dimension of the final feature vector is composed of the frequency of occurrence of each visual world in the image, as shown in Figure 33 (f).

Then, any Machine Learning technique, such as Multilayer Perceptron (MLP) (RUMELHART; HINTON; WILLIAMS, 1985) or Random Forest (RF) (HO, 1998), can be used to train a decision model λ to assign a correct label, *e.g. high-quality* and *low-quality*, to each input sinogram.

6 EXPERIMENTAL RESULTS

This chapter presents the experimental results obtained in the evaluation of the methods proposed in Chapter 5. The datasets and the experimental environment used are the same of the exposed in Section 3.2. Thus, the reconstruction quality and processing time obtained in the experiments of this chapter are compared with those presented in Section 3.2.2 that, for applying standard techniques such as Filtered Back Projection (FBP) and Simultaneous Iterative Reconstruction Technique (SIRT), is our baseline.

The content of this chapter is organized following the same structure of the Chapter 5: the first section presents the experimental results of the techniques which are anchored in the conventional CT workflow; then, the second section shows the experimental results of the shortened CT workflow.

6.1 Conventional CT workflow

As discussed in Chapter 5, the goal of the methods based on conventional CT workflow is to reduce the number of projections required in the system's acquisition stage to improve the throughput of the inline CT [1]. Thus, we are looking for the best trade-off between reconstruction quality and scanning time.

In the following experiments, two performance measures are used: *(i)* the rate of pixels with correct attenuation coefficients in relation to the phantom images segmented by the multi-level Otsu (LIAO et al., 2001) to measure the reconstruction accuracy; and *(ii)* the number of X-ray projections required in the reconstruction process to of the system's scanning time[2].

6.1.1 Using prior knowledge about material's composition and object shape

To evaluate the method proposed in Section 5.1.1, the accuracy of DART reconstructions were compared to the solutions generated by FBP and SIRT in scenarios at which a small number of X-ray projections is acquired to reduce the scanning time of the inline setup. To compare non-discrete solutions (created by FBP and SIRT) with discrete solutions (created by DART), the output of FBP and SIRT were segmented using the multi-level Otsu (LIAO et al., 2001) which lead to the Segmented FBP (S-FBP) and the Segmented SIRT (S-SIRT). Figure 34 shows the box plots of the reconstruction accu-

[1] Section 3.2.2 showed that the scanning time predominates over the reconstruction time, when FBP and SIRT are applied, to compose the overall processing time.

[2] a closer relation between the number of X-ray projections acquired and the scanning time in the inline system used in this work was explored in Figure 22.

racy provided by (a) S-FBP, (b) S-SIRT, and (c) DART in the Jonagold apple dataset. Figure 35 shows the same for the Bell pepper dataset.

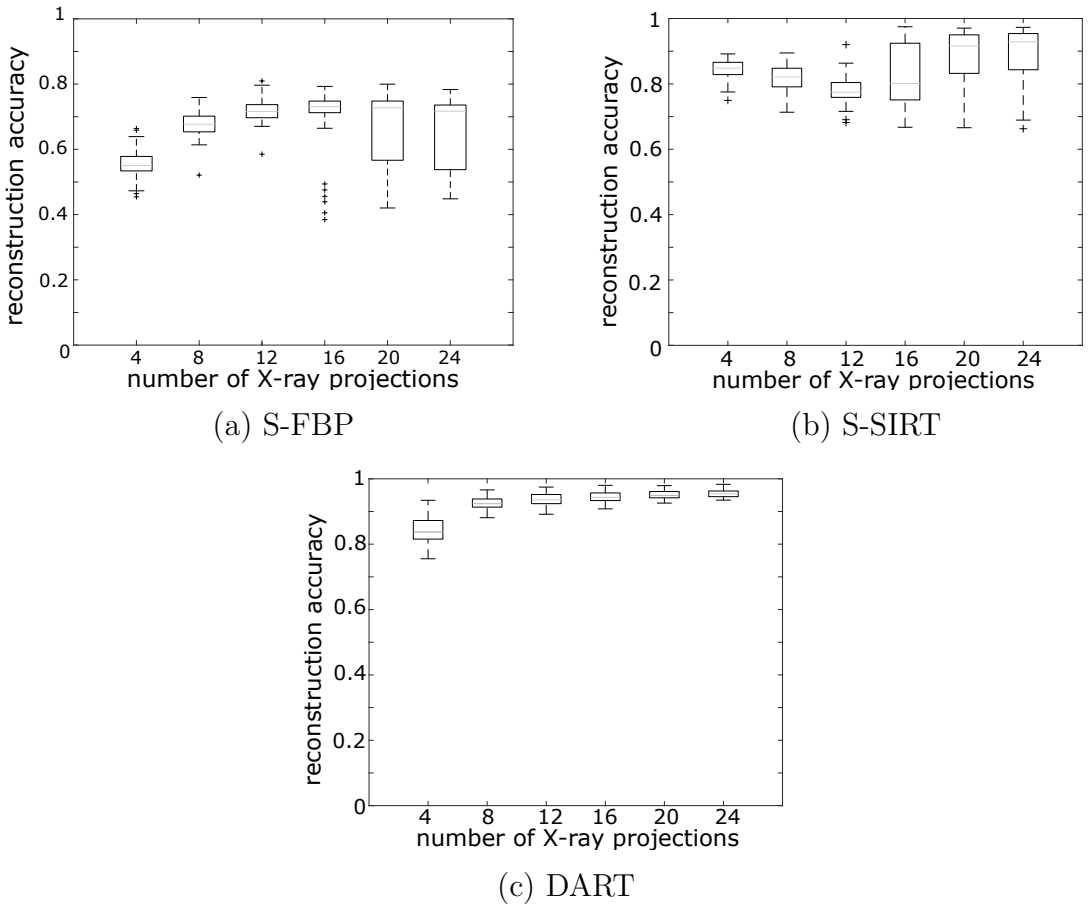

(a) S-FBP

(b) S-SIRT

(c) DART

Figure 34 – Box plots of the reconstruction accuracy provided by (a) S-FBP, (b) S-SIRT, and (c) DART in simulations of the inline scanning setup using the Jonagold apple dataset.

The results shown in Figures 34 and 35 show that by applying DART it is possible to achieve high quality image reconstructions from a small number of X-ray projections. This leads to a fast scanning stage, as desired. For illustration purposes, Figures 36 and 37 show examples of the obtained reconstructions and its respective ground truths.

However, the use of a new reconstruction stage affects the overall processing time. In fact, using 16 X-ray projections, to reconstruct 256×256 images, the reconstruction time is about $30s$ if DART is applied against $0.26s$ if SIRT is applied. To mitigate such excessive time consumption, which was already expected[3], Section 5.1.1 proposed the addition of an Expected Object Domain (EOD) into the workflow. Figure 38 shows the growth of accuracy as many DART iterations are applied with and without EOD. The results show that, using EOD-DART, it is possible to achieve reconstruction convergence

[3] this justification can be seen at Section 5.1.1.

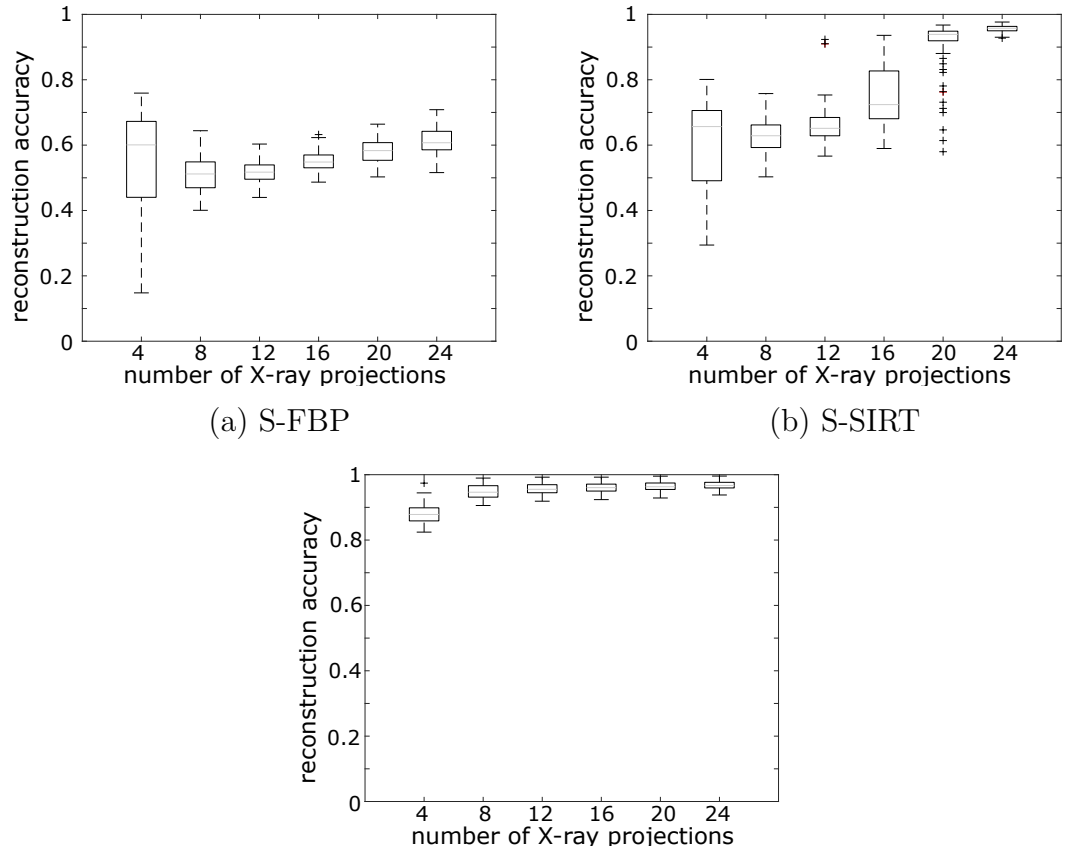

(a) S-FBP

(b) S-SIRT

(c) DART

Figure 35 – Box plots of the reconstruction accuracy provided by (a) S-FBP, (b) S-SIRT, and (c) DART in simulations of the inline scanning setup using the Bell pepper dataset.

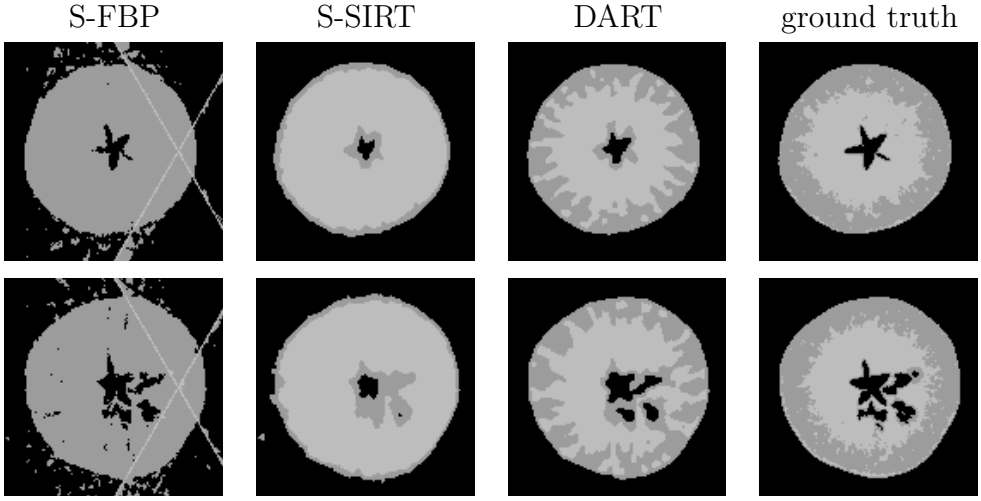

Figure 36 – Examples of reconstructed images of apples using 15 X-ray projections in the proposed inline X-ray CT system using a conveyor belt that allows object rotation.

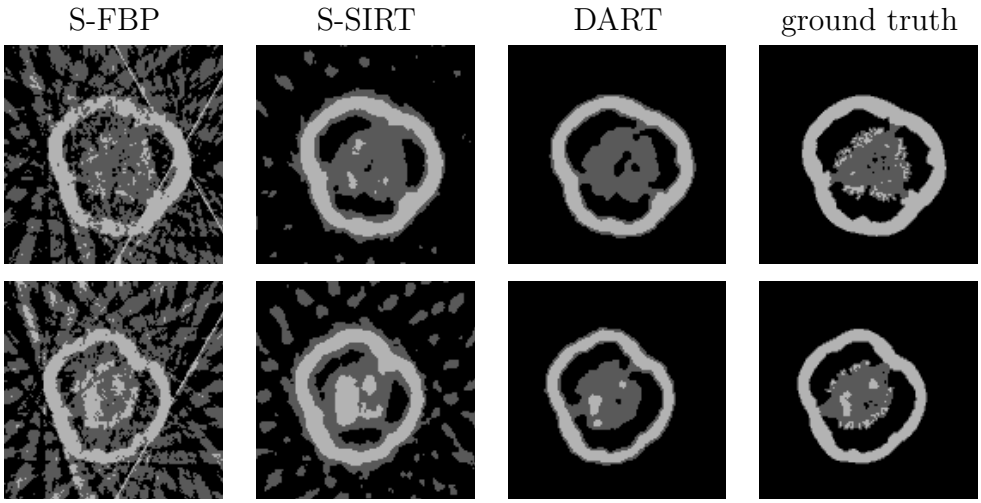

Figure 37 – Examples of reconstructed images of peppers using 15 X-ray projections in the proposed inline X-ray CT system using a conveyor belt that allows object rotation.

using a reduced number of iterations, *i.e.* faster. Unfortunately, even EOD-DART is not fast enough to provide the throughput required in industrial CT systems.

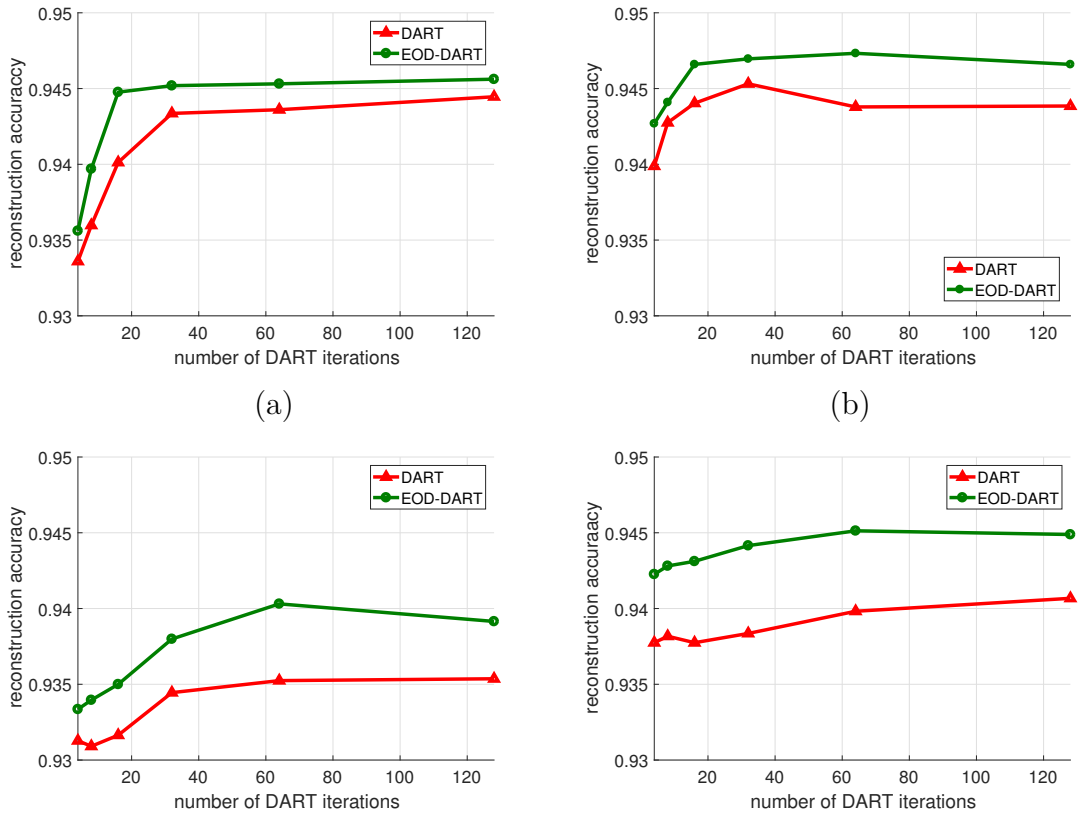

Figure 38 – Growth of reconstruction accuracy as many as DART iterations are applied with and without EOD.

6.1.2 Extracting prior knowledge from a training set of images

To evaluate the method proposed in Section 5.1.2, two scenarios were created at which the constraints are: *(i)* a small number of projections to reduce the scanning time; and *(ii)* a reduced number of SIRT iterations to check if the reconstruction time can also be reduced.

6.1.2.1 *Reduced number of X-ray projections*

Image reconstructions were simulated in the inline scanning setup using 4, 8, 12, 16, 20 and 24 X-rays projections. Figure 39 shows the box plot of the segmentation accuracy for (a) conventional Otsu and (b) the proposed method in the Jonagold apple dataset. Figure 40 shows the same in the Bell pepper dataset.

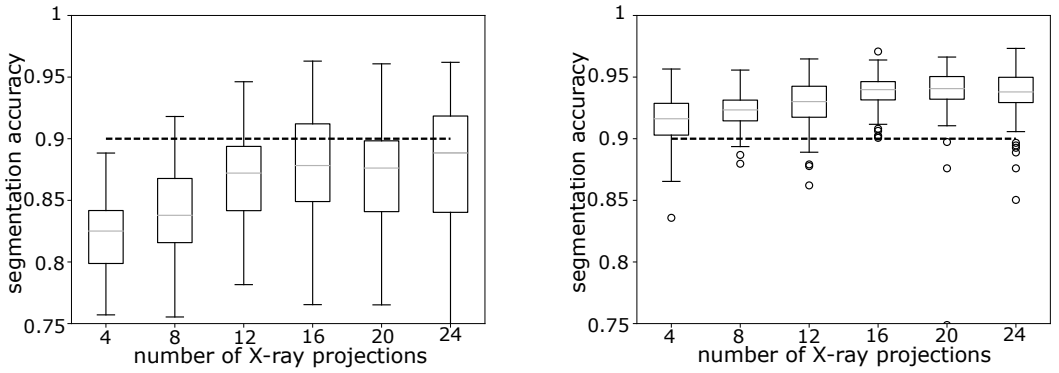

(a) Otsu (b) proposed method

Figure 39 – Box plot of segmentation accuracy for (a) conventional Otsu and (b) the proposed method using the dataset of apples. The dotted line represents an accuracy threshold of 90%.

Assuming that 90% of reconstruction accuracy is enough for the quality assessment, the proposed method ensures this quality level for all images in both datasets when at least 16 X-ray projections are used. In the bell pepper dataset, 90% of accuracy was only obtained with 24 X-ray projections using conventional methods. In the apple dataset, such quality levels could not be achieved using standard methods with less than 24 X-ray projections. These results combined with the measured times shown in Figure 22 demonstrate that the proposed approach ensures an accuracy of at least 90% for a scanning of 15 to 29 seconds depending on the conveyor belt's acceleration/deceleration. Using conventional technique, the scanning elapsed time should be 19 to 37 seconds or more. Thus, a reduction of at least 21% in the scanning time can be achieved.

For illustration purposes, examples of the obtained reconstructions and its corresponding ground truth are shown in Figures 41 and 42.

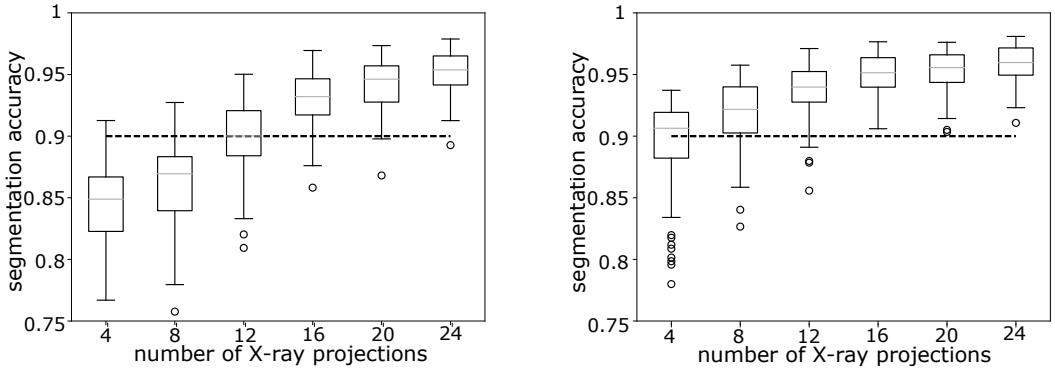

(a) Otsu (b) proposed method

Figure 40 – Box plot of the segmentation accuracy for (a) conventional Otsu and the (b) proposed method using the dataset of bell peppers. The dotted line represents an accuracy threshold of 90%.

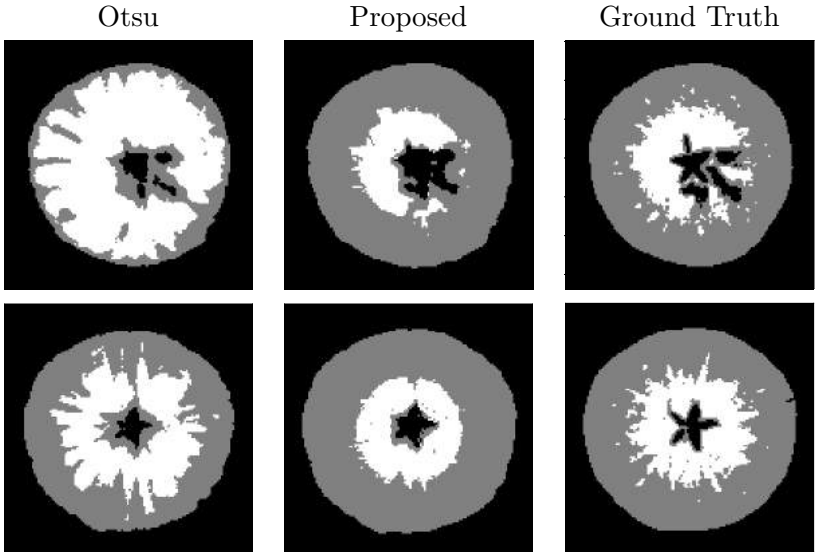

Figure 41 – Examples of reconstruction results of apples using 16 X-ray projections and 128 SIRT iterations.

6.1.2.2 *Reduced number of SIRT iterations*

Reconstructions were simulated using 16 projections and SIRT iterations varying from 8 to 128. Figures 43 and 44 show the box plot of the segmentation accuracy for (a) conventional Otsu and (b) the proposed method in the Jonagold apple and Bell pepper dataset, respectively.

The results show that 32 iterations are enough for both datasets to ensure a reconstruction accuracy above 90% if the proposed method is used. The reader should notice that - even using 128 iterations - the conventional method did not ensure an accuracy index of 90% in both datasets. Based on these experiments and in the time measures pre-

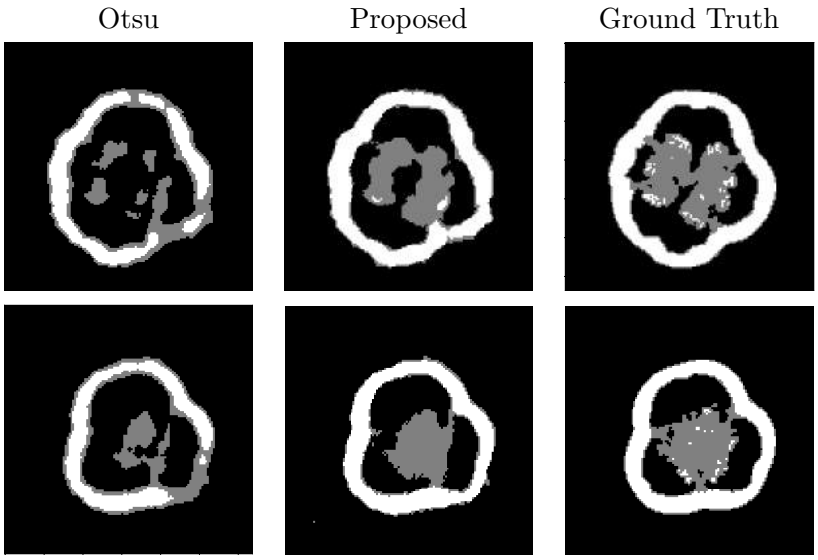

Figure 42 – Examples of reconstruction results of bell peppers using 16 X-ray projections and 128 SIRT iterations.

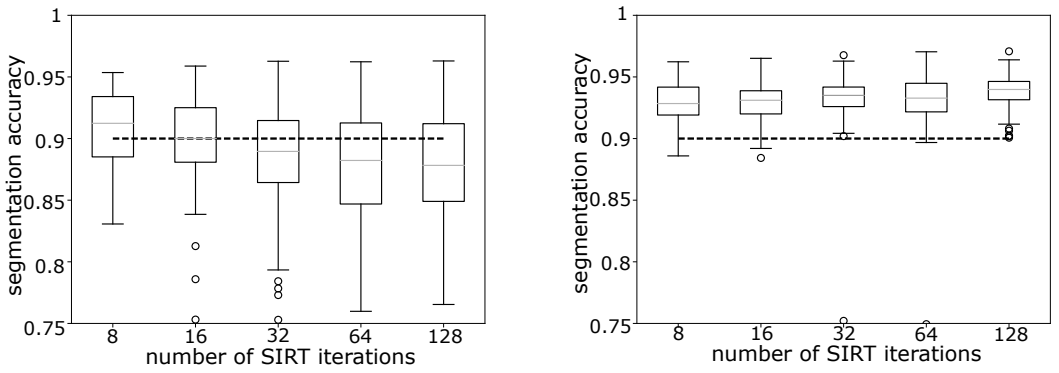

(a) Otsu (b) proposed method

Figure 43 – Box plot of segmentation accuracy for Otsu (a) and (b) the proposed method using the dataset of Jonagold apples. The dotted line represents an accuracy threshold of 90%.

sented in Figures 23 and 24, we conclude that, if the proposed method is used, SIRT can achieve reconstruction times comparable to FBP while keeping a sufficient image accuracy. For instance, to generate images of high resolution (1024×1024) with reconstruction accuracy over 90%, SIRT may takes $1.9003s$ (using 32 projections) which is very close to the $1.8664s$ taken by FBP (using 128 projections). This is an important result because, in the state-of-the-art, FBP is always preferable than SIRT if time resolution is a constraint.

For illustration purposes, examples of the obtained reconstructions and its respective ground truth are shown in Figures 45 and 46.

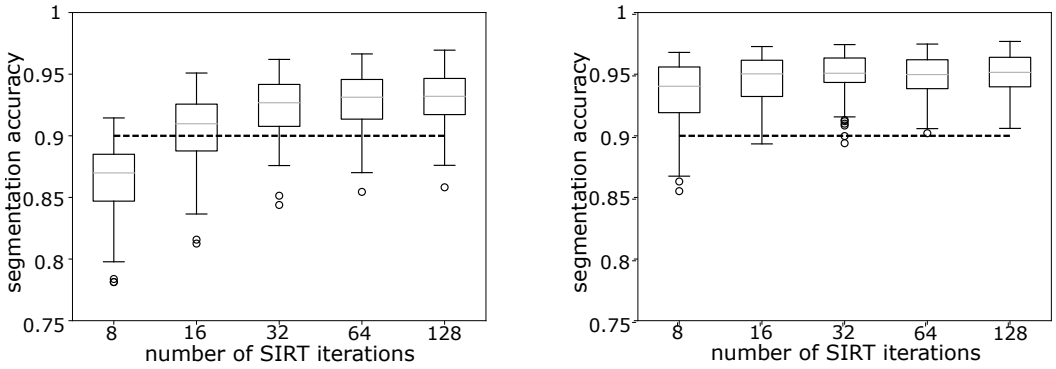

(a) Otsu (b) proposed method

Figure 44 – Box plot of segmentation accuracy for (a) Otsu and (b) the proposed method using the dataset of Bell peppers. The dotted line represents an accuracy threshold of 90%.

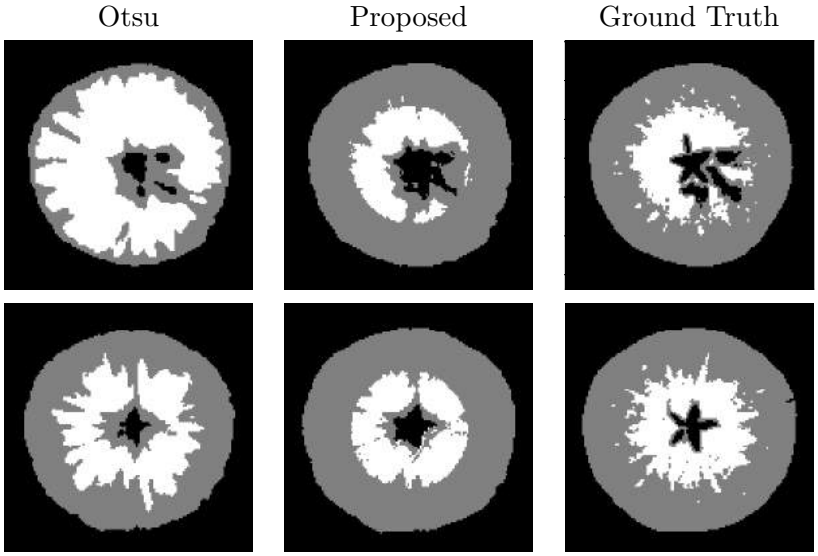

Figure 45 – Examples of reconstruction results of apples using 16 X-ray projections and 32 SIRT iterations.

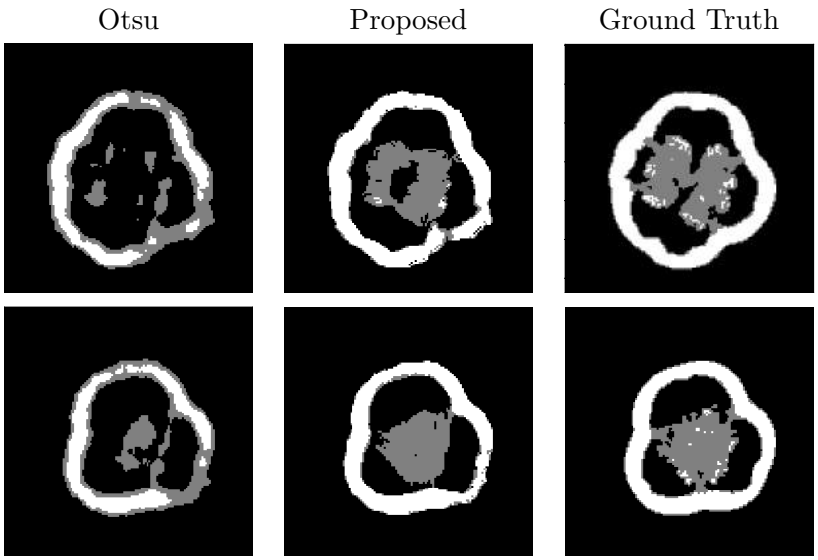

Figure 46 – Examples of reconstruction results of bell peppers using 16 X-ray projections and 32 SIRT iterations.

6.2 Altered CT workflow

As discussed in Chapter 5, the goal of the method based on the altered CT workflow is to reduce the processing time by eliminating the reconstruction stage from the workflow. Moreover, since no reconstruction algorithm will be executed, a reduced number of X-ray projections can be enough to classify the input data. It would lead to an inferior scanning time.

The evaluation of this method starts by assigning labels to all the CT images in the dataset. For the experiments of this thesis, the label *damaged* or *undamaged* was associated with each image of the Jonagold apple dataset. Figure 47 (a) - (c) illustrates sample of images from the dataset assigned as *undamaged* and Figure 47 (d) - (f) illustrates sample of images from the dataset assigned as *damaged*. Such categorization into labels was made by a non-expert in food materials based on the size of holes inside the apples. However, many distinct categorizations can be made by experts to detect specific features in the data.

The rate of sinograms correct classified into the classes (*damaged* or *undamaged*) was computed using the 10-fold cross-validation scheme in eight experimental setups where 16, 32, 64, and 128 X-ray projections were acquired twice: initially, the object rotation in the conveyor belt (see Figure 16) was turned on; then, it was turned off. Figure 48 (a) shows the classification accuracy in the experimental setups at which the object rotation was allowed. As can be seen, the classification accuracy tends to grow as many X-ray projections are used indicating that such approach is more efficient than the evaluation

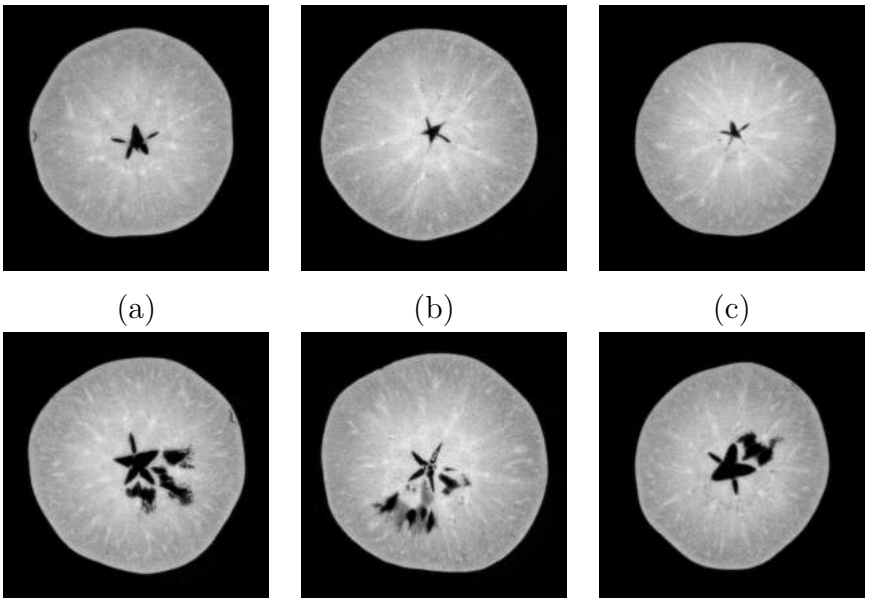

(a) (b) (c)

(d) (e) (f)

Figure 47 – Samples of images from the dataset assigned as *undamaged* (a) - (c) and *damaged* (d) - (f).

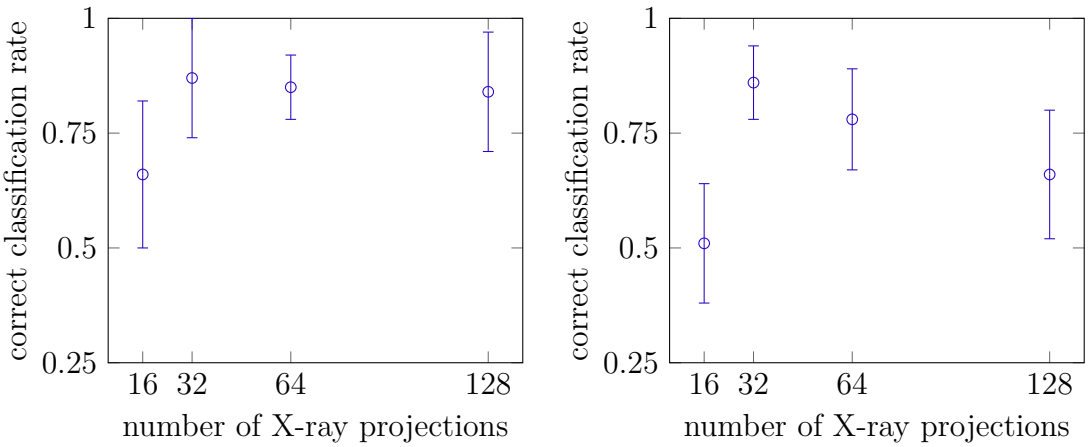

Figure 48 – Rate of classification accuracy of the samples of Jonagold apple dataset in the inline scanning setup with (a) and without (b) object rotation.

of conventional radiographs which are widely used at the industry [4]. However, the use of 32 X-ray projections to obtain an acceptable performance (87%) do not represent an apparent reduction in the scanning time in relation to the previous solutions. Figure 48 (b) shows that, in contrast to the methods proposed earlier which are based on image reconstruction, the final results are not significantly influenced by the rotation attribute of the conveyor belt. Such result may give rise to cheaper scanning setups at which the engines which allow object rotation in the conveyor belt are dismissed.

[4] see Section 1.1

7 CONCLUSION

In this thesis, an inline X-ray Computed Tomography (CT) scanning setup for industrial environments was described. The system comprises a fixed X-ray source and detector, and a linear translation of the target object in a conveyor belt. Compared to the conventional CT systems in which the X-source rotates around the object, the inline system has two main advantages: *(i)* it is more flexible for industrial environments since the object is imaged during its trajectory in a conveyor belt; *(ii)* it is cheaper since the mechanical engines used to rotate the radiation source around the object are dismissed. However, a huge trade-off between reconstruction quality and system throughput is imposed in such scenario. In this work, imaging simulations were performed to evaluate and quantify such trade-off. Thus, the findings enumerated as follows were obtained:

(i) Filtered Back Projection (FBP) algorithms cannot generate - in any way - reconstructions free of artifacts from the truncated projections acquired in the inline scanning geometry.

(ii) If object rotation is not applied in the conveyor belt, any conventional reconstruction technique produces images full of severe smearing artifacts no matter how many X-ray projections are used in the scanning stage.

(iii) If object rotation is applied to the conveyor belt, Simultaneous Iterative Reconstruction Technique (SIRT) using at least 32 X-ray projections can produce reconstructions of enough quality for object inspection purposes.

(iv) To acquired 32 X-ray projections, the scanning time is in between 17 seconds and 43 seconds for acceleration/deceleration in conveyor belts from 0.2 m/s^2 to 0.0025 m/s^2.

(v) The reconstruction time is less critical than the acquisition time. In fact, both FBP and SIRT can reconstruct 512×512 images from 32 X-ray projections in less than a second, which is an order of magnitude lower than the scanning time mentioned in the previous topic.

Methods were proposed in this thesis to introduce - via software - prior knowledge about the scanned objects into the CT imaging workflow to compensate the few number of X-ray projections that must be acquired to reduce the scanning time to the lowest possible while the quality of the image reconstruction is kept. The proposed methods were placed in both reconstruction and post-processing stages. In the reconstruction stage, the main idea was to exploit priors related to the material's composition and object shape. In

the post-processing stage, the main idea was to recover natural aspects of the images by using a training set of inline scanned images correctly segmented. The findings obtained from the experimental analysis of such methods are described as follows:

(vi) Discrete Algebraic Reconstruction Technique (DART), which incorporates priors related to the expected material's composition and its attenuation coefficient, can generate 90% accurate reconstructions from only 12 X-ray projections acquired in the inline setup. However, DART can achieve reconstruction times two orders of magnitude greater than SIRT.

(vii) If the reconstruction domain is constrained by using an Expected Object Domain (EOD), that requires a prior about the external object shape, into DART algorithm as proposed in this thesis, it is possible to achieve reconstruction convergences using a reduced number of iterations and, as a consequence, a reduced reconstruction time. However, even EOD-DART is not fast enough to provide the throughput required in industrial CT systems.

(viii) If Simultaneous Iterative Reconstruction Technique (SIRT) is adopted to reconstruct CT images from projections acquired in the inline scanning geometry, the post-processing stage based on Artificial Neural Network (ANN) proposed in this thesis can ensure at least 90% of accuracy to the final image reconstruction using only 16 X-ray projections. It represents a scanning time reduction from $19 - 37$ seconds to $15 - 29$ seconds, *i.e.* at least 21%.

(ix) Although the literature highlights the main drawback of SIRT as its computational cost in relation to FBP, it was shown in this thesis that it is possible to reduce the number of SIRT iterations until the reconstruction times became comparable to FBP. Then, to enhance the image artifacts generated by the precipitated end of SIRT algorithm, the proposed post-processing stage may be used.

Furthermore, to drastically reduces the number of X-ray projections acquired, it was also proposed a bypass from the acquisition stage to the analysis stage of the workflow. If correct classifications of the object were made from few X-ray projections, there would be no need for a reconstruction stage in such Non-destructive Testing (NDT) system. From initial evaluations of such approach, the following findings were obtained:

(x) As the classification accuracy grows as many X-ray projections are used, we may conclude that such approach substantially differs from the evaluation of conventional radiographs which are already widely used in the industry. The method evaluated in this thesis only obtained acceptable performance of classification using 32 X-ray projections. Thus, it cannot allow the expected acquisition time for inline industrial systems.

(xi) This was the only method evaluated in this thesis that the final results were not significantly influenced by the rotation of objects in the conveyor belt. A deeper investigation of such method may give rise to an even cheaper Non-destructive Testing (NDT) setup where the rotation engines in the conveyor belt are dismissed.

7.1 Contributions

The main contributions of this thesis consist of:

(i) **an investigation of a scanning geometry consisting of a single and static pair of X-ray source and detector**. In contrast, previous works - that also discussed CT solutions for industry - proposed the use of multiple pairs of X-ray source and detector or a non-stationary trajectory of, at least, one of them;

(ii) **the proposal of a Machine Learning-based post-processing stage** that can recovery natural aspect of the objects reconstructed using a smaller number of X-ray projections. As a consequence, the scanning time can be reduced in at least 21%;

(iii) **an improvement into the DART algorithm - the EOD-DART** - which constraints the reconstruction domain and allows a faster convergence of the algorithm by using a prior related to the outer object shape;

(iv) **a quantification of the trade-off between reconstruction quality and processing time in the inline CT system**. In fact, the results showed links processing time, conveyor belt acceleration/deceleration, number of X-ray projections, reconstruction accuracy, and image resolution;

(v) **introducing the idea of a compressed CT workflow for NDT systems consisting of only an acquisition stage and an analysis stage**. Such elimination of a reconstruction stage would reduce the need for a high number of X-ray projections and, as a consequence, improve the overall system throughput.

(vi) **a broad review of the methods previously proposed in the literature that exploit priors in distinct stages of the CT workflow**. Thus, we believe that such review will be helpful to any researcher that is going to work with low-dose and few-view CT;

7.2 Future Works

For future works, the following activities are planned:

(i) Expansion of Chapter 4 and submission of such material to a Journal as a Survey on methods for incorporate priors in few-view and low-dose CT systems. The surveys on dose reduction in CT published up to the present date, such as (KARABULUT; ARIYÜREK, 2006; LEE; CHHEM, 2010), are focused on *(i)* guidelines and procedures to be adopted by radiologists during the patient exam; and/or *(ii)* hardware-based solutions; and/or *(iii)* techniques which incorporate priors into the reconstruction stage of the CT workflow. To the best of our knowledge, a complete review on software-based solutions to incorporate priors into the pre-processing, reconstruction, and post-processing stage of the CT workflow - as showed in Chapter 4 is missing in the literature;

(ii) To investigate how fast can be an implementation of DART algorithm in a dedicated hardware device, such as a Field-Programmable Gate Array (FPGA). The main idea is to process in parallel the required computation for each pixel of the image. The basic iterative nature of DART algorithm needs to be kept. Even so, we believe that a drastic time reduction can be obtained by making that the processing of each pixel takes place in parallel in a dedicated hardware device. Thus, the solution exposed in Section would become practical to real-world scenarios;

(iii) To investigate how deep Artificial Neural Network (ANN) architectures, specially autoencoders, can generate new sinogram views from a limited number of projections. If such pre-processing method, followed by a reconstruction stage using the conventional Simultaneous Iterative Reconstruction Technique (SIRT), would improve the number of views, for instance, from 8 to 32 in the inline scanning geometry it would be possible to achieve acceptable reconstruction images using a very reduced scanning time;

(iv) To investigate how deep ANN architectures, specially Convolutional Neural Network (CNN), can improve the segmentation stage proposed in 5.1.2. Such Deep Learning-based techniques seem to have the potential of improving the results presented in this thesis;

(v) To investigate how different shape-based regularization methods can be incorporated together in Algebraic Reconstruction Techniques (ART) for providing better reconstruction results in the inline CT system;

(vi) To investigate how improvements in pre-reconstruction, reconstruction, and post-reconstruction stages of the CT workflow can be used simultaneously to improve the final results of the inline CT system.

7.3 Summary of publications

The research presented in this thesis led to the following publications:

- Conference proceedings:
  - L. F. Alves Pereira, A. Dabravolski, T. I. Ren, G. D. C. Cavalcanti and J. Sijbers, Conveyor Belt X-ray CT Using Domain Constrained Discrete Tomography, *Graphics, Patterns and Images (SIBGRAPI), 2014 27th SIBGRAPI Conference on*, Rio de Janeiro, 2014, pp. 290-297. (**status:** published, **Qualis-CC:** B1-2016)
- Journals:
  - L. F. Alves Pereira, E. Janssens, G. D. C. Cavalcanti, T. Ing Ren, M. Van Dael, P. Verboven, B. Nicolai and J. Sijbers, Inline X-ray Computed Tomography system based on Discrete Tomography: application to agricultural product inspection, *Computers and Electronics in Agriculture*, Volume 138, 2017, pp. 117-126. (**status:** published, **Qualis-CC:** A2-2015)
  - L. F. Alves Pereira, G. D. C. Cavalcanti, T. Ing Ren, and J. Sijbers, A machine learning approach for fast tomography. (**status:** in progress)

REFERENCES

AARLE, W. V. *Tomographic segmentation and discrete tomography for quantitative analysis of transmission tomography data*. 190 p. Dissertação (PhD thesis) — University of Antwerp, Antwerp, Belgium, 2012.

AARLE, W. van; PALENSTIJN, W. J.; CANT, J.; JANSSENS, E.; BLEICHRODT, F.; DABRAVOLSKI, A.; BEENHOUWER, J. D.; BATENBURG, K. J.; SIJBERS, J. Fast and flexible x-ray tomography using the astra toolbox. *Opt. Express*, OSA, v. 24, n. 22, p. 25129–25147, Oct 2016.

ABIDI, B. R.; ZHENG, Y.; GRIBOK, A. V.; ABIDI, M. A. Improving weapon detection in single energy x-ray images through pseudocoloring. *IEEE Transactions on Systems, Man, and Cybernetics, Part C (Applications and Reviews)*, IEEE, v. 36, n. 6, p. 784–796, 2006.

AHARON, M.; ELAD, M.; BRUCKSTEIN, A. K-svd: An algorithm for designing overcomplete dictionaries for sparse representation. *IEEE Transactions on signal processing*, IEEE, v. 54, n. 11, p. 4311–4322, 2006.

ANUAR, N. K.; WUI, W. T.; GHODGAONKAR, D. K.; TAIB, M. N. Characterization of hydroxypropylmethylcellulose films using microwave non-destructive testing technique. *Journal of pharmaceutical and biomedical analysis*, Elsevier, v. 43, n. 2, p. 549–557, 2007.

ARAPAKIS, I.; EFSTATHOPOULOS, E.; TSITSIA, V.; KORDOLAIMI, S.; ECONOMOPOULOS, N.; ARGENTOS, S.; PLOUSSI, A.; ALEXOPOULOU, E. Using "idose4" iterative reconstruction algorithm in adults' chest–abdomen–pelvis ct examinations: effect on image quality in relation to patient radiation exposure. *The British journal of radiology*, The British Institute of Radiology., v. 87, n. 1036, p. 20130613, 2014.

AYALEW, G.; HOLDEN, N. M.; GRACE, P. M.; WARD, S. M. Detection of glass contamination in horticultural peat with dual-energy X-ray absorptiometry (DXA). *Computers and Electronics in Agriculture*, v. 42, n. 1, p. 1 – 17, 2004.

BAHLMANN, C.; HEIDEMANN, G.; RITTER, H. Artificial neural networks for automated quality control of textile seams. *Pattern recognition*, Elsevier, v. 32, n. 6, p. 1049–1060, 1999.

BALDA, M.; HORNEGGER, J.; HEISMANN, B. Ray contribution masks for structure adaptive sinogram filtering. *IEEE transactions on medical imaging*, IEEE, v. 31, n. 6, p. 1228–1239, 2012.

BATENBURG, K. J. A network flow algorithm for reconstructing binary images from discrete x-rays. *Journal of Mathematical Imaging and Vision*, Springer, v. 27, n. 2, p. 175–191, 2007.

BATENBURG, K. J.; SIJBERS, J. Generic iterative subset algorithms for discrete tomography. *Discrete Applied Mathematics*, Elsevier, v. 157, n. 3, p. 438–451, 2009.

BATENBURG, K. J.; SIJBERS, J. Dart: a practical reconstruction algorithm for discrete tomography. *Image Processing, IEEE Transactions on*, IEEE, v. 20, n. 9, p. 2542–2553, 2011.

BATENBURG, K. J.; SIJBERS, J. Dart: a practical reconstruction algorithm for discrete tomography. *IEEE Transactions on Image Processing*, IEEE, v. 20, n. 9, p. 2542–2553, 2011.

BATES, D.; SMITH, G.; LU, D.; HEWITT, J. Rapid thermal non-destructive testing of aircraft components. *Composites Part B: Engineering*, Elsevier, v. 31, n. 3, p. 175–185, 2000.

BERNINGER, W. H.; REDINGTON, R. W. *Multiple purpose high speed tomographic x-ray scanner*. [S.l.]: Google Patents, 1980. US Patent 4,196,352.

BERTRAM, M.; ROSE, G.; SCHAFER, D.; WIEGERT, J.; AACH, T. Directional interpolation of sparsely sampled cone-beam ct sinogram data. In: IEEE. *Biomedical Imaging: Nano to Macro, 2004. IEEE International Symposium on*. [S.l.], 2004. p. 928–931.

BERTRAM, M.; WIEGERT, J.; SCHAFER, D.; AACH, T.; ROSE, G. Directional view interpolation for compensation of sparse angular sampling in cone-beam ct. *IEEE Transactions on Medical Imaging*, IEEE, v. 28, n. 7, p. 1011–1022, 2009.

BORSDORF, A.; RAUPACH, R.; FLOHR, T.; HORNEGGER, J. Wavelet based noise reduction in ct-images using correlation analysis. *IEEE transactions on medical imaging*, IEEE, v. 27, n. 12, p. 1685–1703, 2008.

BOSCH, A.; MUñOZ, X.; MARTí, R. Which is the best way to organize/classify images by content? *Image and Vision Computing*, v. 25, n. 6, p. 778 – 791, 2007. ISSN 0262-8856.

BOYD, D. P.; LIPTON, M. J. Cardiac computed tomography. *Proceedings of the IEEE*, IEEE, v. 71, n. 3, p. 298–307, 1983.

BROSNAN, T.; SUN, D.-W. Improving quality inspection of food products by computer vision—-a review. *Journal of Food Engineering*, Elsevier, v. 61, n. 1, p. 3–16, 2004.

BUADES, A.; COLL, B.; MOREL, J.-M. A non-local algorithm for image denoising. In: IEEE. *Computer Vision and Pattern Recognition, 2005. CVPR 2005. IEEE Computer Society Conference on*. [S.l.], 2005. v. 2, p. 60–65.

BUADES, A.; COLL, B.; MOREL, J.-M. A review of image denoising algorithms, with a new one. *Multiscale Modeling & Simulation*, SIAM, v. 4, n. 2, p. 490–530, 2005.

BUSHBERG, J.; SEIBERT, J.; LEIDHOLDT, E.; BOONE, J. *The Essential Physics of Medical Imaging*. [S.l.]: Wolters Kluwer Health, 2011. ISBN 9781451153941.

BUZUG, T. *Computed Tomography: From Photon Statistics to Modern Cone-Beam CT*. [S.l.]: Springer, 2008. ISBN 9783540394082.

CANDÈS, E. J.; ROMBERG, J.; TAO, T. Robust uncertainty principles: Exact signal reconstruction from highly incomplete frequency information. *IEEE Transactions on information theory*, IEEE, v. 52, n. 2, p. 489–509, 2006.

CARRASCO, M.; MERY, D. Automatic multiple view inspection using geometrical tracking and feature analysis in aluminum wheels. *Machine Vision and Applications*, Springer, v. 22, n. 1, p. 157–170, 2011.

CARVALHO, J. M.; MIRANDA, D. L. As exportações brasileiras de frutas: um panorama atual. 2009.

CHEN, H.; ZHANG, Y.; KALRA, M. K.; LIN, F.; CHEN, Y.; LIAO, P.; ZHOU, J.; WANG, G. Low-dose ct with a residual encoder-decoder convolutional neural network. *IEEE transactions on medical imaging*, IEEE, v. 36, n. 12, p. 2524–2535, 2017.

CHEN, H.; ZHANG, Y.; ZHANG, W.; LIAO, P.; LI, K.; ZHOU, J.; WANG, G. Low-dose ct via convolutional neural network. *Biomedical optics express*, Optical Society of America, v. 8, n. 2, p. 679–694, 2017.

CHEN, Y.; GAO, D.; NIE, C.; LUO, L.; CHEN, W.; YIN, X.; LIN, Y. Bayesian statistical reconstruction for low-dose x-ray computed tomography using an adaptive-weighting nonlocal prior. *Computerized Medical Imaging and Graphics*, Elsevier, v. 33, n. 7, p. 495–500, 2009.

CHEN, Y.; MA, J.; FENG, Q.; LUO, L.; SHI, P.; CHEN, W. Nonlocal prior bayesian tomographic reconstruction. *Journal of Mathematical Imaging and Vision*, Springer, v. 30, n. 2, p. 133–146, 2008.

CHEN, Y.; SHI, L.; FENG, Q.; YANG, J.; SHU, H.; LUO, L.; COATRIEUX, J.-L.; CHEN, W. Artifact suppressed dictionary learning for low-dose ct image processing. *IEEE transactions on medical imaging*, IEEE, v. 33, n. 12, p. 2271–2292, 2014.

CHEN, Y.; SHI, L.; YANG, J.; HU, Y.; LUO, L.; YIN, X.; COATRIEUX, J.-L. Radiation dose reduction with dictionary learning based processing for head ct. *Australasian Physical & Engineering Sciences in Medicine*, Springer, v. 37, n. 3, p. 483–493, 2014.

CHEN, Y.; YIN, X.; SHI, L.; SHU, H.; LUO, L.; COATRIEUX, J.-L.; TOUMOULIN, C. Improving abdomen tumor low-dose ct images using a fast dictionary learning based processing. *Physics in medicine and biology*, IOP Publishing, v. 58, n. 16, p. 5803, 2013.

CHEN, Z.; QI, H.; WU, S.; XU, Y.; ZHOU, L. Few-view ct reconstruction via a novel non-local means algorithm. *Physica Medica*, Elsevier, v. 32, n. 10, p. 1276–1283, 2016.

CHUANG, C.-L.; OUYANG, C.-S.; LIN, T.-T.; YANG, M.-M.; YANG, E.-C.; HUANG, T.-W.; KUEI, C.-F.; LUKE, A.; JIANG, J.-A. Automatic X-ray quarantine scanner and pest infestation detector for agricultural products. *Computers and Electronics in Agriculture*, v. 77, n. 1, p. 41 – 59, 2011. ISSN 0168-1699. Disponível em: <http://www.sciencedirect.com/science/article/pii/S0168169911000688>.

CIERNIAK, R. New neural network algorithm for image reconstruction from fan-beam projections. *Neurocomputing*, Elsevier, v. 72, n. 13, p. 3238–3244, 2009.

CLARK, M.; MCCANN, D.; FORDE, M. Application of infrared thermography to the non-destructive testing of concrete and masonry bridges. *Ndt & E International*, Elsevier, v. 36, n. 4, p. 265–275, 2003.

COLONNA, F.; EASLEY, G.; GUO, K.; LABATE, D. Radon transform inversion using the shearlet representation. *Applied and Computational Harmonic Analysis*, Elsevier, v. 29, n. 2, p. 232–250, 2010.

CSURKA, G.; DANCE, C.; FAN, L.; WILLAMOWSKI, J.; BRAY, C. Visual categorization with bags of keypoints. In: PRAGUE. *Workshop on statistical learning in computer vision, ECCV*. [S.l.], 2004. v. 1, n. 1-22, p. 1–2.

DABRAVOLSKI, A.; BATENBURG, K. J.; SIJBERS, J. A multiresolution approach to discrete tomography using dart. *PloS ONE*, Public Library of Science, v. 9, n. 9, p. e106090, 2014.

DENNHOVEN, M.; KUNZE, C.; KUEHN, R. *Baggage inspection device*. [S.l.]: Google Patents, 1977. US Patent 4,047,035.

DENNHOVEN, M.; KUNZE, C.; KUEHN, R. *Device for examining luggage by means of X-rays*. [S.l.]: Google Patents, 1979. US Patent 4,139,771.

EILBERT, R.; SHI, S. Improved imaging for x-ray inspection systems. *Aerospace and Electronic Systems Magazine, IEEE*, IEEE, v. 20, n. 3, p. 23–28, 2005.

ELAD, M. On the origin of the bilateral filter and ways to improve it. *IEEE Transactions on image processing*, IEEE, v. 11, n. 10, p. 1141–1151, 2002.

ERDOGAN, H.; FESSLER, J. A. Ordered subsets algorithms for transmission tomography. *Physics in medicine and biology*, IOP Publishing, v. 44, n. 11, p. 2835, 1999.

ETIEMBLE, A.; BESNARD, N.; ADRIEN, J.; TRAN-VAN, P.; GAUTIER, L.; LESTRIEZ, B.; MAIRE, E. Quality control tool of electrode coating for lithium-ion batteries based on x-ray radiography. *Journal of Power Sources*, Elsevier, v. 298, p. 285–291, 2015.

ETTER, V.; JOVANOVIC, I.; VETTERLI, M. Use of learned dictionaries in tomographic reconstruction. In: SPIE-INT SOC OPTICAL ENGINEERING, PO BOX 10, BELLINGHAM, WA 98227-0010 USA. *Proceedings of SPIE*. [S.l.], 2011. v. 8138, n. EPFL-CONF-169941.

FANTIDIS, J.; POTOLIAS, C.; BANDEKAS, D. Wind turbine blade nondestructive testing with a transportable radiography system. *Science and Technology of Nuclear Installations*, Hindawi Publishing Corporation, v. 2011, 2011.

FRESE, T.; BOUMAN, C. A.; SAUER, K. Multiscale bayesian methods for discrete tomography. In: *Discrete Tomography*. [S.l.]: Springer, 1999. p. 237–264.

GEMAN, S.; GEMAN, D. Stochastic relaxation, gibbs distributions, and the bayesian restoration of images. *IEEE Transactions on pattern analysis and machine intelligence*, IEEE, n. 6, p. 721–741, 1984.

GHETTI, C.; ORTENZIA, O.; SERRELI, G. Ct iterative reconstruction in image space: a phantom study. *Physica medica*, Elsevier, v. 28, n. 2, p. 161–165, 2012.

GINESU, G.; GIUSTO, D. D.; MARGNER, V.; MEINLSCHMIDT, P. Detection of foreign bodies in food by thermal image processing. *IEEE Transactions on Industrial Electronics*, IEEE, v. 51, n. 2, p. 480–490, 2004.

GONZALEZ, R. C.; WOODS, R. E. *Digital Image Processing (3rd Edition)*. Upper Saddle River, NJ, USA: Prentice-Hall, Inc., 2006.

GORDON, R.; BENDER, R.; HERMAN, G. T. Algebraic reconstruction techniques (art) for three-dimensional electron microscopy and x-ray photography. *Journal of theoretical Biology*, Elsevier, v. 29, n. 3, p. 471–481, 1970.

GOUILLART, E.; KRZAKALA, F.; MEZARD, M.; ZDEBOROVÁ, L. Belief-propagation reconstruction for discrete tomography. *Inverse Problems*, IOP Publishing, v. 29, n. 3, p. 035003, 2013.

GREEN, P. J. Bayesian reconstructions from emission tomography data using a modified em algorithm. *IEEE transactions on medical imaging*, IEEE, v. 9, n. 1, p. 84–93, 1990.

GUEDES, M. S. B.; SENA, M.; TOLEDO, S. Certificação como estratégia competitiva internacional dos produtores de frutas no Brasil. *VII Encontro da Sociedade de Economia Ecológica*, 2013.

HA, S.; MUELLER, K. Low dose ct image restoration using a localized patch database. In: IEEE. *2013 IEEE Nuclear Science Symposium and Medical Imaging Conference (2013 NSS/MIC)*. [S.l.], 2013. p. 1–2.

HA, S.; MUELLER, K. Low dose ct image restoration using a database of image patches. *Physics in medicine and biology*, IOP Publishing, v. 60, n. 2, p. 869, 2015.

HAFF, R. P.; TOYOFUKU, N. X-ray detection of defects and contaminants in the food industry. *Sensing and Instrumentation for Food Quality and Safety*, Springer, v. 2, n. 4, p. 262–273, 2008.

HE, D.; PANG, Y.; LODEWIJKS, G. Determination of acceleration for belt conveyor speed control in transient operation. *International Journal of Engineering and Technology*, IACSIT Press, v. 8, n. 3, p. 206, 2016.

HEUSSER, T.; BREHM, M.; RITSCHL, L.; SAWALL, S.; KACHELRIESS, M. Prior-based artifact correction (pbac) in computed tomography. *Medical physics*, American Association of Physicists in Medicine, v. 41, n. 2, p. 021906, 2014.

HEUSSER, T.; BREHM, M.; SAWALL, S.; KACHELRIESS, M. Ct data completion based on prior scans. In: IEEE. *Nuclear Science Symposium and Medical Imaging Conference (NSS/MIC), 2012 IEEE*. [S.l.], 2012. p. 2969–2976.

HO, T. K. The random subspace method for constructing decision forests. *IEEE transactions on pattern analysis and machine intelligence*, IEEE, v. 20, n. 8, p. 832–844, 1998.

HORI, K.; FUJIMOTO, T.; KAWANISHI, K. Development of ultra-fast x-ray computed tomography scanner system. *IEEE Transactions on Nuclear Science*, IEEE, v. 45, n. 4, p. 2089–2094, 1998.

HUANG, J.; MA, J.; LIU, N.; ZHANG, H.; BIAN, Z.; FENG, Y.; FENG, Q.; CHEN, W. Sparse angular ct reconstruction using non-local means based iterative-correction pocs. *Computers in Biology and Medicine*, Elsevier, v. 41, n. 4, p. 195–205, 2011.

JADIN, M. S.; TAIB, S. Recent progress in diagnosing the reliability of electrical equipment by using infrared thermography. *Infrared Physics & Technology*, Elsevier, v. 55, n. 4, p. 236–245, 2012.

JANSSENS, E.; PEREIRA, L. F. A.; BEENHOUWER, J. D.; TSANG, I. R.; DAEL, M. V.; VERBOVEN, P.; NICOLAI, B.; SIJBERS, J. Fast inline inspection by neural network based filtered backprojection: Application to apple inspection. *Case Studies in Nondestructive Testing and Evaluation*, v. 6, p. 14 – 20, 2016. ISSN 2214-6571. Special Issue: Industrial computed tomography.

JANSSENS, E.; PEREIRA, L. F. A.; BEENHOUWER, J. D.; TSANG, R.; DAEL, M. V.; VERBOVEN, P.; NICOLAÏ, B.; SIJBERS, J. Fast inline inspection by neural network based filtered backprojection: Application to apple inspection. *Case Studies in Nondestructive Testing and Evaluation*, Elsevier, v. 6, p. 14–20, 2016.

JASINIEN, E.; RAIUTIS, R.; VOLEIIS, A.; VLADIAUSKAS, A.; MITCHARD, D.; AMOS, M. et al. Ndt of wind turbine blades using adapted ultrasonic and radiographic techniques. *Insight-Non-Destructive Testing and Condition Monitoring*, The British Institute of Non-Destructive Testing, v. 51, n. 9, p. 477–483, 2009.

JIANG, J.-A.; CHANG, H.-Y.; WU, K.-H.; OUYANG, C.-S.; YANG, M.-M.; YANG, E.-C.; CHEN, T.-W.; LIN, T.-T. An adaptive image segmentation algorithm for X-ray quarantine inspection of selected fruits. *Computers and Electronics in Agriculture*, v. 60, n. 2, p. 190 – 200, 2008. ISSN 0168-1699. Disponível em: <http://www.sciencedirect.com/science/article/pii/S0168169907001767>.

JU, Y.; SAKA, M.; ABE, H. Nondestructive inspection of delamination in ic packages by high-frequency microwaves. *NDT & E International*, Elsevier, v. 34, n. 3, p. 213–217, 2001.

KAK, A.; SLANEY, M.; MEDICINE, I. E. in; SOCIETY, B. *Principles of Computerized Tomographic Imaging*. [S.l.]: IEEE Press, 1988. ISBN 9780879421984.

KALENDER, W. A. Technical foundations of spiral ct. In: ELSEVIER. *Seminars in Ultrasound, CT and MRI*. [S.l.], 1994. v. 15, n. 2, p. 81–89.

KALENDER, W. A. X-ray computed tomography. *Physics in medicine and biology*, IOP Publishing, v. 51, n. 13, p. R29, 2006.

KALKE, M.; SILTANEN, S. Sinogram interpolation method for sparse-angle tomography. *Applied Mathematics*, Scientific Research Publishing, v. 5, n. 03, p. 423, 2014.

KARABULUT, N.; ARIYÜREK, M. Low dose ct: practices and strategies of radiologists in university hospitals. *Diagnostic and Interventional Radiology*, Aves Yayincilik Ltd. STI., v. 12, n. 1, p. 3, 2006.

KARIMI, D.; WARD, R. K. Sinogram denoising via simultaneous sparse representation in learned dictionaries. *Physics in medicine and biology*, IOP Publishing, v. 61, n. 9, p. 3536, 2016.

KATSURA, M.; MATSUDA, I.; AKAHANE, M.; SATO, J.; AKAI, H.; YASAKA, K.; KUNIMATSU, A.; OHTOMO, K. Model-based iterative reconstruction technique for radiation dose reduction in chest ct: comparison with the adaptive statistical iterative reconstruction technique. *European radiology*, Springer, v. 22, n. 8, p. 1613–1623, 2012.

KATUNIN, A.; DRAGAN, K.; DZIENDZIKOWSKI, M. Damage identification in aircraft composite structures: A case study using various non-destructive testing techniques. *Composite structures*, Elsevier, v. 127, p. 1–9, 2015.

KELKAR, S.; BOUSHEY, C. J.; OKOS, M. A method to determine the density of foods using x-ray imaging. *Journal of food engineering*, Elsevier, v. 159, p. 36–41, 2015.

KOSTLER, H.; PRUMMER, M.; RUDE, U.; HORNEGGER, J. Adaptive variational sinogram interpolation of sparsely sampled ct data. In: IEEE. *Pattern Recognition, 2006. ICPR 2006. 18th International Conference on*. [S.l.], 2006. v. 3, p. 778–781.

KWON, J.-S.; LEE, J.-M.; KIM, W.-Y. Real-time detection of foreign objects using x-ray imaging for dry food manufacturing line. In: IEEE. *2008 IEEE International Symposium on Consumer Electronics*. [S.l.], 2008. p. 1–4.

LANGE, K.; CARSON, R. et al. Em reconstruction algorithms for emission and transmission tomography. *J. Comput. Assist. Tomogr*, v. 8, n. 2, p. 306–316, 1984.

LEE, T.-Y.; CHHEM, R. K. Impact of new technologies on dose reduction in ct. *European journal of radiology*, Elsevier, v. 76, n. 1, p. 28–35, 2010.

LEEA, H.; LEEA, J.; CHOA, S. View-interpolation of sparsely sampled sinogram using convolutional neural network. In: INTERNATIONAL SOCIETY FOR OPTICS AND PHOTONICS. *SPIE Medical Imaging*. [S.l.], 2017. p. 1013328–1013328.

LI, S.; CAO, Q.; CHEN, Y.; HU, Y.; LUO, L.; TOUMOULIN, C. Dictionary learning based sinogram inpainting for ct sparse reconstruction. *Optik-International Journal for Light and Electron Optics*, Elsevier, v. 125, n. 12, p. 2862–2867, 2014.

LI, T.; LI, X.; WANG, J.; WEN, J.; LU, H.; HSIEH, J.; LIANG, Z. Nonlinear sinogram smoothing for low-dose x-ray ct. *IEEE Transactions on Nuclear Science*, IEEE, v. 51, n. 5, p. 2505–2513, 2004.

LI, X.; TSO, S. K.; GUAN, X.-P.; HUANG, Q. Improving automatic detection of defects in castings by applying wavelet technique. *IEEE Transactions on Industrial Electronics*, IEEE, v. 53, n. 6, p. 1927–1934, 2006.

LI, Y.; CHEN, Y.; HU, Y.; OUKILI, A.; LUO, L.; CHEN, W.; TOUMOULIN, C. Strategy of computed tomography sinogram inpainting based on sinusoid-like curve decomposition and eigenvector-guided interpolation. *JOSA A*, Optical Society of America, v. 29, n. 1, p. 153–163, 2012.

LIAO, P.-S.; CHEN, T.-S.; CHUNG, P.-C. et al. A fast algorithm for multilevel thresholding. *J. Inf. Sci. Eng.*, v. 17, n. 5, p. 713–727, 2001.

LIU, L. Model-based iterative reconstruction: a promising algorithm for today's computed tomography imaging. *Journal of Medical imaging and Radiation sciences*, Elsevier, v. 45, n. 2, p. 131–136, 2014.

LU, H.; LI, X.; HSIAO, I.-T.; LIANG, Z. Analytical noise treatment for low-dose ct projection data by penalized weighted least-square smoothing in the kl domain. In: *SPIE Medical Imaging*. [S.l.: s.n.], 2002. v. 4682, p. 146–152.

LU, Y.; ZHAO, J.; WANG, G. Few-view image reconstruction with dual dictionaries. *Physics in medicine and biology*, IOP Publishing, v. 57, n. 1, p. 173, 2011.

MA, J.; HUANG, J.; FENG, Q.; ZHANG, H.; LU, H.; LIANG, Z.; CHEN, W. Low-dose computed tomography image restoration using previous normal-dose scan. *Medical physics*, American Association of Physicists in Medicine, v. 38, n. 10, p. 5713–5731, 2011.

MA, X. F.; FUKUHARA, M.; TAKEDA, T. Neural network ct image reconstruction method for small amount of projection data. *Nuclear Instruments and Methods in Physics Research Section A: Accelerators, Spectrometers, Detectors and Associated Equipment*, Elsevier, v. 449, n. 1, p. 366–377, 2000.

MAHMOOD, K.; CARMONA, P. L.; SHAHBAZMOHAMADI, S.; PLA, F.; JAVIDI, B. Real-time automated counterfeit integrated circuit detection using x-ray microscopy. *Applied Optics*, Optical Society of America, v. 54, n. 13, p. D25–D32, 2015.

MAIRE, E.; WITHERS, P. Quantitative x-ray tomography. *International materials reviews*, Taylor & Francis, v. 59, n. 1, p. 1–43, 2014.

MANDUCA, A.; YU, L.; TRZASKO, J. D.; KHAYLOVA, N.; KOFLER, J. M.; MCCOLLOUGH, C. M.; FLETCHER, J. G. Projection space denoising with bilateral filtering and ct noise modeling for dose reduction in ct. *Medical physics*, Wiley Online Library, v. 36, n. 11, p. 4911–4919, 2009.

MANICKAVASAGAN, A.; JAYAS, D. S.; WHITE, N. D.; PALIWAL, J. Applications of thermal imaging in agriculture–a review. *The Canadian society for engineering in agriculture, food and biological systems, paper*, p. 05–002, 2005.

MATHANKER, S.; WECKLER, P.; BOWSER, T.; WANG, N.; MANESS, N. Adaboost classifiers for pecan defect classification. *Computers and electronics in agriculture*, Elsevier, v. 77, n. 1, p. 60–68, 2011.

MEOLA, C. Infrared thermography of masonry structures. *Infrared physics & technology*, Elsevier, v. 49, n. 3, p. 228–233, 2007.

MERY, D. Crossing line profile: a new approach to detecting defects in aluminium die casting. In: SPRINGER. *Scandinavian Conference on Image Analysis*. [S.l.], 2003. p. 725–732.

MERY, D. Automated radioscopic inspection of aluminum die castings. *Materials Evaluation*, v. 65, n. 6, p. 643–647, 2006.

MERY, D.; FILBERT, D. Automated flaw detection in aluminum castings based on the tracking of potential defects in a radioscopic image sequence. *IEEE Transactions on Robotics and Automation*, IEEE, v. 18, n. 6, p. 890–901, 2002.

MERY, D.; LILLO, I.; LOEBEL, H.; RIFFO, V.; SOTO, A.; CIPRIANO, A.; AGUILERA, J. M. Automated fish bone detection using X-ray imaging. *Journal of food engineering*, Elsevier, v. 105, n. 3, p. 485–492, 2011.

MICHEL, S.; KOLLER, S. M.; RUITER, J. C. de; MOERLAND, R.; HOGERVORST, M.; SCHWANINGER, A. Computer-based training increases efficiency in x-ray image interpretation by aviation security screeners. In: IEEE. *2007 41st Annual IEEE International Carnahan Conference on Security Technology*. [S.l.], 2007. p. 201–206.

MORI, S.; ENDO, M.; TSUNOO, T.; KANDATSU, S.; TANADA, S.; ARADATE, H.; SAITO, Y.; MIYAZAKI, H.; SATOH, K.; MATSUSHITA, S. et al. Physical performance evaluation of a 256-slice ct-scanner for four-dimensional imaging. *Medical physics*, American Association of Physicists in Medicine, v. 31, n. 6, p. 1348–1356, 2004.

MORRISON, D.; ABEYRATNE, U. Ultrasonic technique for non-destructive quality evaluation of oranges. *Journal of Food Engineering*, Elsevier, v. 141, p. 107–112, 2014.

MORTON, E.; LUGGAR, R.; KEY, R.; KUNDU, A.; TAVORA, L.; GILBOY, W. Development of a high speed x-ray tomography system for multiphase flow imaging. In: IEEE. *Nuclear Science Symposium, 1998. Conference Record. 1998 IEEE*. [S.l.], 1998. v. 2, p. 995–999.

MORTON, E.; MANN, K.; BERMAN, A.; KNAUP, M.; KACHELRIEß, M. Ultrafast 3D reconstruction for x-ray real-time tomography (RTT). In: *Nuclear Science Symposium Conference Record (NSS/MIC), 2009 IEEE*. [S.l.: s.n.], 2009. p. 4077–4080. ISSN 1095-7863.

NAGURNEY, A.; LI, D. A supply chain network game theory model with product differentiation, outsourcing of production and distribution, and quality and price competition. *Annals of Operations Research*, Springer, v. 226, n. 1, p. 479–503, 2015.

NERCESSIAN, S.; PANETTA, K.; AGAIAN, S. Automatic detection of potential threat objects in x-ray luggage scan images. In: IEEE. *Technologies for Homeland Security, 2008 IEEE Conference on*. [S.l.], 2008. p. 504–509.

NEROLADAKI, A.; BOTSIKAS, D.; BOUDABBOUS, S.; BECKER, C. D.; MONTET, X. Computed tomography of the chest with model-based iterative reconstruction using a radiation exposure similar to chest x-ray examination: preliminary observations. *European radiology*, Springer, v. 23, n. 2, p. 360–366, 2013.

NIELSEN, M. S.; CHRISTENSEN, L. B.; FEIDENHANS, R. Frozen and defrosted fruit revealed with x-ray dark-field radiography. *Food Control*, Elsevier, v. 39, p. 222–226, 2014.

NIEMI, E.; LASSAS, M.; SILTANEN, S. Dynamic x-ray tomography with multiple sources. In: IEEE. *2013 8th International Symposium on Image and Signal Processing and Analysis (ISPA)*. [S.l.], 2013. p. 618–621.

OERTEL, C.; BOCK, P. Identification of objects-of-interest in x-ray images. In: IEEE. *35th IEEE Applied Imagery and Pattern Recognition Workshop (AIPR'06)*. [S.l.], 2006. p. 17–17.

OGAWA, Y.; KONDO, N.; SHIBUSAWA, S. Inside quality evaluation of fruit by x-ray image. In: IEEE. *Advanced Intelligent Mechatronics, 2003. AIM 2003. Proceedings. 2003 IEEE/ASME International Conference on*. [S.l.], 2003. v. 2, p. 1360–1365.

OSKOUI, P.; STARK, H. A comparative study of three reconstruction methods for a limited-view computer tomography problem. *IEEE Transactions on Medical imaging*, IEEE, v. 8, n. 1, p. 43–49, 1989.

PELT, D. M.; BATENBURG, K. J. Fast tomographic reconstruction from limited data using artificial neural networks. *IEEE Transactions on Image Processing*, IEEE, v. 22, n. 12, p. 5238–5251, 2013.

PIERCE, B. L.; SHELTON, D. J.; LONGBOTHAM, H. G.; BADDIPUDI, S.; YAN, P. Automated inspection of through hole solder joints utilizing x-ray imaging. In: IEEE. *AUTOTESTCON'93. IEEE Systems Readiness Technology Conference. Proceedings*. [S.l.], 1993. p. 191–196.

PLANÈS, T.; LAROSE, E. A review of ultrasonic coda wave interferometry in concrete. *Cement and Concrete Research*, Elsevier, v. 53, p. 248–255, 2013.

QI, H.; CHEN, Z.; WU, S.; XU, Y.; ZHOU, L. Iterative image reconstruction using modified non-local means filtering for limited-angle computed tomography. *Physica Medica*, Elsevier, v. 32, n. 9, p. 1041–1051, 2016.

RACK, A.; GARCIA-MORENO, F.; SCHMITT, C.; BETZ, O.; CECILIA, A.; ERSHOV, A.; RACK, T.; BANHART, J.; ZABLER, S. On the possibilities of hard x-ray imaging with high spatio-temporal resolution using polychromatic synchrotron radiation. *Journal of X-ray Science and Technology*, IOS Press, v. 18, n. 4, p. 429–441, 2010.

RADON, J. On the determination of functions from their integral values along certain manifolds. *Medical Imaging, IEEE Transactions on*, v. 5, n. 4, p. 170–176, Dec 1986. ISSN 0278-0062.

RIVIERE, P. J. L. Penalized-likelihood sinogram smoothing for low-dose ct. *Medical physics*, Wiley Online Library, v. 32, n. 6, p. 1676–1683, 2005.

ROBB, R. A.; HOFFMAN, E. A.; SINAK, L. J.; HARRIS, L. D.; RITMAN, E. L. High-speed three-dimensional x-ray computed tomography: The dynamic spatial reconstructor. *Proceedings of the IEEE*, IEEE, v. 71, n. 3, p. 308–319, 1983.

ROCKMORE, A. J.; MACOVSKI, A. A maximum likelihood approach to emission image reconstruction from projections. *IEEE transactions on nuclear science*, IEEE, v. 23, n. 4, p. 1428–1432, 1976.

RUMELHART, D. E.; HINTON, G. E.; WILLIAMS, R. J. *Learning internal representations by error propagation*. [S.l.], 1985.

SAKAI, Y.; YUSA, N.; ITO, S.; HASHIZUME, H. Numerical analysis of microwave ndt applied to piping inspection. *Materials Transactions*, The Japan Institute of Metals and Materials, v. 53, n. 4, p. 627–630, 2012.

SAUER, K.; BOUMAN, C. A local update strategy for iterative reconstruction from projections. *IEEE Transactions on Signal Processing*, IEEE, v. 41, n. 2, p. 534–548, 1993.

SCHEFFEL, H.; STOLZMANN, P.; SCHLETT, C. L.; ENGEL, L.-C.; MAJOR, G. P.; KÁROLYI, M.; DO, S.; MAUROVICH-HORVAT, P.; HOFFMANN, U. Coronary artery plaques: cardiac ct with model-based and adaptive-statistical iterative reconstruction technique. *European journal of radiology*, Elsevier, v. 81, n. 3, p. e363–e369, 2012.

SCHÜLE, T.; SCHNÖRR, C.; WEBER, S.; HORNEGGER, J. Discrete tomography by convex–concave regularization and dc programming. *Discrete Applied Mathematics*, Elsevier, v. 151, n. 1, p. 229–243, 2005.

SHAO, J.; DU, D.; CHANG, B.; SHI, H. Automatic weld defect detection based on potential defect tracking in real-time radiographic image sequence. *NDT & E International*, Elsevier, v. 46, p. 14–21, 2012.

SHEPP, L. A.; LOGAN, B. F. The fourier reconstruction of a head section. *IEEE Transactions on Nuclear Science*, IEEE, v. 21, n. 3, p. 21–43, 1974.

SHEPP, L. A.; VARDI, Y. Maximum likelihood reconstruction for emission tomography. *IEEE transactions on medical imaging*, IEEE, v. 1, n. 2, p. 113–122, 1982.

SHULL, P. J. *Nondestructive evaluation: theory, techniques, and applications*. [S.l.]: CRC press, 2002.

SIDKY, E. Y.; KAO, C.-M.; PAN, X. Accurate image reconstruction from few-views and limited-angle data in divergent-beam ct. *Journal of X-ray Science and Technology*, IOS Press, v. 14, n. 2, p. 119–139, 2006.

SIDKY, E. Y.; PAN, X. Image reconstruction in circular cone-beam computed tomography by constrained, total-variation minimization. *Physics in medicine and biology*, IOP Publishing, v. 53, n. 17, p. 4777, 2008.

SINGH, M.; SINGH, S. Optimizing image enhancement for screening luggage at airports. In: IEEE. *CIHSPS 2005. Proceedings of the 2005 IEEE International Conference on Computational Intelligence for Homeland Security and Personal Safety, 2005.* [S.l.], 2005. p. 131–136.

SINGH, S.; KALRA, M. K.; GILMAN, M. D.; HSIEH, J.; PIEN, H. H.; DIGUMARTHY, S. R.; SHEPARD, J.-A. O. Adaptive statistical iterative reconstruction technique for radiation dose reduction in chest ct: a pilot study. *Radiology*, Radiological Society of North America, Inc., v. 259, n. 2, p. 565–573, 2011.

SMITH-BINDMAN, R.; LIPSON, J.; MARCUS, R.; KIM, K.-P.; MAHESH, M.; GOULD, R.; GONZÁLEZ, A. B. de; MIGLIORETTI, D. L. Radiation dose associated with common computed tomography examinations and the associated lifetime attributable risk of cancer. *Archives of internal medicine*, American Medical Association, v. 169, n. 22, p. 2078–2086, 2009.

SOLTANI, S.; ANDERSEN, M. S.; HANSEN, P. C. Tomographic image reconstruction using training images. *arXiv preprint arXiv:1503.01993*, 2015.

SOLTANI, S.; ANDERSEN, M. S.; HANSEN, P. C. Tomographic image reconstruction using training images. *Journal of Computational and Applied Mathematics*, Elsevier, v. 313, p. 243–258, 2017.

TAGUCHI, K.; ARADATE, H. Algorithm for image reconstruction in multi-slice helical ct. *Medical Physics*, American Association of Physicists in Medicine, v. 25, n. 4, p. 550–561, 1998.

THIBAULT, J.-B.; SAUER, K. D.; BOUMAN, C. A.; HSIEH, J. A three-dimensional statistical approach to improved image quality for multislice helical ct. *Medical physics*, Wiley Online Library, v. 34, n. 11, p. 4526–4544, 2007.

THOMPSON, W. M.; LIONHEART, W. R.; MORTON, E. J.; CUNNINGHAM, M.; LUGGAR, R. D. High speed imaging of dynamic processes with a switched source x-ray ct system. *Measurement Science and Technology*, IOP Publishing, v. 26, n. 5, p. 055401, 2015.

UEHARA, M.; YASHIRO, W.; MOMOSE, A. Effectiveness of x-ray grating interferometry for non-destructive inspection of packaged devices. *Journal of Applied Physics*, AIP Publishing, v. 114, n. 13, p. 134901, 2013.

VERAVERBEKE, E. A.; VERBOVEN, P.; LAMMERTYN, J.; CRONJE, P.; BAERDEMAEKER, J. D.; NICOLAÏ, B. M. Thermographic surface quality evaluation of apple. *Journal of food engineering*, Elsevier, v. 77, n. 1, p. 162–168, 2006.

VILAR, R.; ZAPATA, J.; RUIZ, R. An automatic system of classification of weld defects in radiographic images. *NDT & E International*, Elsevier, v. 42, n. 5, p. 467–476, 2009.

WANG, G.; LIAO, T. W. Automatic identification of different types of welding defects in radiographic images. *Ndt & E International*, Elsevier, v. 35, n. 8, p. 519–528, 2002.

WANG, J.; LI, T.; LU, H.; LIANG, Z. Noise reduction for low-dose single-slice helical ct sinograms. *IEEE transactions on nuclear science*, IEEE, v. 53, n. 3, p. 1230–1237, 2006.

WANG, J.; LU, H.; WEN, J.; LIANG, Z. Multiscale penalized weighted least-squares sinogram restoration for low-dose x-ray computed tomography. *IEEE Transactions on Biomedical Engineering*, IEEE, v. 55, n. 3, p. 1022–1031, 2008.

WANG, Y.; WANG, M.; ZHANG, Z. Microfocus x-ray printed circuit board inspection system. *Optik-International Journal for Light and Electron Optics*, Elsevier, v. 125, n. 17, p. 4929–4931, 2014.

WEBER, S.; SCHNORR, C.; HORNEGGER, J. A linear programming relaxation for binary tomography with smoothness priors. *Electronic Notes in Discrete Mathematics*, Elsevier, v. 12, p. 243–254, 2003.

WELLS, K.; BRADLEY, D. A review of x-ray explosives detection techniques for checked baggage. *Applied Radiation and Isotopes*, Elsevier, v. 70, n. 8, p. 1729–1746, 2012.

WÜRFL, T.; GHESU, F. C.; CHRISTLEIN, V.; MAIER, A. Deep learning computed tomography. In: SPRINGER. *International Conference on Medical Image Computing and Computer-Assisted Intervention*. [S.l.], 2016. p. 432–440.

XU, Q.; YU, H.; MOU, X.; ZHANG, L.; HSIEH, J.; WANG, G. Low-dose x-ray ct reconstruction via dictionary learning. *IEEE transactions on medical imaging*, NIH Public Access, v. 31, n. 9, p. 1682, 2012.

XU, Q.; YU, H.; WANG, G.; MOU, X. Dictionary learning based low-dose x-ray ct reconstruction. In: *Frontiers of Medical Imaging*. [S.l.]: World Scientific, 2015. p. 99–119.

XU, W.; HA, S.; MUELLER, K. Database-assisted low-dose ct image restoration. *Medical physics*, American Association of Physicists in Medicine, v. 40, n. 3, p. 031109, 2013.

XU, W.; MUELLER, K. A reference image database approach for nlm filter-regularized ct reconstruction. *Proc. Fully3D*, p. 116–119, 2011.

YANG, M.; LIU, Q.; ZHAO, H.; LI, Z.; LIU, B.; LI, X.; MENG, F. Automatic x-ray inspection for escaped coated particles in spherical fuel elements of high temperature gas-cooled reactor. *Energy*, Elsevier, v. 68, p. 385–398, 2014.

YAZDANI, S.; YUSOF, R.; RIAZI, A.; KARIMIAN, A.; HEMATIAN, A. Evaluation of pipelines in industrial radiography using image processing techniques. *Advanced Science, Engineering and Medicine*, American Scientific Publishers, v. 6, n. 1, p. 81–85, 2014.

YE, G.; NEAL, B.; BOOT, A.; KAPPATOS, V.; SELCUK, C.; GAN, T.-H. Development of an ultrasonic ndt system for automated in-situ inspection of wind turbine blades. In: *EWSHM-7th European Workshop on Structural Health Monitoring*. [S.l.: s.n.], 2014.

YEDIDIA, J. S.; FREEMAN, W. T.; WEISS, Y. Understanding belief propagation and its generalizations. *Exploring artificial intelligence in the new millennium*, v. 8, p. 236–239, 2003.

YU, H.; ZHAO, S.; HOFFMAN, E. A.; WANG, G. Ultra-low dose lung ct perfusion regularized by a previous scan. *Academic radiology*, Elsevier, v. 16, n. 3, p. 363–373, 2009.

ZAHRAN, O.; KASBAN, H.; EL-KORDY, M.; EL-SAMIE, F. A. Automatic weld defect identification from radiographic images. *NDT & E International*, Elsevier, v. 57, p. 26–35, 2013.

ZAPATA, J.; VILAR, R.; RUIZ, R. Performance evaluation of an automatic inspection system of weld defects in radiographic images based on neuro-classifiers. *Expert Systems with Applications*, Elsevier, v. 38, n. 7, p. 8812–8824, 2011.

ZHANG, G.; ZHANG, L.; CHEN, Z. An hl curve method for material discrimination of dual energy x-ray inspection systems. In: IEEE. *IEEE Nuclear Science Symposium Conference Record, 2005*. [S.l.], 2005. v. 1, p. 326–328.

ZHANG, H.; MA, J.; WANG, J.; LIU, Y.; LU, H.; LIANG, Z. Statistical image reconstruction for low-dose ct using nonlocal means-based regularization. *Computerized Medical Imaging and Graphics*, Elsevier, v. 38, n. 6, p. 423–435, 2014.

GLOSSARY

artifacts image errors that may emerge in Computed Tomography (CT) reconstructions due to a variety of reasons, such as missing projection data. 39, 59, 64, 83, 84

attenuation coefficient indicates how intense is the loss of X-ray photons in the interaction of the radiation beam with matter at each object position. In a Computed Tomography (CT) image reconstruction, the gray level at each pixel represents the material's attenuation coefficient on that object's position. 29, 33, 37, 55–58, 72, 84, 102

missing wedge non-sampled projection angles during an X-ray data acquisition in Computed Tomography (CT). 39

phantom digital images used to model object's material response to a specif type of radiation in the development and testing of imaging systems such as Magnetic Resonance Imaging (MRI), Computed Tomography (CT), and Positron Emission Tomography (PET). 12, 53, 72, 106

scanning geometry refers to the relative position of the X-ray source, detector, and target object during the acquisition of X-ray projections. 25, 31, 33, 43, 83–86

sinogram visual representation of the raw data acquired in Computed Tomography (CT) processing. 22, 50–55, 58, 69–71, 81, 86, 105

APPENDIX A - DOMAINS IN A CT PROCESSING

This quick overview on the distinct domains of a CT is based on the very well written summary presented in (AARLE, 2012).

The CT image reconstruction problem involves three domains: the object function domain, the projection domain, and the reconstruction domain. Each of those are described as follows, and the relation between them are illustrated in Figure 49.

- **object function domain** refers to a rectangular coordinate system at which an object function $f(x, y)$ is defined. The value at each point (x, y) represents the attenuation coefficient μ, *i.e.* the density level of the material, in that specific position.
- **projection domain** refers to a cilindric coordinate system at which an projection function $g(\theta, d)$ is defined. The values along $g(\theta_z, d)$ represents the values registered by the X-ray detector for a given projection angle θ_z. The values along $g(\theta, d_k)$ represents the values registered in one detector cell d_k for every projection angle evaluated.
- **reconstruction domain** refers to a rectangular coordinate system at which a reconstruction function $f'(x, y)$ is defined. The value at each point (x, y) is the most probable attenuation coefficient for that position according to the projection data available and a given image reconstruction technique.

From a real object, a projection data is generated by an X-ray CT scanning system. Such mechanical scanning is mathematically equivalent to apply the Radon transform[1] to the data in the object function domain. Then, the projection data can be mapped into a reconstruction domain via any reconstruction procedure, which is usually based on the Inverse Radon transform.

[1] for a detailed description about the Radon transform and the inverse Radom transform, see Appendix B

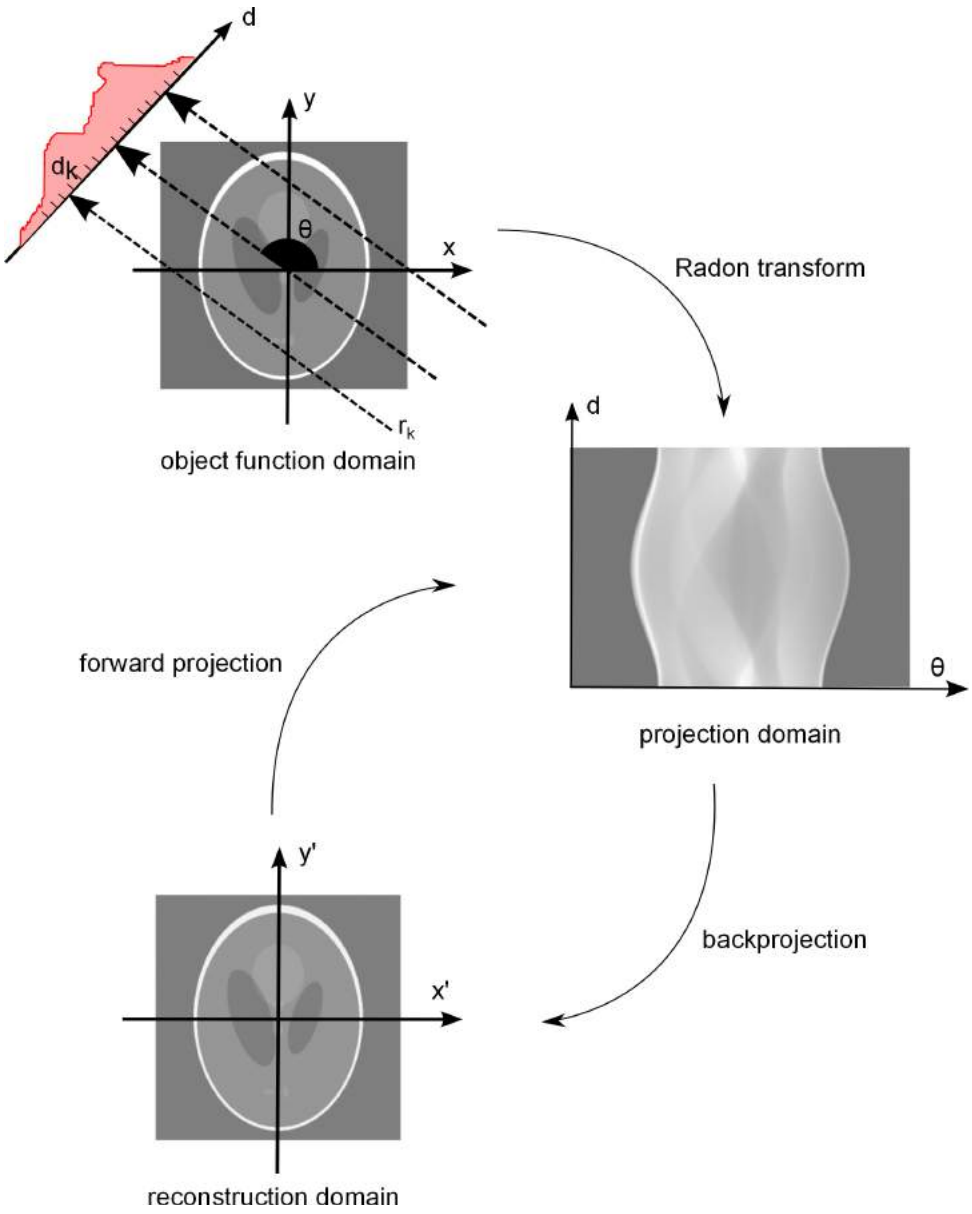

Figure 49 – Relation between the object function domain, projection domain and reconstruction domain in a CT reconstruction process.

APPENDIX B - RADON TRANSFORM

Johann Karl August Radon published the results of his research in German in 1917 and the reader can find an English translation of the original Radon's work in (RADON, 1986). However, due to the mathematical complexity and formalism presented there, this section was written based in the very didactic explanation given in (GONZALEZ; WOODS, 2006).

Consider a straight line in the Cartesian coordinate system, as illustrated in Figure 50. Such line is described by $y = ax + b$, or by its normal form as follows:

$$x\cos\theta + y\sin\theta = \rho \tag{B.1}$$

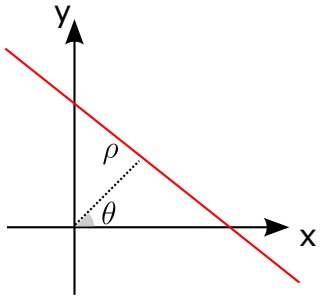

Figure 50 – Normal (or perpendicular) form of equation of line.

Given a target object described by $f(x, y)$ at the $xy-$plane, the object's projection in the perpendicular direction to θ_k, as illustrated in Figure 51, is the sum of the values of $f(x, y)$ within the paths $x\cos\theta_k + y\sin\theta_k = \rho_j$ for every ρ_j.

The Radon Transform $(\mathcal{R}f)(\theta, \rho)$ calculates the projections of $f(x, y)$ for all ρ and θ. For continuous values, the Radon Transform is defined as:

$$(\mathcal{R}f)(\theta, \rho) = g(\rho, \theta) = \int_{-\infty}^{\infty}\int_{-\infty}^{\infty} f(x, y)\delta(x\cos\theta + y\sin\theta - \rho)dxdy \tag{B.2}$$

where $\delta(\cdot)$ is the delta Dirac function which ensures that the right side of Equation (B.2) is zero except for the points (x', y') which relies in the line $x\cos\theta_k + y\sin\theta_k = \rho_j$.

The inverse Radon Transform proposed by Johann Radon, which recover the function $f(x, y)$ from the data $g(\rho, \theta)$ in the *projection space*, may be written as described by (COLONNA et al., 2010):

$$f(x, y) = \frac{1}{4\pi^2}\int_{-\infty}^{\infty}\int_{-\infty}^{\infty}\frac{\frac{\partial}{\partial\rho}g(\rho, \theta)}{x\cdot\theta - \rho}d\rho d\theta \tag{B.3}$$

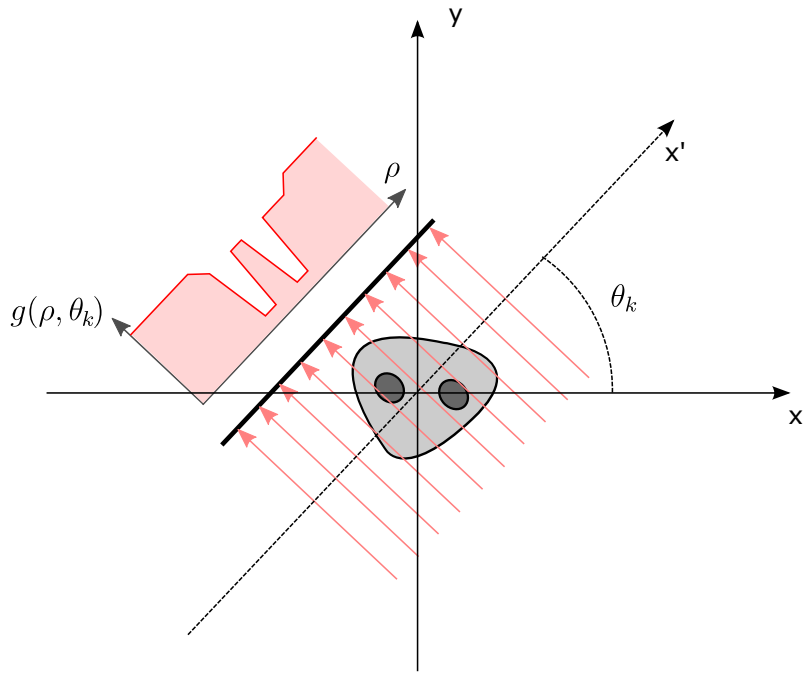

Figure 51 – The projection of a target object, described by $f(x, y)$, in the perpendicular direction to θ_k, is the sum of the values of $f(x, y)$ within the paths $x \cos\theta_k + y \sin\theta_k = \rho_j$ for every ρ_j.

For Digital Image Processing, Radon Transform must be considered on its discrete case. Then, Equation (B.2) become:

$$g(\rho, \theta) = \sum_{x=0}^{M-1} \sum_{y=0}^{N-1} f(x, y)\delta(x \cos\theta + y \sin\theta - \rho) \tag{B.4}$$

at which x, y, ρ and θ are now discrete variables.

Figure 52 (b) and (d) shows the sinograms, generated using Equation (B.4), related to the digital images (a) and (c), respectively. Each column in the sinogram is the object's projection along the perpendicular direction to θ_k.

The inversion method mathematically described by Johann Radon in Equation (B.3) is highly complex, thus its conversion into an accurate and efficient computational algorithm is far from obvious, as discussed by (COLONNA et al., 2010). Therefore, Computed Tomography (CT) systems, along the years, has been making use of a number of algorithms and techniques to implement the inverse Radon Transform. The most meaningful image reconstruction techniques used in CT scans will be discussed later in this thesis.

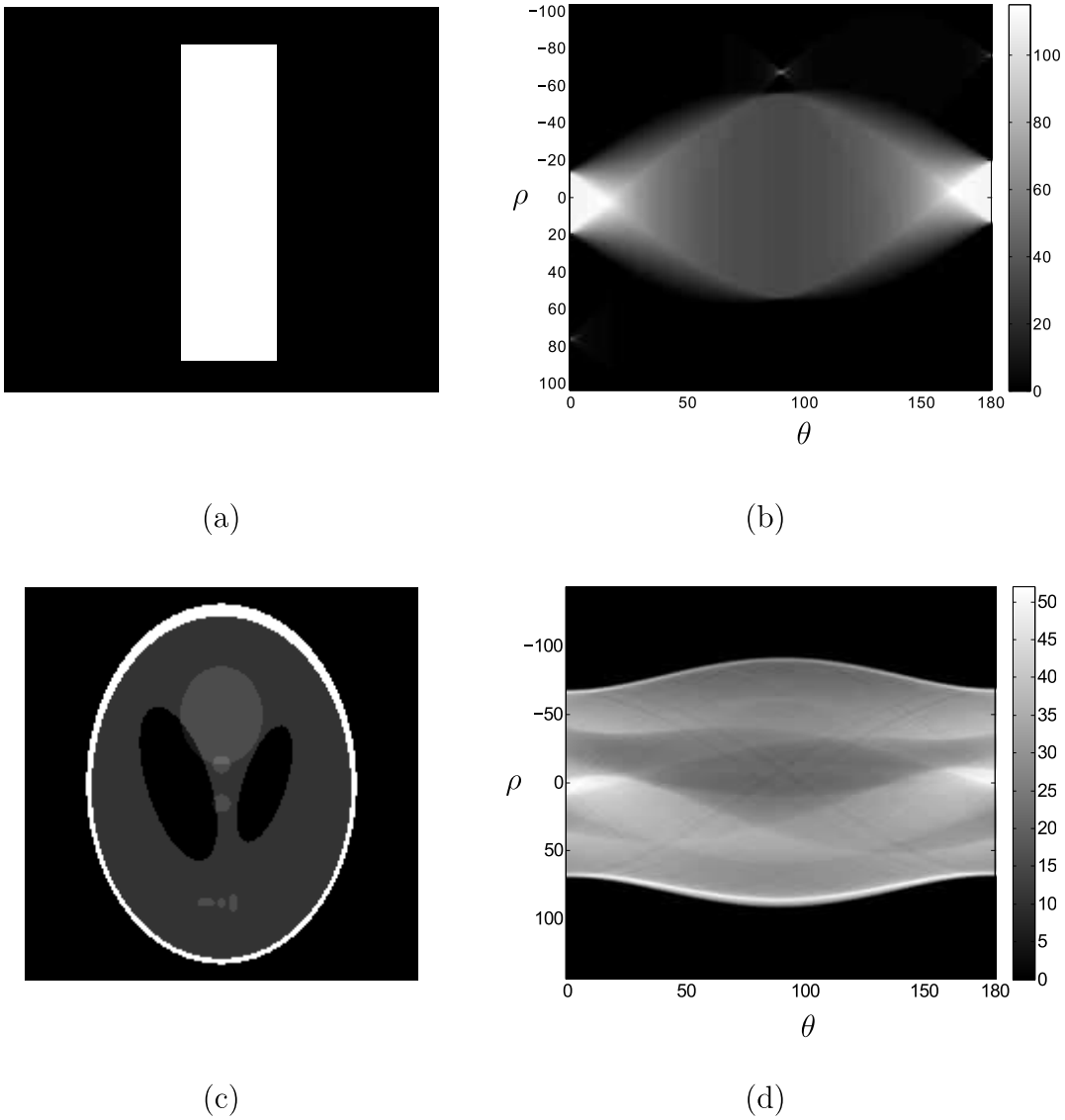

Figure 52 – Examples of digital images $f(x, y)$ in (a) and (c) and its respective Radon Transforms $g(\rho, \theta)$. (c) shows a *Sheep-Logan phantom*, which is a synthetic image widely used to simulate the absorption of radiation in important regions of the brain, including small tumours.